

# **Modelling of the Liquid Slag Behaviour in the Continuous Casting Mould**

Ph.D.  
**Zacharias Kountouriotis**

School of Computing and Mathematical Sciences  
the University of Greenwich  
London, England.

A thesis submitted in partial fulfilment of the requirements of the University of Greenwich  
for the degree of Doctor of Philosophy

April 2011

# Declaration

“I certify that this work has not been accepted in substance for any degree, and is not concurrently being submitted for any degree other than that of Doctor of Philosophy (Ph.D.) being studied at the University of Greenwich. I also declare that this work is the result of my own investigations except where otherwise identified by references and that I have not plagiarised another’s work”.

-----  
Zacharias Kountouriotis

-----  
Professor Koulis Pericleous

-----  
Dr. Mayur Patel

-----  
Dr. Georgi Djambazov

## **Abstract**

This work presents a fluid dynamics model of a continuous caster mould region, including the transient behaviour of the steel/slag interface. The research was carried out in collaboration with ArcelorMittal Research (AMR), based in Maizières-les-Metz in France. The industrial objective of the thesis was to understand the factors affecting the transient behaviour of the liquid slag layer covering the steel and its interaction with the Submerged Entry Nozzle (SEN) jet supplying the steel from the tundish to the Continuous Casting (CC) mould. The study includes the very complex phenomenon of argon bubble transport which also affects the behaviour of the slag layer and SEN jet. The model developed in this study is based on the finite volume method with the liquid regions (steel, slag) solved in an Eulerian scheme on a fixed unstructured mesh. The interface behaviour is modelled using a number of VOF type schemes, including the time-efficient Counter Diffusion Method (*CDM*). A coupled Lagrangian particle tracking scheme is used to represent the presence of argon bubbles and their influence on the flowfield (mainly due to buoyancy) in conjunction with the fluctuating surface dynamics. The bulk of the research concerns comparisons against flowfield and interface data obtained from an experimental water/oil study of the process. However, the model is extended to include predictions of heat transfer and phase change in the steel and flux powder regions in an industrial CC unit and validation against available data. The three-phase model is developed making use of the unstructured mesh multi-physics finite volume code PHYSICA [1].

As stated, the main goal of this particular work has to do with the study of the dynamic behaviour of the steel/slag interface, including the effects of casting speed and injected gas. Because of the great difficulty in physical experiments with a real caster, the research is supported with water model experiments and mathematical simulation. Comparisons of observed interface profiles, measured and predicted mean and fluctuating velocities, gave an insight to the degree of coupling between interface behaviour and the fluid dynamics within the mould region. In particular, a spectral analysis of the dominant fluctuation frequencies in the water/oil experiment suggests a strong link between the upper and lower recirculation loops generated by the SEN jet as it splits after contact with the narrow face for the mould. The presence of gas bubbles alters the spectral picture, since the buoyancy induced in the

flow affects the behaviour of the jet, leading to the one/two loop behaviour known from experiments. Good qualitative and quantitative agreement was achieved between the numerical results and water-model experimental data. The main observations drawn from the water model simulation and experiment are as follows:

- An increase in casting speed, which is equivalent to an increase in SEN velocity leads to an increase in the amplitude of interfacial fluctuations.
- At the highest SEN velocities, the oil layer is pushed away from the narrow ends of the mould, exposing the water surface to air.
- When there is no oil on top of the water surface, the surface remains for all practical purpose flat.
- Air entering through the SEN influences the flowfield in the mould and also disturbs the oil/water interface when it passes through it.
- The ratio of water to air flow rate seems to be the most important parameter, with high air/water flow ratios leading to a change in flowfield at the top of the mould as the gas buoyancy lifts the SEN jet towards the surface.

To achieve a good correlation between the experiments and the simulations a number of factors in the numerics were found to be important. These are:

- The quality of the mesh used, especially in the complex transition from the SEN geometry – essentially a cylinder with two outlets set at a specific angle of  $20^\circ$  to the vertical, to the thin rectangular geometry of the mould which is designed to cast flat products.
- The turbulence model, which was initially found to suppress interface oscillations whenever an oil layer was introduced. Various approaches were followed to overcome this problem, (a)removing the turbulence model from the oil layer, (b) using a low frequency filter to remove resolved turbulence kinetic energy from the k- $\epsilon$  model, (c)opting for the high order SMART numerical scheme in preference to the default Hybrid.

- The interface tracking algorithm used as a default in the code PHYSICA is essentially a VOF technique with options for a Van-Leer (TVD) scheme [2] or alternative the popular Donor Acceptor scheme [3,4], both options work well but they are explicit and therefore extremely expensive computationally. Due to the size of the mesh and the CFL limit for stability, timesteps as small as  $10^{-3}$ s become necessary, meaning a 600s simulation could take up to 8 weeks! To overcome this, the implicit CDM scheme [5] was used, which allows the interface to spread by diffusion but then pushed back against the gradient to re-sharpen at the end of each timestep. With this scheme, timesteps up to 2 orders of magnitude larger become possible, the limit then governed by the frequency range to be resolved.

A non-standard approach to the Lagrangian particle tracking scheme was adopted in the simulation with the following characteristics:

- The amount of gas entering was divided into packets of equal bubble diameter and then each packet was further divided into individual tracks. The transport of 1000 and more particles tracks was used to ensure a realistic dispersion.
- Tracks were updated at regular time intervals (but not necessarily at each Eulerian timestep) and then followed until they exited the calculation domain.
- The residence time of particles in each cell provided information for the gas content of the cell and therefore its density. With this approach, the Navier-Stokes equations then solve for mixture (gas and liquid) and lighter cells are influenced by buoyancy.
- The bubble tracks are affected by the mean velocity of the surrounding fluid and also by a stochastic component derived from the turbulence model. However, there is no direct feedback to fluid turbulence from the bubbles.

To extend simulations to a real caster, heat transfer and phase change were introduced in the model, in addition to the property changes (water to steel, oil to slag, air to argon). Of importance here was the development of a solidified skin of steel on the water-cooled mould walls and also the melting of flux powder into a liquid layer on the top surface. This last component of the research was introduced to enable comparisons against plant data obtained by AMR. Of particular interest in this study was the transition from a double to a single roll

recirculation in the top section of the mould, as a function of the relative quality of argon entering the SEN. The model was able to reproduce this behaviour for the cases studied.

Although much has been done in developing this model of the continuous casting process it is evident that much more research is needed, especially in the case of a real caster. For example, the thermophysical property variations in the slag due to temperature, composition and mass transfer were ignored. A very simple approach was used for the phase change in steel and flux powder, although since the PHYSICA framework is modular, more sophisticated alternatives can be easily introduced. The boundary conditions for heat transfer remain uncertain and the values used in this study were obtained from the industrial partner from earlier experiments.

In spite the aforementioned limitations, the model is very useful, especially in understanding the dynamic interactions between the SEN jets, and the slag/steel interface and in this respect in advance of other models used by industry.

## **Acknowledgements**

This thesis would not have been accomplished without the funding provided by ArcelorMittal and the University of Greenwich, and the guidance plus invaluable assistance of several people.

Firstly, I would like to thank the University of Greenwich for giving me the opportunity to undertake my PhD studies and moreover, for the financial support provided by the collaboration between ArcelorMittal Research (AMR) and the University. Special thanks are due to Drs Jean-François Domgin and Pascal Gardin from AMR, for providing me with empirical data and boundary conditions. Moreover, I am grateful to AMR for the opportunity they gave me to assist in obtaining new experimental measurements performed using Laser Doppler Anemometry (LDA) and to get an overall experience of continuous casting through brainstorming and presentations with researchers in AMR.

I would like to express my appreciation to my supervisors Professor Pericleous, Dr Djambazov and Dr Patel. Particular thanks to Professor Pericleous for the important scientific guidance, the overall knowledge he provided to me and finally, the confidence which he showed in me during this period. I am also grateful to Dr Georgi Djambazov for his assistance in resolving several problems occurring during the thesis and additionally, for providing a FORTRAN code for averaging the signal and Mb3 mesh. Furthermore, I would like to thank Dr Patel for his support and invaluable help whenever I needed it. I am also thankful to Dr Nick Croft, from the University of Swansea, for the PHYSICA user routine implementing solid velocity in solidified regions of the casting and for the Gambit to Physica conversion mesh filter. I would also like to express my appreciation to my colleague Bruno Lebon for his help and the important information which he gave to me in the beginning of my studies. My special appreciation goes to Dr Nikolaos Christakis from University of Crete, who shared my concerns and provided me with valuable advice from the beginning of my PhD studies.

Finally, I would like to thank my family for their support and encouragement through my many years of education. Last but not least, I would like to thank my fiancée Makrina for her patience and comprehension throughout my studies.

## Contents

<b>Declaration.....</b>	<b>i</b>
<b>Abstract.....</b>	<b>ii</b>
<b>Acknowledgements.....</b>	<b>vi</b>
<b>Contents .....</b>	<b>viii</b>
<b>List of Tables .....</b>	<b>xii</b>
<b>List of Figures.....</b>	<b>xiii</b>
<b>Nomenclature .....</b>	<b>xviii</b>
<b>List of Abbreviation .....</b>	<b>xx</b>
<b>Chapter I.....</b>	<b>1</b>
<b>1 Introduction.....</b>	<b>1</b>
1.1 Objectives and study framework .....	2
1.2 The process of continuous casting of steel .....	4
1.3 Thesis overview .....	7
<b>Chapter II .....</b>	<b>10</b>
<b>2 Literature Review .....</b>	<b>10</b>
2.1 Fluid flow of liquid steel including turbulence model. ....	11
2.1.1 Metal flow pattern in the mould and the SEN .....	11
2.1.2 Turbulence model .....	13
2.2 Predictions of heat transfer, solidification and chemical reaction.....	16
2.3 Bubble particles and droplets behaviour .....	19
2.4 Mathematical modelling and water model configuration.....	22
2.5 Predictions of mould oscillation and applied magnetic field .....	24
<b>Chapter III.....</b>	<b>27</b>

<b>3 Modelling Approach .....</b>	<b>27</b>
3.1 General framework .....	27
3.2 Steady-state model .....	28
3.2.1 Fluid flow .....	29
3.2.2 Heat transfer and solidification.....	29
3.2.3 Turbulence model .....	30
3.3 Transient model .....	32
3.3.1 Free surface tracking .....	32
3.3.2 Particle tracking .....	35
3.4 Water model details .....	39
<b>Chapter IV .....</b>	<b>43</b>
<b>4 Description of Numerical Simulations .....</b>	<b>43</b>
4.1 Steady state .....	43
4.1.1 Mesh and boundary conditions.....	43
4.1.2 Fluid flow .....	45
4.1.3 Heat transfer and solidification.....	46
4.2 Transient simulations .....	48
4.2.1 Mesh and boundary conditions.....	48
4.2.2 Turbulence model modification.....	51
4.2.2.1 First order Hybrid scheme .....	56
4.2.2.2 Second order SMART scheme .....	58
4.2.3 Free Surface simulation .....	59
4.2.4 Particle tracking simulation .....	60
4.3 Industrial configuration.....	63
4.3.1 Mesh and boundary conditions.....	63

<b>Chapter V.....</b>	<b>67</b>
<b>5 Data Analysis and Validation using the Water Model Configuration.....</b>	<b>67</b>
5.1 Qualitative results .....	68
5.1.1 Oil behaviour .....	69
5.1.2 Gas behaviour .....	71
5.2 Quantitative results .....	74
5.2.1 Spectrum analysis .....	75
5.2.2 Comparing numerical results against LDA experiments.....	78
5.2.3 Influence of water flow rate.....	80
5.2.4 Influence of oil (Free surface) .....	82
5.2.5 Influence of gas .....	84
5.2.6 Flow oscillation prediction .....	88
5.2.6.1 Influence of water flow rate in the meniscus stability.....	90
5.2.6.2 Influence of oil and gas on the meniscus velocity.....	92
<b>Chapter VI .....</b>	<b>94</b>
<b>6 Validation against Industrial Configuration.....</b>	<b>94</b>
6.1 Assumptions and solution methodology.....	96
6.2 Metal flow in the mould and the effect of argon gas.....	97
6.3 Influence of argon and immersion depth in the of shell thickness .....	102
6.3.1 Validation of shell thickness.....	105
<b>Chapter VII.....</b>	<b>106</b>
<b>7 Conclusions and Further Work.....</b>	<b>106</b>
7.1 Conclusions.....	106
7.2 Further work.....	110
<b>REFERENCES.....</b>	<b>112</b>

**Appendices ..... 125**

Appendix A. INFORM file for water model configuration ..... 125

Appendix B. INFORM file for industrial model configuration ..... 130

Appendix C. PHYSICA User routine..... 136

    C. 1. Moving Solid .....136

    C. 2. Heat Flux in the Mould .....137

Appendix D CD containing Thesis .pdf file and CC animations ..... 138

## **List of Tables**

Table 3.1: Water model parameters according to Froude similarity where $K$ is the scale factor equal to 100/220 for the CC mould water model.....	40
Table 4.1: Water model geometry and and dimensions.....	44
Table 4.2: Physica properties for the case with water and 2cm Oil.....	51
Table 4.3: Industrial model configuration geometry and dimensions .....	64
Table 5.1: Experimental and numerical cases studied. ....	67
Table 6.1: Properties and casting conditions reported in two cases studied.....	95

## **List of Figures**

Figure 1.1: Slab casting phenomena (courtesy B.G. Thomas, Univ. Illinois) .....	1
Figure 1.2: A schematic process of the continuous casting of steel (Courtesy B. G. Thomas [14]).....	5
Figure 1.3: Complex phenomena in the Continuous Casting of Steel (provided by AMR).....	6
Figure 2.1: The velocity field in the plane of SEN port: a) $V_c=0.8\text{m/min}$ , b) $V_c=1.2\text{m/min}$ c) $V_c=1.8\text{m/min}$ [45] .....	13
Figure 2.2: Effect of $k-\epsilon$ inlet values on calculated velocities in the water model [53, 54] ....	14
Figure 2.3: Time averaged velocity field in the middle plane [46]. .....	16
Figure 2.4: Temperature field in the middle plane [52].....	17
Figure 2.5: Thermal boundary condition of flux layer [66].....	18
Figure 2.6: Inclusions outlining the former surface of bubbles [42]. .....	22
Figure 2.7: Schematic formation of curved hook and meniscus solidification. (Courtesy B. G. Thomas [94]).....	25
Figure 3.1: Video stills of the water-model experiment performed by AMR (2009) with and without gas .....	40
Figure 3.2: LDA technique (Official website from Data dynamic).....	41
Figure 3.3: Experimental measurement arrangement .....	42
Figure 4.1: Hexahedral mesh created by HARPOON. ....	44
Figure 4.2: Streamlines starting from inside nozzle show the two characteristic recirculation zones. ....	46
Figure 4.3: Mean temperature field in the x-z plane in the centre of the mould .....	47
Figure 4.4: Left port and right port are shown to be not symmetrical across the middle plane .....	49
Figure 4.5: Corrected mesh with non-orthogonality contour.....	50
Figure 4.6: Velocity magnitude contours and velocity vectors (a) with filter (left) and (b) without filter (right). ....	52

Figure 4.7: Monitor distribution of horizontal velocity at Points 1,4 and 5 (simulation with inlet velocity 1.018m/s). The oscillations persist at relatively constant amplitude throughout the simulation when the filter is used. ....53

Figure 4.8: Comparing mean values and Standard Deviation of horizontal velocity for the seven measurements points between various k-ε filter lengths using original flawed mesh...53

Figure 4.9: Comparing mean values and Standard Deviation between the case with k-ε filter and without.....54

Figure 4.10: Comparing mean values obtained with the original mesh and the improved mesh using the Hybrid scheme without a k-ε filter.....55

Figure 4.11: Control Volume.....56

Figure 4.12: Free surface with CDM (left) and Donor Acceptor (right) using 0.01s time-step .....59

Figure 4.13: Oil/water inter-surface and contour of the surface tracking variable  $\phi$  ‘fs-phi’ at the symmetry place, y=0 showing velocity vectors using the SMART scheme..... 60

Figure 4.14: Flow pattern in the middle plane of the mould with the interface fs-phi iso-surface, iso-surface of gas volume fraction and typical particle tracks. Large bubble tracks are in black and small bubbles are in blue colour..... 62

Figure 4.15: Influence of gas in the flow pattern in the case with inlet velocity 1.018m/s and a 2cm Oil layer..... 63

Figure 4.16: Two different meshes used for the investigation of the influence of gas (Left) and finer enough mesh to capture the phase transformation of the slag layer (Right). ..... 65

Figure 4.17: Dimensions and boundary conditions plus nozzle design..... 66

Figure 5.1: Comparison of turbulent viscosity between Hybrid (turbulence model is eliminated in the oil layer) and SMART schemes, shown together with velocity vectors and the iso-surface of the interface. .... 69

Figure 5.2: Monitor point history comparison between the SMART scheme, Hybrid scheme (turbulence model eliminated in oil layer) and experimental point 4..... 69

Figure 5.3: Qualitative comparison between experimental and numerical results with a 2cm oil layer and inlet velocity of 1.018m/s. .... 70

Figure 5.4: Qualitative comparisons between experimental and numerical results without oil and an inlet velocity of 1.018m/s..... 70

Figure 5.5: Free surface profile for different water flow rate in experiments. a) 0.5m/s b) 0.8m/s c) 1.018m/s. The interface has been highlighted in the pictures for ease of identification. .... 71

Figure 5.6: Free surface profile for different water flow rate in CFD simulations with velocity vectors shown in the middle plane. a) 0.5m/s b) 0.8m/s c) 1.018m/s..... 71

Figure 5.7: Influence of gas flow rate in the LDA experiment: (a) No gas, (b) 2NI/min - Inlet velocity 1.018m/s..... 72

Figure 5.8: Influence of gas flow rate - 2NI/min - 2cm Oil - Inlet velocity 1.018m/s..... 73

Figure 5.9: Particles tracks of six different diameter sizes ..... 74

Figure 5.10: Experimental measurements arrangement for LDA and computation results. ... 74

Figure 5.11: Raw signal of LDA for point 4- 2cm oil no gas and inlet velocity set at 1.018m/s..... 76

Figure 5.12: Comparisons of filtered signal and spectrum between LDA (red) and CFD (blue). The spectrum is for point4 for case 2B of table 5.1 and inlet velocity set at 0.8m/s. .. 77

Figure 5.13: Comparisons of Mean values and Standard Deviations between LDA and CFD for the case with inlet velocity of 0.5m/s with 2cm Oil and without gas. .... 78

Figure 5.14: Comparisons of Mean values and Standard Deviations between LDA and CFD for the case with inlet velocity of 0.8m/s with 2cm oil and without gas. .... 79

Figure 5.15: Comparisons of Mean values and Standard Deviations between LDA and CFD for the case with inlet velocity of 0.8m/s with 2cm air and without gas. .... 79

Figure 5.16: Comparison of horizontal velocity distribution between LDA and CFD at point 6..... 80

Figure 5.17: Influence of water flow rate in mean value of horizontal velocity in case with 2cm Oil without gas using LDA and CFD results. .... 81

Figure 5.18: Influence of water flow rate in mean value of horizontal velocity in case with 2cm air without gas using LDA and CFD results. .... 81

Figure 5.19: Influence of water flow rate in standard deviation of horizontal velocity in case with 2cm air without gas using LDA and CFD results. .... 82

Figure 5.20: Influence of oil layer on the horizontal velocity at the meniscus - Mean Values for point 1,4and 5 using LDA. .... 82

Figure 5.21: Influence of oil layer on the horizontal velocity fluctuation at the meniscus- Standard Deviation for point 1, 4 and 5 using LDA. .... 83

Figure 5.22: Influence of oil layer on the horizontal velocity at the meniscus - Mean Values for point 1,4and 5 using CFD. ....83

Figure 5.23: Influence of oil layer on the horizontal velocity fluctuation at the meniscus- Standard Deviation for point 1, 4 and 5 using CFD. ....84

Figure 5.24: Influence of gas injection on the horizontal velocity (mean value) and fluctuation (standard deviation) at the meniscus using LDA. Comparison between case 2A (0.5m/s 2cm Oil No Gas) and 2C (0.5m/s 2cm Oil Gas 2L/min) .....85

Figure 5.25: Influence of gas injection on the horizontal velocity (mean value) and fluctuation (standard deviation) at the meniscus using LDA. Comparison between case 2A (0.8m/s 2cm Oil No Gas) and 2C (0.8m/s 2cm Oil Gas 2L/min) .....85

Figure 5.26: Influence of gas injection on the horizontal velocity (mean value) and fluctuation (standard deviation) at the meniscus using LDA. Comparison between case 3A (1.018m/s 2cm Oil No Gas) and 3C (1.018m/s 2cm Oil Gas 2L/min). .....85

Figure 5.27: Influence of gas injection on the horizontal velocity (mean value) and fluctuation (standard deviation) at the meniscus using CFD. Comparison between case 3A (0.8m/s 2cm Oil No Gas) and 3C (0.8m/s 2cm Oil Gas 2L/min). .....86

Figure 5.28: Influence of gas injection on the horizontal velocity (mean value) and fluctuation (standard deviation) at the meniscus using CFD. Comparison between case 3A (1.018m/s 2cm Oil No Gas) and 3C (1.018m/s 2cm Oil Gas 2L/min). .....87

Figure 5.29: Bubbles diameter distribution provided by ARM for water model configuration .....87

Figure 5.30: Experimental and numerical spectra for horizontal velocity components – 0.5m/s 2cm Oil no gas Point 5.....88

Figure 5.31: Experimental and numerical spectra for horizontal velocity components – 0.8m/s No Oil no gas Point 5.....89

Figure 5.32: Experimental and numerical spectra for horizontal velocity components – 1.018m/s no Oil no gas, Point 5 and Point 2.....89

Figure 5.33: Four typical computed particle trajectories. ....90

Figure 5.34: Influence of water flow rate, Spectrum Analyses comparisons with LDA data .91

Figure 5.35: Influence of water flow rate, Spectrum Analyses-CFD results using SMART scheme.....92

Figure 5.36: Influence of Oil and gas for point 4 –  $V_{in}=0.8m/s$ . The left column shows the filtered LDA signal and the right column the spectrum. The three rows correspond to: no oil layer, oil layer, oil+gas. ....92

Figure 5.37: Influence of Oil for point 4 – CFD-Inlet Velocity 0.8m/s.....93

Figure 6.1: Interpolated velocity at the meniscus considering all immersion depths from industrial measurements.....98

Figure 6.2: Flux surface with velocity vectors in the middle plane and contours of argon concentration, calculated and iso-surface of liquid fraction equal to 0.5. a) 0.8m/min, b) 1.6m/min. ....99

Figure 6.3: Flux surface with velocity streamlines from inside the nozzle in the middle plane, temperature distribution and argon concentrations contours. a) 0.8m/min, b) 1.6m/min..... 100

Figure 6.4: Comparison between Industrial velocity vectors (according to the slope of the solidified steel nails) and simulation vectors in the meniscus.0.8m/min - Immersion Depth 160mm. Single roll is predicted. .... 101

Figure 6.5: Comparison between Industrial velocity vectors (according to the slope of the solidified steel nails) and simulation vectors in the meniscus.1.6m/min – Immersion Depth 160mm. Double roll is predicted. .... 101

Figure 6.6: Comparison of the average horizontal velocity of plant measurement against numerical monitor history- Left: Vc 0.8m/min , Right: Vc 1.6m/min. .... 102

Figure 6.7: Temperature distribution with shell profile at the impingement point and the mould exit. .... 103

Figure 6.8: Temperature distribution with shell profile at the impingement point and the mould exit (Z=-0.83). Immersion depth set at 160mm with Vc=1.6m/min. .... 103

Figure 6.9: Influence of gas on the shell thickness at the mould exit (top), the flow pattern and in the temperature distribution within the mould. Left figures present the results without gas while the right figures are with argon gas. .... 104

Figure 6.10: Validation of shell thickness profile in the mould exit with previous work from Ramirez-Lopez et al [129] Meng et al [65], Thomas et al [130] and Bruno [89]. .... 105

## Nomenclature

$A$	area	$m^2$
$A_{inlet}$	SEN inlet area	$m^2$
$A_{outlet}$	mould outlet area	$m^2$
$C_{pl}$	specific heat of liquidus phase (steel, slag)	J/kg K
$C_{ps}$	specific heat of solidus phase (steel, slag)	J/kg K
$C_d$	drag coefficient	
$C1, C\mu, C2$	turbulent constants	
$dp$	Particle diameter	m
$ds$	Shell thickness	m
$D_{SEN}$	SEN diameter	m
$Fr$	Froude number	
$g$	gravity vector	$m/s^2$
$H$	enthalpy	kJ
$h$	heat transfer coefficient	$W/m^2K$
$h_{gap}$	heat transfer coefficient in the gap	$W/m^2K$
$K$	permeability coefficient	
$k$	turbulent kinetic energy	$m^2s^{-2}$
$k_s$	Steel conductivity	W/m K
$k_f$	Flux Conductivity	W/m K
$L$	Latent Heat of solidification	Kj/Kg
$Nu$	Nusselt number	
$m$	Mass	Kg
$\dot{m}$	mass flow rate	Kg/s
$\dot{m}_{air}$	Mass flow rate of air	Kg/s
$m_p$	particle mass	Kg
$Np$	Total number of particles	
$P$	pressure	Pa
$Pr$	Prandtl number	
$q$	Convection flux	$W/m^2$
$Q_{air}$	Air flow rate	NI/min
$Q_{argon}$	Argon flow rate	NI/min
$Q_w$	Water flow rate	$m^3/h$

$Re$	Reynolds number	
$T_{amb}$	ambient temperature	$^{\circ}\text{C}$
$T_{mould}$	mould temperature	$^{\circ}\text{C}$
$T_L$	liquidus temperature (steel, slag)	$^{\circ}\text{C}$
$T_S$	solidus temperature (steel, slag)	$^{\circ}\text{C}$
$T_{inlet}$	Inlet Temperature	$^{\circ}\text{C}$
$T$	Time	s
$u_p$	particle velocity	m/s
$u$	Instantaneous velocity vector	m/s
$\bar{u}$	average velocity vector	m/s
$u'$	velocity fluctuation vector	m/s
$V$	element volume	$\text{m}^3$
$V_p$	particle volume	$\text{m}^3$
$V_{inlet}$	Inlet Velocity	m/s
$V_c$	Casting Velocity	m/min
$We$	Weber number	
$\gamma$	surface tension	N/m
$\Delta t_e$	eddy lifetime	s
$\Delta t_r$	droplet passing time through an eddy	s
$\delta t$	Time-step	s
$\delta x$	internal length of a cell	m
$\varepsilon$	dissipation rate of turbulent kinetic energy	$\text{m}^2/\text{s}^3$
$\mu_t$	Turbulence dynamic viscosity	$\text{Kg}/\text{m s}$
$\mu_{lam}$	Laminar viscosity	$\text{Kg}/\text{m s}$
$\nu_{oil}$	oil kinematic viscosity	$\text{m}^2/\text{s}^{-1}$
$\nu_{water}$	water kinematic viscosity	$\text{m}^2/\text{s}^{-1}$
$\nu_{steel}$	steel kinematic viscosity	$\text{m}^2/\text{s}^{-1}$
$\nu_{flux}$	flux kinematic viscosity	$\text{m}^2/\text{s}^{-1}$
$\rho_{water}$	density of water	$\text{Kg}/\text{m}^{-3}$
$\rho_{oil}$	density of oil	$\text{Kg}/\text{m}^{-3}$
$\rho_{gas}$	density of gas	$\text{Kg}/\text{m}^{-3}$
$\rho_{flux}$	density of flux	$\text{Kg}/\text{m}^{-3}$
$\rho_{steel}$	density of steel	$\text{Kg}/\text{m}^{-3}$
$\sigma_t$	turbulent Prandtl number	
$\sigma_T$	standard deviation	

## List of Abbreviations

AMR	ArcelorMittal Research
CAD	Computer-Aided Design
CC	Continuous Casting
CDM	Counter Diffusion Method
CFD	Computational Fluid Dynamics
CFL	Courand Freidrick Levy
DNS	Direct Numerical Simulation
EMB	Electromagnetic Breakers
EMLS	Electromagnetic Level Stabilizer
EMS	Electromagnetic Stirrers
FFT	Fast Fourier Transfrom
FV	Finite Volume
LDA	Laser Doppler Anemometry
LES	Large Eddy Simulation
LFN	Liquid Fraction
NS	Navier Stokes
PIV	Particle Image Velocimetry
RANS	Reynolds Averaged Navier Stokes
SEN	Submerged Entry Nozzle
SGS	Sub-grid Scale
STL	StereoLithography
SVC	Sub-meniscus Velocity Control
TVD	Total Variation Diminishing
VOF	Volume of Fluid

# Chapter I

## 1 Introduction

The continuous casting method for plate steel production presents one of the most difficult problems to solve considering its complexity. It attracts a lot of people involved in industrial research and also numerical CFD practitioners in its development and optimisation. The main research effort has to do with the improvement of product quality and reduction of cost by understanding the complex phenomena occurring in the entire process of CC. There have been many studies since the 1950s [6, 7, 8] attempting to explain several phenomena presented in CC as illustrated in Figure 1.1. A comprehensive knowledge of the problem and software implementation in CFD provides significant time and cost savings in comparison to physical testing methods and measurements. Consequently, the increase in computer power has forced process engineers to model the continuous casting process; however, there are several issues that require additional research.

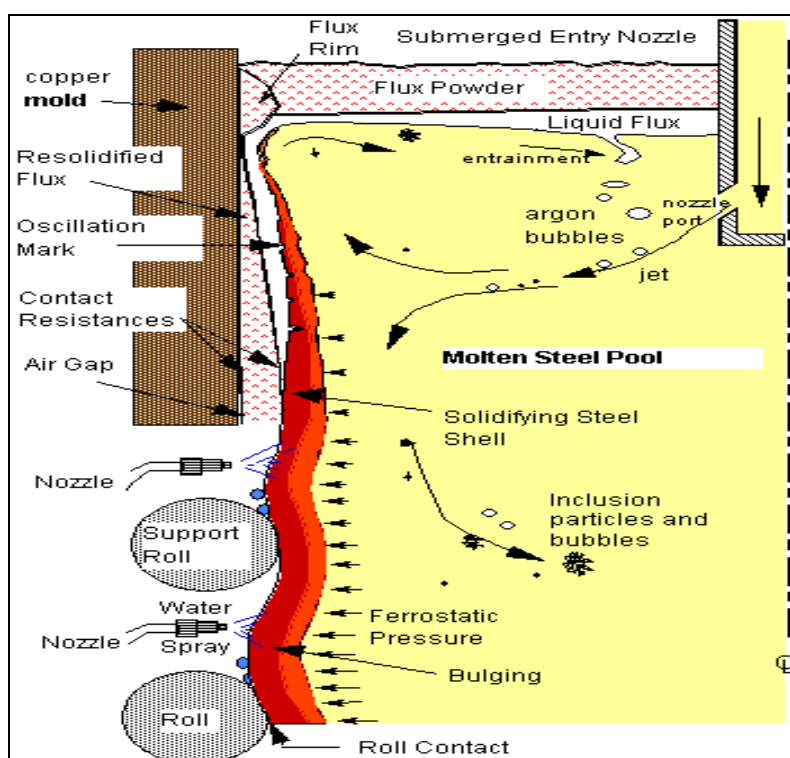


Figure 1.1: Slab casting phenomena (courtesy B.G. Thomas, Univ. Illinois)

Two main problems that may occur in CC concern (1) breakout due to insufficient lubrication at the steel-mould contact region, or insufficient heat transfer leading to a weak solidifying

skin and (2) carbon boil and oxygen reaction with carbon in the steel to form CO [9]. For these reasons, control of the temperature in the mould (and the ladle) and the addition of a slag layer at the top of the mould are important. The casting nozzles tend to get clogged considering the presence of inclusions and additions of aluminium and/ or silicon in the steel. To prevent this effect, argon gas is added to the SEN during CC which also affects the flow pattern in the nozzle and, as a result, in the mould. For these reasons, CC becomes a three-phase flow problem.

Keeping in mind the high cost and physical risk of actual casting measurements, mathematical modelling and water model experiments are extremely important tools in order to understand and improve the CC process. In this research a numerical model is developed to describe the turbulent flow pattern in the CC mould region, starting with detailed validation against water model experiments. In these experiments water represents molten steel, a top layer of silicon oil the slag, and air the argon gas. Emphasis is given to understanding the dynamic behaviour of the water/oil interface as a function of SEN jet velocity, recognizing interfacial turbulence as a source of inclusions. The air bubbles, modelled using a particle tracking technique, influence the flowfield in the mould and alter the interface behavior. Since the model has to also represent a real industrial process, heat transfer and phase change in the steel and flux regions are also included and the model predictions are compared to available industrial process data.

## ***1.1 Objectives and study framework***

The industrial objective of this thesis is to improve the quality of the steel plate, through a deeper understanding of fundamental phenomena relevant to the process of continuous casting of steel. For this purpose, a comprehensive 3D, validated, transient model of the CC process mould region is to be developed (that is excluding regions far downstream of the mould). The model will be based on the Finite Volume CFD framework, as provided by the Greenwich code PHYSICA. In the simulations, special emphasis is to be given to the slag/steel interface modelling and its unsteady behaviour. Consequently, a key objective is that of the comparison between experimental water model configuration data (provided by AMR) and the mathematical model used. In reality, this problem is a three-phase one, since gas is usually injected together with the molten steel into the caster. To address this

phenomenon, a Lagrangian tracking algorithm is used to track air bubbles (instead of argon) flow, through the SEN and which are seen in the experiments to disturb the water/oil interface.

Several new objectives appeared during model development and validation: Free surface tracking was initially investigated using the Donor-Acceptor method, one of the Volume of Fluid [3, 4] methods available inside PHYSICA and then using improved tracking fully implicit method (Counter Diffusion Method-CDM) [5]. This new method speeds up the computation as bigger time-steps can be used, without violating the stability limits imposed on explicit methods by the Courant-Freidrick-Levy (CFL) criterion. In addition, the study aims to increase the understanding of the interaction of the slag/steel (oil/water) interface with the SEN jet and the influence of the buoyancy forces of gas. Consequently, the slag (oil) surface was coupled with a computationally efficient Lagrangian tracking scheme, hence to the development of a three-species transient model. Good qualitative and quantitative comparisons were achieved using the CDM method either with gas or without.

A  $k$ - $\varepsilon$  turbulence model suitable for transient simulation was implemented during the operation of numerical simulation avoiding the LES model due to high computational cost. Previous results [5] indicated that the use of the standard  $k$ - $\varepsilon$  model in transient RANS computations leads to the rapid suppression of the oil/water interface oscillation. To overcome this problem, a ‘filter’ [10] in the Kolmogorov-Prandtl equation was introduced, reducing the computed effective viscosity by removing the resolved low frequency content of the turbulent kinetic energy  $k$ . A better amplitude of surface oscillation and qualitative results that are more in accordance with experimental data were obtained with this method but the mean value of the velocity was adversely affected. Since the filter has an adjustable length scale parameter related to the SEN jet diameter, a more systematic study of this parameter is needed in the future. Since numerical diffusion can also be a problem in FV discretization, in parallel to turbulence model improvements, the application of a second order accurate scheme in PHYSICA was examined. The quadratic upwind bound scheme SMART [11] was found to give the best qualitative (visualization, observation) and quantitative (mean values, standard deviation, spectrum analyses) results. A detailed description of the numerical difficulties encountered and methods used to overcome them is presented in Chapter 4.

Validation of numerical results against LDA measurements is critically important to establish confidence for future plant trial simulations. Detailed investigation of numerical and LDA measurements helps to explain several observed phenomena and raises awareness of the effects of the different process parameters. The findings of this work include fundamental understanding of the dynamic behaviour of oil/water interface and main characteristics of metal flow. In addition, the model successfully predicts the modifications of flow and notably disturbed interface due to buoyancy forces of the air injection.

The second stage of this thesis comprises the modeling of an industrial caster operated by ArcelorMittal. For this purpose the model usability was expanded with the implementation of heat transfer and solidification. The objective here was the study of the influence of casting velocity and argon gas flow rate on steel/slag interface behaviour, general flowfield pattern, prediction of the liquid slag layer thickness and extend of strand formation within the mould region. Validation is against available plant data, obtained in the mould region by AMR.

## ***1.2 The process of continuous casting of steel***

With reference to Figure 1.2, the hot steel in liquid form enters from the ladle via a pipe to the tundish container where most of the impurities are removed. Steel then flows from the tundish into the mould through the SEN. The SEN jets induce upper and lower recirculation loops in the mould as arise in Figure 1.3. Control of these loops is very important in the process as they are strictly related to the wave formation of the steel/slag interface, the distribution of the heat and the stability of the steel meniscus behaviour, where is the curved in the upper surface of steel produced due to its contact with the slag layer. The water-cooled mould causes a thin shell, or strand, to solidify and oscillates vertically so that the solidified shell separates from the mould. At first only a very thin shell appears and as time passes this shell grows so that it becomes thick enough to support the weight of the liquid steel [12].

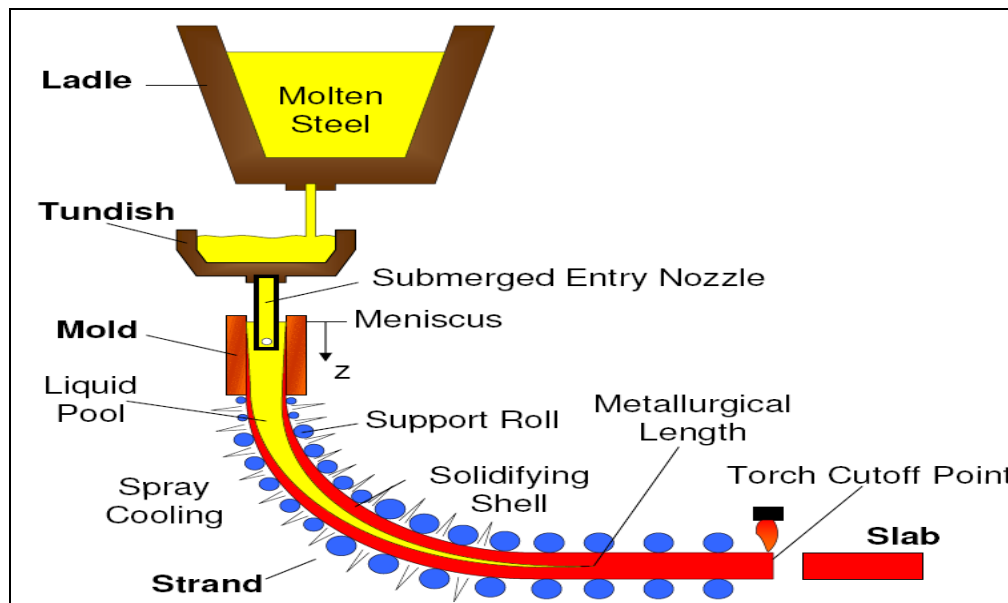


Figure 1.2: A schematic process of the continuous casting of steel (Courtesy B. G. Thomas [14])

A layer of liquid/slag powder is added to the top of the metal to prevent sticking and to trap any inclusion particles. The behaviour of this slag layer is very important for a number of reasons, since it prevents the meniscus from oxidation, provides the optimum level of horizontal heat transfer, allows absorption of inclusions from the steel and prevents the steel surface from freezing [13]. Furthermore, gas bubbles are injected into the nozzle to limit the nozzle clogging and to remove inclusion by floatation, producing cleaner steel. A few small bubbles tend to follow the steel flow. The bigger bubbles circulate in the upper zone where they generally escape through the slag layer, although occasionally they may be entrapped in the solidifying shell, leading to serious surface defects, such as surface cracks and inclusions.

The strand, the solidified thin shell steel next to the mould wall, exits the base of the mould into a water spray region, whilst molten metal still appears within the walls of the strand. The strand is immediately supported by closely spaced water-cooled rollers against the ferrostatic pressure of the still-solidifying liquid within the strand. To increase the rate of solidification, the strand is also sprayed with large amounts of water, as it passes through the spray-chamber. When the completely solidified casting has attained the desired length, it is cut off with a cutter.

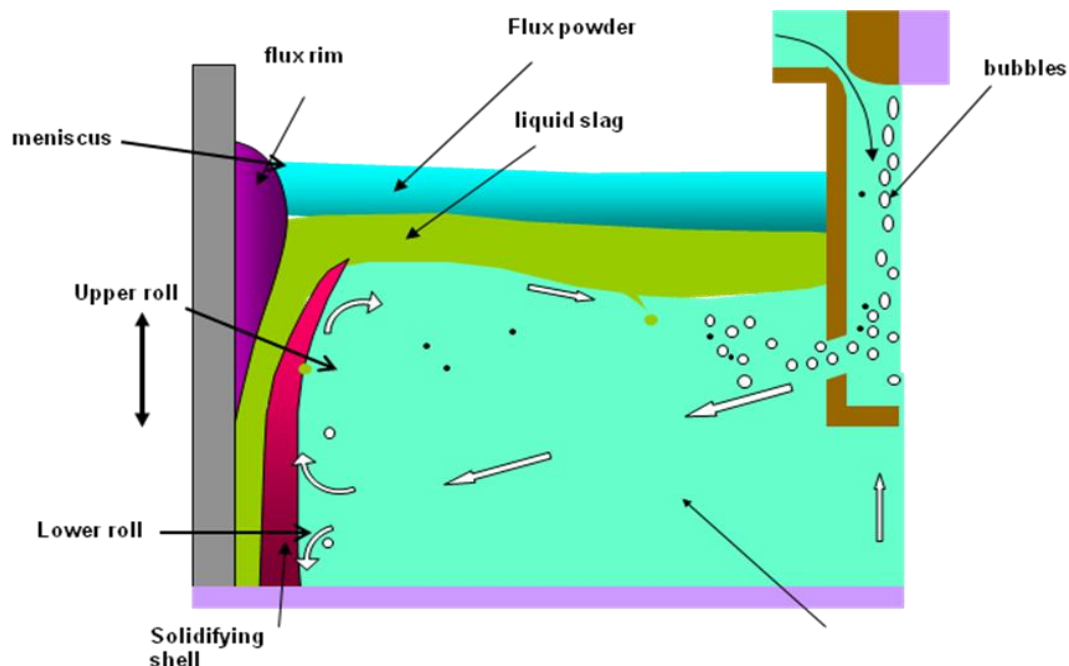


Figure 1.3: Complex phenomena in the Continuous Casting of Steel (provided by AMR).

This work concerns the development of a time-accurate model within the PHYSICA code framework used to understand the main parameters affecting the steel flow instability, including the effects of casting speed, the interaction of the dynamic slag layer with the SEN jet and the influence of the buoyancy forces of gas. The Eulerian representation of the flowfield in the mould region is accompanied by a realistic representation of gas bubble using a Lagrangian tracking scheme. The emphasis will be on the factors affecting the flow and the transient meniscus stability, including the effects of casting speed, the injected gas and the presence of the liquid slag (oil). Because of the great difficulty, in performing real caster experiments, the numerical model is supported with water model measurements performed by AMR. Observation of water experiments illustrate an almost flat air/water interface (without oil) for all the casting speed used (0.5m/s, 0.8m/s, 1.018m/s). On the other hand, a 2 cm oil layer, representing slag, leads to a wavy oil/water interface that becomes very disturbed at higher velocities. The finite-volume model successfully predicts the modification of the steel flow and the notably disturbed interface due to buoyancy forces of the air injection. In addition, the three-phase model proves the influence of gas in the SEN jet creating an upward flow near the nozzle and bulging oil surface, where the gas exits.

Simulations of various SEN casting velocities and gas flow rate accord very well with experiment leading to important suggestions which are applicable to the industrial casting.

Numerically, the presence of oil and the injection of air gas affect the horizontal velocity distribution at the meniscus, aiding the flow instability. Furthermore, a spectrum analysis of the collected horizontal velocity data and its distribution provides plausible explanations of the oscillation mechanism apparent during the continuous casting process. The observed frequencies characterize the periodic evolution of the horizontal velocity at the meniscus, which seem to be directly related to the oscillating movement of the SEN jet, the size of its roll and the SEN casting velocity. Considering the magnitude of the spectrum signal, the results validate the influence of oil and gas on the flow instability observed in qualitative comparisons of experimental video and numerical visualization.

In spite the considerable process of the analysis of experimental and calculation data, there is no clear link between the established frequencies of SEN jet, upper loop and the surface oscillations. Such a study provides a better knowledge in the unsteady behaviour of the steel flow which is the main parameter of the defects, such us the entrapment of inclusion. However, for the first time, the calculation validates the flow oscillation prediction of experimental results providing a new insight in the hydrodynamic parameters which affects the transient behaviour of steel flow in CC process.

### ***1.3 Thesis overview***

The research presented in this Thesis forms part of a research contract between Arcelor Mittal Research (AMR) and the University of Greenwich. The thesis consists of seven chapters and describes the mathematical basis and development of an efficient three-phase model of the CC process. Results are presented first for the experimental water model and then for an industrial configuration. In both simulations emphasis is placed on model validation. Initially, the thesis presents an introduction to the industrial objectives that govern the project framework as described at Section 1.1. Then, an overall description of various phenomena occurring in the CC process is given. Chapter 2 is a review of recent published works on the subject, which includes a general description of previous computational models and experiments that contributed to improved understanding of the continuous casting process. The chapter also includes a discussion of turbulence models used in steel flow simulations, heat transfer and solidification approaches, mathematical models of bubble behaviour and

their influence on fluid flow in the SEN and the mould, and finally previous water model configuration studies.

Chapter 3 describes the mathematical basis of the models developed starting with a steady-state simulation employed at the beginning of this research. This preliminary model was used in order to examine the basic fluid flow pattern and heat transfer effects, including an evaluation of the turbulence model used. Then a description of a transient calculation follows for three-phase turbulent fluid flow, including the free-surface treatment and the particle tracking approach. In addition, there is a description of the LDA measurements, performed in the AMR laboratories in Metz during the first year of my studies.

Chapter 4 contains a detailed presentation of two different meshes used and the results obtained for the water model experimental configuration. The chapter begins with an analysis of steady state and heat transfer plus solidification simulations using a mesh produced by the HARPOON [15] mesh generator. Afterwards, the results obtained using an alternative Gambit [16] mesh are shown. Several studies are described, with emphasis on free surface (or interface) behaviour. Moreover, introduction and testing of the turbulence dispersion effects on air bubbles (tracked using a Lagrangian numerical scheme) are illustrated.

Validation and analysis of the time-dependent water model results (for mean value, standard deviation and spectral characteristics) against existing Laser Doppler measurements are described in Chapter 5. The results highlight deficiencies of the numerical scheme used in the simulation and for this reason the chapter contains a description of the first order Hybrid scheme and second order SMART numerical scheme used, difficulties encountered, comparisons against experiment and other findings. The qualitative evaluation of the results against water model video visualizations clarify the observed main flow pattern, consisting of two recirculation zones and record using comparative images (and animation included in the Thesis CD) the oil/slag layer behavior both with gas and without.

Quantitative comparison of mean velocity and standard deviation is provided at seven measurement positions and the nature of observed wave action is explained with reference to derived frequency spectral patterns. For the first time frequencies are linked to the turnover

time of the two recirculation loops, which appear in the CC mould, for various SEN casting velocities and gas flow rates.

Chapter 6 is the study of a real industrial continuous caster in which an important change in the velocity profile takes place. Plant measurements predict a ‘single roll’ instead of the usual ‘double roll’ as the gas flow rate increases and casting velocity decreases. Additionally, the final case provides an opportunity to test the model with steel/slag properties and with the addition of heat transfer and solidification.

The final chapter in the Thesis is a summary of conclusions derived from the study and a brief description of proposed further research leading to improvements in the related phenomena presented and additions to the model necessary for industrial use.

## *Chapter II*

### **2 Literature Review**

The importance of continuous casting for world steel production and the economy justifies the intensive research activity in this topic, with the use of both mathematical models [17, 18, 19] and/or physical experiments [20, 21, 22]. The latter are key tools in the optimization of the process for product quality and increase in production speed. Great efforts have been expended in understanding the continuous casting process from the point of view of the physics involved, ranging from turbulent flow behaviour, to heat transfer and change of phase. The fluid flow pattern and its control are most important in the improvement of steel quality. Due to the high flow rate involved in the process, the flow becomes inevitably turbulent and turbulent modelling is important in addressing the real steel flow pattern. In this respect, various mathematical models were developed to investigate fully-turbulent, transient steel flow, and compare them against water model or real caster measurements. Furthermore, the complex transient nature of steel/slag interface needs to be understood as it has an important influence on the CC process and affect the quality of the steel produced. The slag layer has many functions: it protects steel from oxidation, it controls the horizontal heat transfer towards the mould and traps inclusions that float to the surface [23, 24]. The breakup of this interface by turbulent wave action may entrain impurities into the product. Additionally the liquid slag infiltrates into the gap developing between the mould and the solidifying shell during mould oscillation, lubricating the steel shell (Figure 1.3) as it is being extracted.

As already mentioned the presence of argon gas in the mould disturbs the steel/flux interface and affects the flow pattern due to the buoyancy forces generated. Argon gas prevents the SEN nozzles from clogging and the floating bubbles carry inclusions to the surface producing cleaner steel. From another point of view, the bubbles plus inclusions may become entrapped into the solidifying steel before they have the change to escape, creating important line defects. Free surface behaviour and particle tracking for the bubbles are described mathematically using multiphase techniques such as Lagrangian and Eulerian approach [25,

26, 27]. Heat transfer and solidification are linked strongly with the flow pattern and the motion of the slag/steel interface. For instance, low fluctuation and flow velocities prevent the re-entrapment of mould fluxes. In contrast, low steel flow rate can lead to freeze the meniscus, forming subsurface hooks [28, 29]. In the best case scenario the hot flow must reach the surface quickly, achieving a hotter meniscus and avoiding freezing problems [30].

The need to control the strong flow from the SEN jets, led to the application of electromagnetic forces and this topic was also extensively studied, as an important factor for the stability of steel flow in the mould. The electromagnetic devices used can be divided into electromagnetic stirrers (EMS) [31, 32, 33] and electromagnetic breakers (EMBr) [34, 35, 36] which mostly investigated by computation model.

Due to the complexity of each phenomenon present in the continuous casting process, the emphasis in each study is to develop a simplified model, separating for attention specific tasks so as to enhance the understanding of each phenomenon individually. Then each phenomenon can be coupled with others using empirical constants or by making reasonable assumptions [37].

Concerning the above complex phenomena and their related investigations, the literature can be divided into five categories.

## ***2.1 Fluid flow of liquid steel including turbulence model.***

### **2.1.1 Metal flow pattern in the mould and the SEN**

The liquid steel jet from a Submerged Entry Nozzle (SEN) reaches the narrow face of the caster, where it splits into a large lower loop in the casting direction and a small upper loop which flows back to the SEN (Figure 1.3). The upper loop is considered most influential in affecting the wave amplitude of the meniscus, hence the flow field in the slag layer. Based on previous research [38], there are indications that the back flow loop brings inclusions back to the nozzle which may then get clogged. In this respect, an understanding of flow patterns in the mould is of paramount importance.

Observations from experiments and numerical results show that the two loops are affected by several parameters, such as the nozzle shape, immersion depth, downward angle of the nozzle and steel flow rate [39, 40, 41]. Using PIV measurements, Xing-Guo et al. [39] demonstrate more stable meniscus behaviour can be obtained by increasing the immersion depth, since the flow velocity in the jet is decreased. Moreover, almost the same flow pattern is observed in case of a 30° nozzle angle for the four immersion depth tested (50 mm, 100 mm, 150 mm and 200 mm) but there is an effect on the fluctuation velocity of the meniscus. Their results corroborate with previous observations [40, 42] which also state that the jet angle mainly depends on the angle of bottom edge of the port than on the top. In addition, flow in the upper jet decrease with increasing the angle of the nozzle, hence the meniscus becomes steadier. Another work [43] examines the water-air flow pattern at the port outlet, by computational results verified with PIV measurements. It is important to note that in this study the numerical domain is restricted only to the nozzle (the mould is excluded) in order to reduce computation time. Despite the limited domain, the authors manage to calculate the jet characteristics by the numerical solution at the port outlet. They observed that the downward jet contains only a small amount of gas with strong vortex, with upper jet containing over of 70% of the gas and flowing upwards due to buoyancy.

An essential issue for several researchers is the accurate description of the molten steel/slag interface. Anagnostopoulos et al. [44] investigated flow near the interface surface using a fixed mesh surface tracking method, known as the volume of fluid (VOF) method [4]. This group found that the particular design of the SEN examined causes flow reversal into the nozzle and the wave height increases with casting speed. The results are compared with available experimental data obtained in a water-oil mould model for various flow rates and immersion depths of the submerged entry nozzle. The VOF method was considered also by Ramirez et al. [45] with the purpose of examine the meniscus stability. This group ascertained the amount of flow reversal in the upper edge of the port which depends on casting speed, design of SEN and port size. At low casting speed, they found a large amount of backflow in the upper edge of the nozzle port due to the small energy dissipation in the narrow faces. On the other hand, high casting speed dissipates large amounts of energy at the nozzle wall, leading to weaker upper flow and hence to the almost total elimination of back flow (see Figure 2.1). In addition they observed that the meniscus instability in low casting speeds occurs in the region surrounding the nozzle and in the mould corner high casting

speeds. However, the amount back-flow mainly depends on the angle of the two edges of the SEN port. According to Thomas et al. [43, 46] results (experimental and numerical), this unnecessary backflow in the nozzle can be avoided using a particular design of a SEN port, with a  $40^\circ$  down-facing upper port edge and  $15^\circ$  down-facing lower port edge.

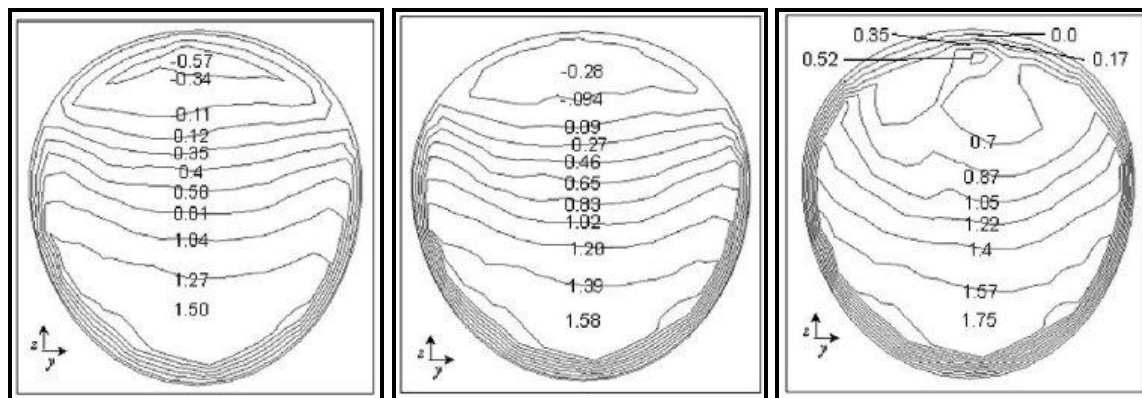


Figure 2.1: The velocity field in the plane of SEN port: a)  $V_c=0.8\text{m/min}$ , b)  $V_c=1.2\text{m/min}$  c)  $V_c=1.8\text{m/min}$  [45]

### 2.1.2 Turbulence model

The effect of the turbulence used in simulations has been investigated by several authors [45, 47-50] as it is critical not only for the metal flowfield behaviour but also for the heat distribution and the flux layer. The standard  $k-\varepsilon$  model, based on Reynolds Averaged Navier Stokes (RANS) approach, is the most widely used in many applications. This model was developed to describe steady state problems [51]. In modelling the continuous casting of steel, in areas with low Reynolds number, damping functions are vital in order to take care of viscous damping. Modifications in turbulence models were introduced in both  $k-\varepsilon$  and  $k-\omega$  in previous collaboration between IRSID (now AMR) and the University of Greenwich [47, 52]. Their results showed that a newly developed damping function used to multiply the effective viscosity gave the best agreement with experiments.

$$f_\mu = \min \left[ 1, \frac{(\rho\kappa^2)^{1/3}}{45\mu\varepsilon} \right] \quad (2.1)$$

Where  $\rho$  is the density,  $\mu$  is the effective viscosity,  $\kappa$  is the kinetic energy and  $\varepsilon$  dissipation rate. The other two functions of this group are

$$f_{\mu} = 1 - \exp\left[-\frac{\rho\kappa^2}{25\sqrt{3/2}\mu\epsilon}\right] \quad f_{\mu} = \exp\left[\frac{-3.4}{\left(1 + \rho\kappa^2/50\mu\epsilon\right)^2}\right] \quad (2.2)$$

The last function was also used by Wiwaranamataphee et al. [48] with additional multiplication of the square of liquid fraction in the damping function, to model a moving phase-change boundary and turbulent flow in the mould.

Thomas et al. [53, 54] analysed turbulence flow using the k- $\epsilon$  model, steady-state fluid and heat transfer using a finite element model to simulate one-quarter of the mould. They found that  $k$  and  $\epsilon$  values at the inlet affect the flow as increasing turbulent kinetic energy appears to increase the jet angle but increasing dissipation rate decreases it as depicted in Figure 2.2. In addition, they investigated the influence of the turbulent Prandtl number in heat transfer which it is increasing the overall temperature and decreases heat flux. Good comparisons were obtained using boundary inlet values for turbulent kinetic energy of  $k=0.0502\text{m}^2/\text{s}^2$  and viscous dissipation  $\epsilon=0.457\text{m}^2/\text{s}^3$  throughout the computational domain. The inlet velocity for the above investigation was computed by performing a mass balance equation in two dimensions (the nozzle length  $\times$  nozzle outlet velocity equal to the casting speed  $\times$  mould outlet width).

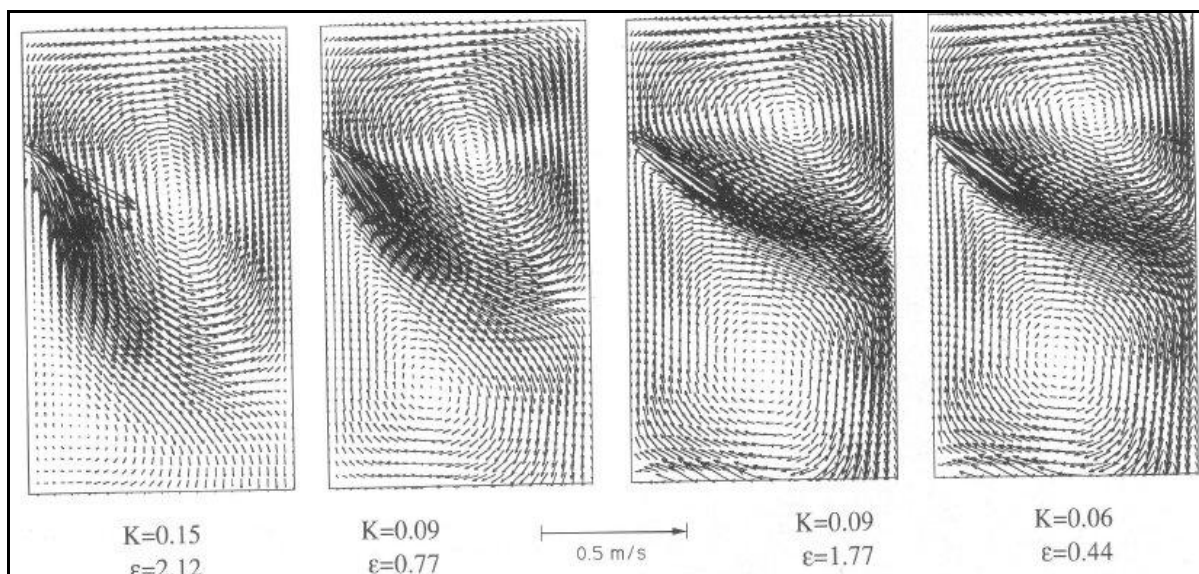


Figure 2.2: Effect of k- $\epsilon$  inlet values on calculated velocities in the water model [53, 54]

Thomas et al. [30, 46, 55] have considered the capability of several turbulence models. The time averaged k- $\epsilon$  model predicts accurate quantitative results with the least computation effort in a steady flow field but has difficulty with transient phenomena such as flow oscillation. The Direct Numerical Simulation (DNS) is more accurate but requires a very fine mesh to resolve all the turbulence length scales. As a result, a full geometry of continuous casting cannot be resolved with a DNS model, due to the unreachable computation time. The Large Eddy Simulation (LES) model is the current trend for simulating turbulence in continuous casting. Transient features of the flow field can be better predicted using the LES model [46, 56, 57]. The latter requires a fine enough mesh to resolve the large scale eddies, which lead to an increase in computational cost. The small scale eddies are assumed to be isotropic and are computed with a Sub-grid scale (SGS) model [30]. The accuracy of this method has been demonstrated by qualitative and quantitative comparisons with PIV and plant measurements. Comparisons between k- $\epsilon$  model and two LES approaches demonstrate the same downward jet angle and similar time-averaged flow patterns as with PIV measurements (Figure 2.3). However, both LES and PIV can capture the changes between smaller structures and vortices and the single large recirculation structure. This model is still not tested in free surface phenomena.

In this thesis, it was observed that performing simulations with a 2<sup>nd</sup> order in time scheme and the standard k- $\epsilon$  model can overcome the excessive eddy viscosity. Quantitative evaluation of this work has been achieved by activation of a 2<sup>nd</sup> order scheme and k- $\epsilon$  model, which aid the accuracy of the mathematical model. This model enhances, understanding of the flow pattern in continuous casting process.

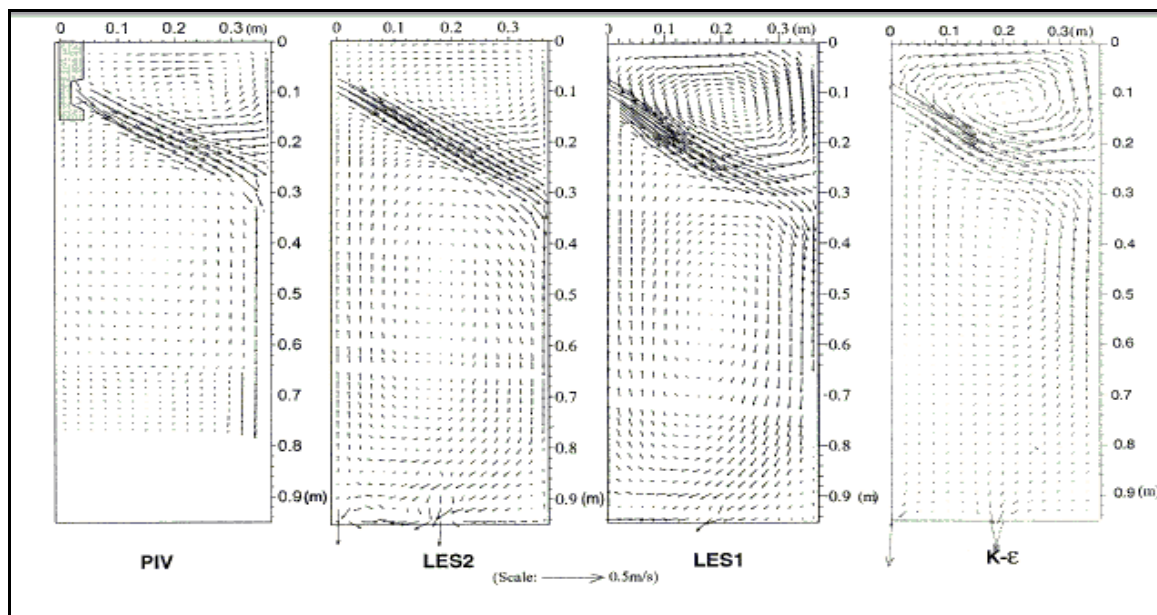


Figure 2.3: Time averaged velocity field in the middle plane [46].

## 2.2 Predictions of heat transfer, solidification and chemical reaction

Despite a plethora of studies [58-65] on heat transfer and solidification these are still many areas of continuous casting where further improvements are needed due to the important role of heat transfer in the success of the process. In plate casting, the molten steel is delivered to the mould via a nozzle and it reaches the narrow face of the mould at the impingement point, where a large peak of heat flux occurs (Figure 2.4). Furthermore, the meniscus region close to the narrow faces is the coolest region, which is important to shell solidification as it can lead to freezing of the meniscus [59]. Heat transfer to the top of the metal pool governs the melting of the protective flux powder, leading to a molten flux layer. The behaviour of this layer has a very important role to play in the efficiency of the process, since it affects several quality imperfections. It was observed that in high steel flow rates it causes the steel flux interface to become wavy because of the increasing of shear velocity in the bottom of flux layer. The latter affects flow and heat transfer in the liquid flux. As a result the flux may become entrained in the steel jet and trapped in the solidifying shell. On the other hand low steel flow rates may cause breakout, which is most common at the mould exit [60, 62].

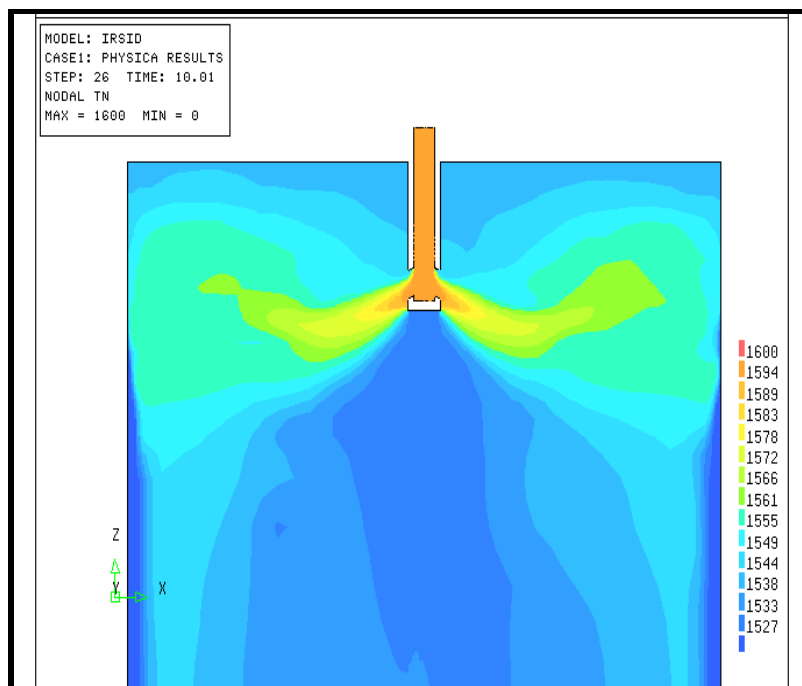


Figure 2.4: Temperature field in the middle plane [52].

Mc David et al. [66] coupled fluid flow with the thermal behaviour of flux layers (Figure 2.5) in a three-dimensional steady model using finite-element package, FIDAP. They established the importance of the flux layer plus the effect of its viscosity and thermal conductivity using temperature dependent properties. Lower liquid flux viscosity assisted better convective mixing, hence higher consumption and better quality. However the liquid flux viscosity has little effect on the liquid layer thickness near the meniscus of the narrow faces. In addition, shear velocity in the bottom of the slag layer changes from zero at the edges to a maximum midway between the narrow faces and the SEN. Their results highlight the vital role of metal flow, and the need to investigate its influence in the flux layer and hence the steel quality. Recently, another group led by Thomas [61], investigated the effects of natural convection, shear velocity in the interface and the temperature dependent viscosity using the finite volume code FLUENT. They found that the variation of Rayleigh<sup>1</sup> and Nusselt number<sup>2</sup> on fluxes is analogous to correlations for fluids with constant viscosity. Natural convection is suppressed for realistic fluxes and the Nusselt number increases linearly with increase of shear velocity. The effect of mould flux properties on heat transfer and shell thickness (in a billet during continuous casting) were investigated by Saraswat et al. [62]. They stressed the great importance of thermal resistance as the main factor affecting the horizontal heat

<sup>1</sup> The **Rayleigh number** characterizing the strength of the natural convection and the fluid properties

<sup>2</sup> The **Nusselt number** is the ratio of convective to conductive heat transfer across (normal to) the boundary

extraction from the shell. In addition, increasing the break temperature led to a thinner shell due to the lower heat transfer.

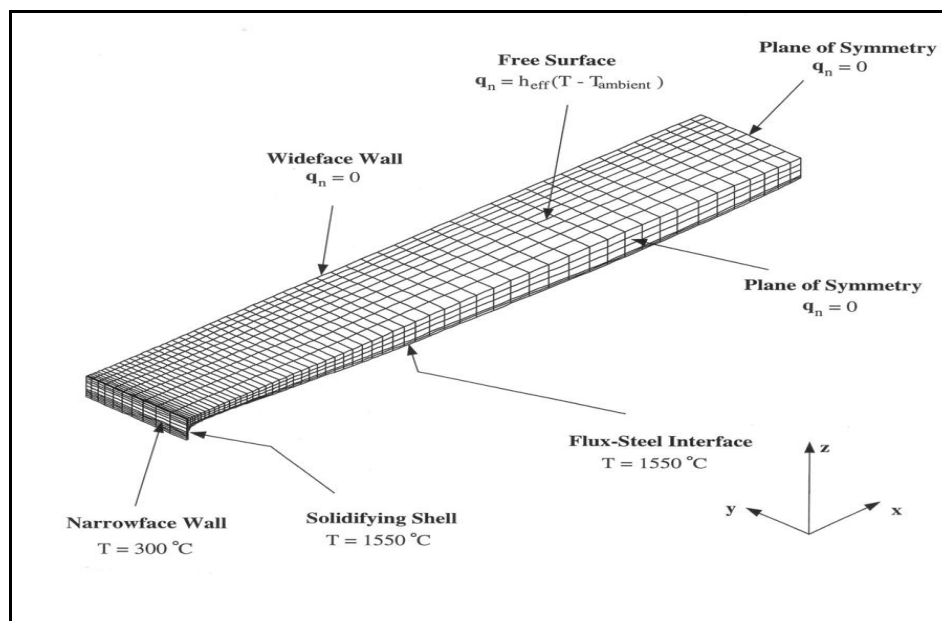


Figure 2.5: Thermal boundary condition of flux layer [66].

Zhao et al. [63] have observed that the average rate of superheat flux is significant because it can slow down solidification of the shell. They found, using LES turbulence models, that both the drag effect of the shell and natural convection have no influence in the flow pattern and temperature field. According to their observations, the flow alters the temperature in the steel pool. The temperature is expected to be higher, mainly in the meniscus region to avoid oscillation and subsurface hook formation, and hence to improve the quality of the metal. The work of this group was used for validation by Alizadeh et al. [64]. This research presents a new analytical model approach with a general relation between strand surface temperature, conductivity of the steel, pouring temperature, casting velocity, distance for the meniscus, volume rate of cooling water and heat flux density at the meniscus. The results show that the simple analytical model is applicable for strand temperature and solidified shell thickness. An advantage of the semi-analytical models is their controllability with convenient parameters (casting velocity etc).

A complete heat flow model was developed by Meng and Thomas [65] including transient 1-D solidification of the steel shell, movement of the slag layer in the air gap and 2-D steady heat conduction within the mould wall. Although the model is simple, it predicts several

related phenomena of the heat transfer in the mould and spray regions, for instance the thickness of solidified slag layer, heat flux profiles in the wide and narrow faces, effect of oscillation marks and boiling in the water channel. However, they were unable to examine transient phenomena (mould oscillation, formation of defects during initial solidification).

Heat conduction in the solidifying shell was solved using the 1-D transient heat conduction equation, which applying chain rule becomes

$$\rho_{steel} C p_{steel}^* \frac{\partial T}{\partial t} = k_{steel} \frac{\partial^2 T}{\partial x^2} + \frac{\partial k_{steel}}{\partial T} \left( \frac{\partial T}{\partial x} \right)^2 \quad (2.3)$$

where  $C p_{steel}^*$  is the effective specific heat,  $\rho$  is the density,  $T$  is the temperature and  $k_{steel}$  is the conductivity of steel.

Heat flux leaving the steel to enter the mould,  $q_{int}$  depends on the effective heat transfer coefficient in the gap,  $h_{gap}$ , and the differences between the surface temperature of the steel shell,  $T_s$  and hot face of the mould,  $T_{mould}$ . Heat conduction depends on thermal resistance of oscillation marks, liquid slag, solid slag and air gap if it exists as shown below:

$$q_{int} = h_{gap} (T_s - T_{mould}) \quad (2.4)$$

$$h_{gap} = 1 / \left( \left( r_{contact} + \frac{d_{air}}{k_{air}} + \frac{d_{solid}}{k_{solid}} \right) + 1 / \left( 1 / \left( \frac{d_{liquid}}{k_{liquid}} + \frac{d_{eff}}{k_{eff}} \right) + h_{eff} \right) \right) \quad (2.5)$$

### 2.3 Bubble particles and droplets behaviour

Bubble, particle and droplet injection is a main concern in the area of metallurgical processes, in view of the fact that it is a key factor of production and affects final cleanliness. Argon gas may be injected into the mould through the nozzle to reduce nozzle clogging, which is a major factor of low productivity and product quality. In contrast, argon injection increases quality defects due to the higher mould level fluctuation and bubble entrapment by the shell

or near the meniscus initiated surface cracks [67, 68]. Argon injection also affects the flow pattern in the nozzle and the mould and tends to change the jet due to the buoyancy forces. Previous water model measurements [69, 70] have observed that single flow pattern is more likely with high gas injection, small SEN submergence depth and small casting speed. The double roll flow pattern is mainly induced by large casting speed, large SEN submergence depth, and small gas flow rate [71]. In general, argon gas reduces the momentum of metal flow and the meniscus velocity, thus the control of flow pattern can be achieved by balancing the molten steel flow rate and argon gas flow [72]. In a later investigation, Kuno et al. [73, 74], applied a suitable ElectroMagnetic Level Stabilizer (EMLS) with argon gas. However, considering their results the braking ratio with argon gas case is much larger than without argon gas.

Regarding Lagrangian particle tracking Croft et al. [27, 52] characterize the motion of each particle by integrating the particle force balance equations, where the first term on the right hand side represents the drag force, which is always opposite to the motion direction. The second term is the buoyancy force due to gravity:

$$\frac{du_p}{dt} = -\frac{3}{4} \frac{C_d u_p \rho}{d_p \rho_p} |u_p - u_i| + \frac{(\rho_p - \rho) g}{\rho_p} = F_D + F_b \quad (2.6)$$

where the subscript  $p$  indicates particle values, other values are those associated with the metal,  $d_p$  is the diameter of the particle and  $g$  the gravity. They used two different options to calculate the drag coefficient.  $C_d$ : a) bubbles were assumed to remain spherical and behave like a rigid body (appropriate for bubbles  $<1$  mm), b) a sophisticated drag coefficient which is sensitive to bubbles shape variation. Results have shown that small bubbles follow the flow and large bubbles float towards the surface. Moreover, the effects of break-up and coalescence processes were considered by Gardin et al. [75, 76], for predicting bubbly air-water flow in a downward vertical nozzle. They used a mixed Eulerian-Lagrangian motion model considering the forces of: drag transverse lift, added mass and buoyancy. They successfully represented the bubbles' void fraction and obtained excellent validation between measured and calculated velocity fluctuation. According to their results the most important forces to predict gas and liquid velocities are the added mass, the drag lift forces and bubble distribution.

Yuan et al. [77] studied the argon bubbles movement in the nozzle using a 3-D finite difference model which has been developed using an Eulerian multiphase model in FLUENT. The motion of spherical inclusion particles in the mould was simulated using a Lagrangian approach. This model considered the balance of ten different forces. The particle transport equation includes six hydrodynamic forces

$$m_p \frac{du_p}{dt} = F_D + F_L + F_{Press} + F_A + F_H + F_G \quad (2.7)$$

where  $F_D$  is the steady-state drag force,  $F_L$  the lift force,  $F_{Press}$  the pressure gradient and stress gradient forces,  $F_A$  the added mass force,  $F_H$  the Basset history force and  $F_G$  the gravitational force. According to their model, four additional forces may act when the particle is very close to the solid-liquid boundaries, which are the lubrication force, the Van der Waals interfacial force, the surface energy gradient forces and the reaction force. According to their experiments, argon bubbles size increase with increasing gas flow rate and decreasing steel flow rate. As expected, most argon bubbles move through the upper recirculation zone in the mould and few small bubbles enter the lower recirculation zone and become entrapped at a characteristic downstream distance of the strand.

Zhang et al. [78] developed a small-scale model to describe the entrapment of inclusion by bubbles (Figure 2.6) using a Lagrangian approach. They found that bubbles smaller than 3mm tended to be spherical 3-10 mm were spheroidal and bubbles larger than 10 mm were spherical-cap-shaped. This research also showed that the flow pattern around bubbles with attached solid inclusions was similar to that of flow around a solid particle. As previous studies indicated small particles (<1 mm) follow the flow and circulate more deeply than large ones; instead bubbles more than 1mm mainly move in the upper recirculation loop. Attached inclusions increase the bubbles density but do not affect the motion as the density is much smaller than that of molten steel. In addition the removal of slag particles entrained from the top surface depends on the particle's size, leading to product defects.

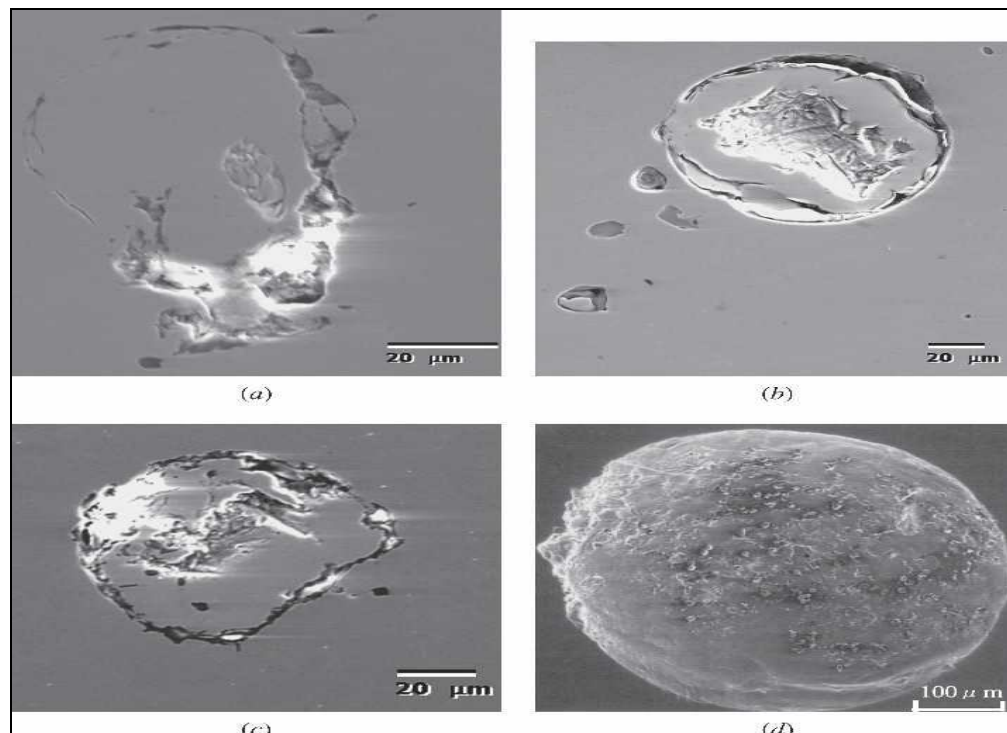


Figure 2.6: Inclusions outlining the former surface of bubbles [42].

## 2.4 Mathematical modelling and water model configuration

For validation, mathematical models and calculations are commonly compared with physical water models and experimental measurements. Thomas et al. [79, 80] provided a comprehensive review of previous works that have successfully investigated fluid flow phenomena employing a physical water model. In addition their review gives a brief discussion of the various advanced mathematical models used, physical properties and computational models employed in the mould region of a continuous caster. As mentioned earlier, a plethora of investigators declare that the flow pattern, not only in the mould but also in the nozzle, is affected by water flow rate, gas flow rate and the immersion depth [44, 45, 46, 83]. Most cases in the literature combine flow with a liquid flux layer or with argon flow. Nevertheless, only a few researchers developed a capable model, to couple the water/oil (steel/slag) interface deformation and its influence due to the gas [52].

Bai et al. [40,43] used an Eulerian multiphase model within the finite volume program CFX developed to simulate two-phase turbulent flow of liquid steel and argon bubbles in a slide gate nozzle. The flow patterns observed in the experiments with the validation nozzle agree closely with the numerical simulation results. Their velocity comparison between the particle-

image-velocimetry (PIV) measurements and model predictions was satisfactory except that the velocity predictions were consistently larger than the measurements.

An interesting study using the Finite-Volume numerical method to simulate turbulent flow, heat transfer and solidification in the caster in the presence of a moving interface and argon bubbles was provided by Croft et al. [52]. Continuum transport equations to be solved represented conservation of transport quantities within a mixture fluid. The two-phase flow problem: heat transfer and the flux-metal interface were solved using the Scalar Equation Algorithm (SEA) [81] and transient heat flow was described by the energy equation. This work used an early version of the FV code PHYSICA and it forms the foundation of the research contained in this Thesis.

Panaras et al. [82] obtained numerical solutions of the water-air free-surface oscillation and free surface shape and found that the free-surface stability criterion of  $H/\lambda = 0.21$  (wave height/wave length) is in agreement with their calculation. They observed that the exiting angle is not significantly affected by flow oscillation of the free surface and FFT analysis of the motion of free surface shows a peak at 0.195 Hz which can be associated with the instability of the free surface. Further continuation of this work by Theothorokakos et al. [84] has simulated a water model experiment in order to get further insight of the oil/water interface and its breakup mechanism. It was found that the oil/water interface wave amplitude increased in comparison to the air/water interface.

Another experimental and numerical comparison has been developed by Miranda et al. [85] using a one-third scale model. Power density spectrum analyses of the results showed a main peak at 1.2 Hz and another two frequencies of 1.8 Hz and 2.1 Hz whose contribution to the free surface dynamic behaviour depend on the process parameters, such as water flow rate and immersion depth. For constant depth, the wave amplitude increased as the SEN output port velocity increased too. For constant exit port velocity, the wave amplitude increased as the immersion depth increased. In contrast for a certain value of the immersion depth, surface velocity decreased as the SEN immersion depth increased.

Water model configuration results, from Ramos-Banderas et al. [86], demonstrate two flow regimes: a bubbly flow or an annular flow in the SEN. In the first case the water and gas are

well mixed and the two jets at the exit ports are symmetrical, causing low pressure in the impingement point due to energy losses. For annular flow, the liquid flow separates from the gas, causing high impingement pressure as a result of the small amount energy losses.

Preliminary works up to this point were mainly to model the slag layer assuming either a fixed top layer [87, 88] or used an observed experimental interface. The slag layer was assumed according to steady measurements, and coupled with steel flow through the shear stress distribution at their interface [66, 89].

$$\tau_{zx} = \mu \left. \frac{\partial u_x}{\partial n} \right|_{flux} = \mu_{steel} \left. \frac{\partial u_x}{\partial n} \right|_{steel} \quad (2.8)$$

Where  $u$  is the horizontal velocity component and  $\mu$  is the effective viscosity of the material. Qualitative and quantitative understanding of the hydrodynamic aspect of water/oil (steel/slag) interface will be addressed in the following chapters. Furthermore, the influence of the gas in the fluid flow pattern and the meniscus deformation will be demonstrated. Predictions of transient phenomena and steel flow stability were determined by spectrum analyses. However, from the numerical point of view, there is no established validation of the hydrodynamic behaviour of the slag layer couple with argon injection.

## ***2.5 Predictions of mould oscillation and applied magnetic field***

A thin shell of metal next to the mold walls solidifies before the metal section exits the base of the mould. The mould is oscillated vertically to prevent the strand shell sticking to the water cooled copper walls and causing a breakout. In contrast, hooks and oscillation marks form due to the solidification near the meniscus during mould oscillation [90]. Ojeda et al. [91, 92] provided a brief review of oscillation cycle and developed a model to describe the oscillation marks and the formation of a slag rim, which is due to the solidification of molten slag in the meniscus region, during mould oscillation. This transient model assists the understanding of several oscillation phenomena such as the oscillating slag rim, the predicted pressure in the gap between mould and the shell, liquid flux consumption behaviour and mechanics of hook formation and shape. Observations of the results have indicate that

- The oscillating solidified slag rim controls the flow pattern in the meniscus.

- Pressure in the gap between the shell and the mould increases during negative strip period which moves the steel/slag interface away from the mould wall and decreases as the mould increases its upward velocity.
- Overflow starts earlier with a more severe solid slag rim.
- Computations and experimental data show that the overflow event can start at different times.
- The heat flux peak occurs ~1cm below the meniscus region.

These phenomena, as illustrated in Figure 2.7, are of paramount importance, as they cause several quality problems due to the entrapment of mould powder, local crack formation and impurities. The flow pattern of liquid slag in the meniscus was considered by Ramirez-Lopez et al. [93]. This investigation showed good corresponding results with the addition of the thermal evolution which is changing the thickness of liquid and solid slag layer. Good prediction of slag thickness and heat fluxes at various casting speed were found and good comparisons to previous results and plant measurements were achieved.

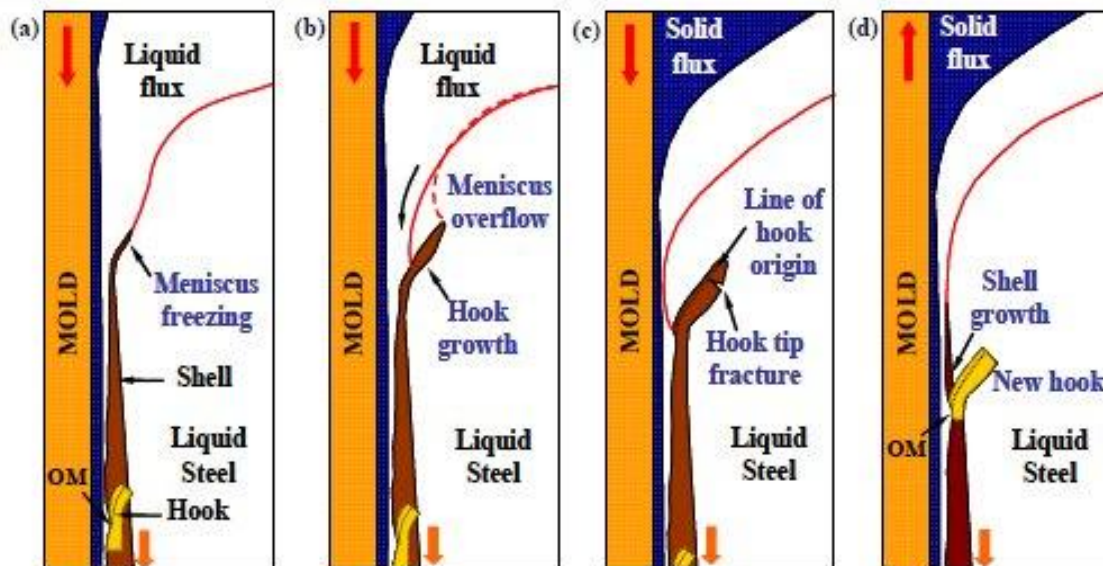


Figure 2.7: Schematic formation of curved hook and meniscus solidification. (Courtesy B. G. Thomas [94])

In order to reduce the surface velocity, many researchers have investigated the application of electromagnetic forces to control the steel flow. Kubo et al. [72, 74] employed electromagnetic force using Electro Magnetic Level Stabilizer (EMLS) with argon gas. Electromagnetic force applies a low frequency alternating magnetic field that moves from the

narrow face of the mould to the mould centre below the nozzle exit. Main observations by this group were firstly the effect of EMLS system in the surface flow and the supported influence of argon gas in the surface flow towards the narrow faces. From calculation and observation of the real casting their method seems to be applicable and optimum intensity of a magnetic field for the flow control should be chosen in consideration with argon gas.

Baokuan et al. [95] investigated the effect of argon gas injection and the static magnetic-field application in the continuous casting process. They found that by applying one magnets on the meniscus and one below the nozzle, the velocities in the bulk were significantly suppressed, also the velocities at the top surface are too small which led to a freezing meniscus. When argon gas was also applied with magnetic-field the external flow of gas plume was significantly suppressed, flotation of gas bubbles was not affected directly by magnetic field. The effects of magnetic field on interface control were not investigated in this Thesis.

## *Chapter III*

### **3 Modelling Approach**

The development of computer power, in recent years, has become an important factor in the improvement of mathematical models, and in a better understanding of the physics behind all aspects of the process of continuous casting. Due to the several complex phenomena involved in continuous casting, it is impossible to model all of the phenomena together at once. As a result, each mathematical model requires a specific issue of interest, and it is important to validate it against the theoretical expectations and experimental results on both water model configuration and real plant measurements [96]. The main aim of this thesis is to demonstrate the effectiveness of the multi-physics code PHYSICA in the simulation of the continuous casting process of steel production and in doing so advance our understanding of the physical mechanisms involved. The ensuing research thesis concerns the development of a numerical model in the simulation of the continuous casting (CC) of steel, and as a long-term industrial goal the improvement of steel quality. Assuming that the casting process is a steady state problem fluid flow and heat transfer across the copper mould are initially investigated using a flat fixed horizontal level to describe the protective slag layer. However, the primary objectives of this thesis are: firstly to model the dynamic behaviour of the slag layer covering the steel and secondly to study the complex interaction of the Argon gas on the slag layer and the fluid dynamic behaviour of the liquid metal in the mould region. To fully understand this behaviour and validate the model, experimental measurements were carried out in a water model by ArcelorMittal Research (AMR) using Laser Doppler Anemometry (LDA) technology.

#### **3.1 General framework**

The initial aim of the project is the implementation of heat transfer and the solidification across a continuous steel casting mould. For this purpose, 3-D dimensional geometry of the mould region has been built, based on industrial geometry parameters provided by AMR. A suitable hexahedral mesh has been created according to PHYSICA requirements, utilizing the HARPOON mesh generator software. As a research effort continuing from previous work

carried out at the University of Greenwich [89], the continuity, flow, heat transfer, solidification and turbulence equations have been solved according to appropriate boundary conditions as described in detail in the following sections. Although the results with the HARPOON mesh, as will be seen in the next section, are encouraging, this mesh was not suitable for capturing free surface motion. This occurred due to the high non-orthogonality of the mesh on some cells in the SEN and also due to the sudden jump in the mesh size from the nozzle to the mould region. After several attempts and in an effort to reduce set up time owing to the reconstruction needed in the HARPOON mesh, a pre-existing unstructured finite-volume mesh has been used to investigate free surface movement and particle tracking, which was supplied by AMR (constructed using the Gambit mesh generator software).

The scientific objective of this initial effort is to develop a numerical model in order to determine the fluid flow patterns of steel and to investigate the transient behaviour of the slag/steel (oil/water) interface using a water model configuration. A three dimensional computation fluid dynamics model has been validated using water measurements in order to understand the wave behaviour and the mechanisms that lead to the break-up of slag-steel interface, which is directly connected with transient flows. In addition, the behaviour of argon bubbles has been investigated together with the disturbance of the steel/slag interface caused by the buoyancy forces of argon. The model includes a specially formulated interface tracking scheme using the Counter Diffusion Method (CDM) to simulate the oil behaviour and a Lagrangian representation of argon bubble tracks to study the influence of injected gas on the liquid steel flow (due to buoyancy) and on the surface behaviour.

Finally the heat transfer between slag and steel in an industrial configuration is studied, which is solved under transient conditions. Therefore a new mesh, corresponding to industrial geometry parameters, was created using an extended mesh building tool: the MB3 mesh builder which is inbuilt in PHYSICA. These multi-phase interactions involve the melting of the flux powder and the formation of the slag layer plus the formation of a thin steel strand adjacent to the mould walls, in the first stages of solidification.

### **3.2 Steady-state model**

Initially we study a typical three dimensional steady state flow model assuming a flat top molten surface at a fixed level and covered by the slag layer. A linear temperature-liquid

fraction relationship is used to model the formation of the solid skin outside the mould. The latent heat effect on local temperature is included in the energy equation through a volumetric source term and the presence of a mushy zone extending inwards towards the skin is represented through a Darcy resistance term in the momentum equation. The simulation of the casting solves fluid flow, heat transfer and turbulence considering the following equations.

### 3.2.1 Fluid flow

A typical three-dimensional fluid flow model below solves the continuity equation and momentum equations

$$\frac{\partial \rho}{\partial t} + \nabla \cdot (\rho \underline{u}) = 0 \quad (3.1)$$

$$\frac{\partial}{\partial t} (\rho \underline{u}) + \nabla \cdot (\rho \underline{u} \underline{u}) = \nabla \cdot (\mu \nabla \underline{u}) - \nabla p + \underline{S} \quad (3.2)$$

where  $\underline{u}$  is the velocity vector,  $p$  is the pressure,  $\rho$  is the density and  $\mu$  is the effective viscosity. The vector  $\underline{S}$  represents body forces and the influence of boundaries. For solidification,  $\underline{S}$  represents a Darcy flow resistance provided by the solid phase,

$$\underline{S} = \frac{(1 - f_L)}{K} V \quad (3.3)$$

where  $K$  is the permeability coefficient of the mushy zone,  $f_L$  is the liquid fraction and  $V$  is the volume of the element.

### 3.2.2 Heat transfer and solidification

The energy equation with temperature as the solved for variable is given by:

$$\frac{\partial}{\partial t} (\rho c_p T) + \nabla \cdot (\rho c_p \underline{u} T) = \nabla \cdot (k \nabla T) + S_H \quad (3.4)$$

$k$  is effective conductivity and  $C_p$  is the specific heat capacitance. The source terms  $S_H$  represents heat transfer at the boundaries and change of phase. The evolution of latent heat  $L$  during solidification is given by

$$S = -L \frac{\partial f_L}{\partial t} - L \text{div}(\rho \underline{u} f_L) \quad (3.5)$$

where  $L$  is the latent heat of solidification,  $\rho$  is the density and  $\underline{u}$  is the velocity vector. The boundary conditions are of the form

$$S_B = hA(T - T_{amb}) \quad (3.6)$$

where  $A$  is the average of the area of the face and  $h$  is the heat transfer coefficient and  $T_{amb}$  is the ambient temperature.

The value of the liquid fraction is usually calculated from the formula

$$f_L = \begin{cases} 1 & \text{if } T > T_L \\ (T - T_S) / (T_L - T_S) & \text{if } T_S \leq T \leq T_L \\ 0 & \text{if } T < T_S \end{cases} \quad (3.7)$$

Where  $T_L$  is the liquidus temperature, the temperature above which the material is fully liquid, and  $T_S$  is the solidus temperature, the temperature below which the material is completely solid.

### 3.2.3 Turbulence model

Turbulence is a key factor in the continuous casting of steel. All the calculations use the k- $\epsilon$  turbulence model approach. This is a standard high Reynolds number model which is a switch on option in PHYSICA. Previous CFD computations performed by the University of Greenwich showed that the presence of an oil layer led to the suppression of interface oscillations, due to excessive diffusion whenever this model was used in a transient simulation with very small computation time-steps. To overcome this problem, an appropriate filter was introduced in the transient k- $\epsilon$  model [5, 52] which removes resolved turbulent energy from the k equation, thus reducing artificial diffusion. Brief investigations of the suitability of the k- $\epsilon$  turbulence model show that the filter also affects the mean value of horizontal velocity at the meniscus. Following various analyses it has been shown that

artificial damping can be avoided simply by using a second order numerical scheme. The next chapter contains a description of this scheme, and in addition to the results obtained using the k- $\varepsilon$  filter. It was concluded that, successful predictions of the dynamic behaviour in the meniscus, can be achieved using a second order scheme without the k- $\varepsilon$  filter.

The turbulent contribution in  $\mu$  in the equation (3.8) is calculated from the solution of the standard k- $\varepsilon$  model. The k- $\varepsilon$  model consists of the turbulent kinetic energy equation  $k$ :

$$\frac{\partial \rho k}{\partial t} + \text{div}(\rho \underline{u} k) = \text{div} \left( \left[ \mu_{lam} + \frac{\rho \nu_t}{\sigma_k} \right] \text{grad} k \right) + \rho \nu_t G - \rho \varepsilon \quad (3.8)$$

and its dissipation rate  $\varepsilon$

$$\frac{\partial \rho \varepsilon}{\partial t} + \text{div}(\rho \underline{u} \varepsilon) = \text{div} \left( \left[ \mu_{lam} + \frac{\rho \nu_t}{\sigma_k} \right] \text{grad} \varepsilon \right) + C_1 \rho \nu_t G \frac{\varepsilon}{k} - C_{2\varepsilon} \rho \frac{\varepsilon^2}{k} \quad (3.9)$$

where  $G$  represents the turbulent generation rate which is equal to

$$G = 2 \left( \left[ \frac{\partial u}{\partial x} \right]^2 + \left[ \frac{\partial v}{\partial x} \right]^2 + \left[ \frac{\partial w}{\partial x} \right]^2 \right) + \left( \frac{\partial u}{\partial y} + \frac{\partial v}{\partial x} \right)^2 + \left( \frac{\partial u}{\partial z} + \frac{\partial w}{\partial x} \right)^2 + \left( \frac{\partial w}{\partial y} + \frac{\partial v}{\partial z} \right)^2 \quad (3.10)$$

The Kolmogorov-Prandtl expression for turbulent viscosity is used in PHYSICA [1]

$$\nu_t = C_\mu \frac{k^2}{\varepsilon} \quad (3.11)$$

together with

$$-\overline{u_i n} = \Gamma_t \frac{\partial h}{\partial x_i} \quad (3.12)$$

where  $\Gamma_t$  is the turbulent diffusivity of heat and the values of empirical constants [136] in equation 3.8-3.11 are

$$C_\mu = 0.09, \sigma_\kappa = 1.0, \sigma_\varepsilon = 1.3, C_1 = 1.44, C_2 = 1.92$$

The Reynolds analogy between heat and momentum transport implies that the turbulent diffusivity is related to  $\nu_t$  by

$$\Gamma_t = \frac{\nu_t}{\sigma_t} \quad (3.13)$$

where  $\sigma_t$  is the turbulent Prandtl number [98].

The effective viscosity in the momentum equation is equal to the sum of the laminar viscosity and turbulence viscosity, and is calculated when the turbulence viscosity ( $\mu_t$ ) is known

$$\mu = \mu_{lam} + \mu_t \quad (3.14)$$

### 3.3 Transient model

A transient simulation is necessary to illustrate the coupling between free surface, fluid dynamics and bubbles. The Donor-Acceptor method [3, 4] was initially used to track the interface, but being explicit requires very small time steps of  $10^{-3}$ s, thus increasing computation time. To overcome this problem a new fully implicit method, the Counter Diffusion Method (CDM) [5] was used. This new method speeds up the computation time as bigger time-steps of 0.01s can be used without stability problems. The model then transports 1000 or more particles using a Lagrangian approach. The equations of motion and transport of representative samples of discrete particles are solved explicitly and the particles are tracked through the flow field until they exit the domain.

#### 3.3.1 Free surface tracking

The interface between the molten flux (oil) and the liquid metal (water) is modelled using the Scalar Equation Algorithm [81]. The continuity equation is adjusted to provide an equation

that represents volume conservations so that any problems caused by the discontinuity of density at the interface are resolved [99].

$$\frac{D(\ln \rho)}{Dt} + \nabla \cdot (\underline{u}) = 0 \quad (3.15)$$

where  $D/Dt$  is the substantial derivative term. To model the problem as a single phase flow, the momentum equation is then rewritten as

$$\frac{\partial}{\partial t} (\rho_f \underline{u}) + \nabla \cdot (\rho_f \underline{u} \underline{u}) = \nabla \cdot (\mu \nabla \underline{u}) - r \nabla p + \underline{S} \quad (3.16)$$

The factor  $r$  in the pressure gradient term,  $\nabla p$ , is given by:

$$r = \left\{ 1 + \phi \left( \frac{\rho_m}{\rho_f} - 1 \right) \right\}^{-1} \quad (3.17)$$

where  $\rho_f$  and  $\rho_m$  are the flux and metal (or oil and water) densities respectively. The mixture density and viscosity are based on the value of  $\phi$ , which is representing the position of the interface and gives the metal volume fraction in a control volume cell. The viscosity is then given by

$$\mu = \mu_f + \phi \left[ \left( \mu_m \frac{\rho_f}{\rho_m} \right) - \mu_f \right] \quad (3.18)$$

where  $\mu_f$  is flux viscosity and metal viscosity is metal viscosity  $\mu_m$ . The mixture density is

$$\rho = \rho_f + \phi(\rho_m - \rho_f) \quad (3.19)$$

Therefore, when  $\phi$  is equal to zero, the momentum equations will use the flux (oil) density and when  $\phi$  is one, the metal (water) density will be used.

### 3.3.1.1 The Counter Diffusion Method

The Donor Acceptor method, which is the original Volume of Fluid scheme, is initially used to capture the oil surface behaviour. This is an explicit formulation, with small time-steps of  $10^{-3}$  s being required in order to satisfy the *CFL* criterion [100], defined as:

$$CFL = (\delta t \cdot u) / \delta x \quad (3.20)$$

where  $\delta t$  is the time-step  $\delta x$  is the internal length of the cell and  $u$  is the velocity.

This criterion is necessary to avoid skipping completely a computation cell during material advection; the time-step should be less than the minimum time required to move material from one cell to another in the domain, as dictated by cell dimensions and velocities.. In essence, the time-step has to be reduced for fine mesh regions or in the case of large advection velocity in order to avoid diverging solutions. Using Donor Acceptor has forced the use of time-steps of 1ms or less which leads to an expensive computation simulation time. To speed up the computation time a new implicit method called *CDM* has been implemented.

When the source  $S$  contains the *CDM* corrections, a new auxiliary scalar called ‘marker’ is used. The value of the marker is copied to ‘phi’ instead of solving ‘phi’ with the free surface module. A counter diffusion ‘flux’ is computed for each internal cell when the face belongs to an interface cell. The artificial counter diffusion is calculated by the equation:

$$Q = C \cdot q \cdot (1 - \phi_{down}) \cdot \phi_{up} \quad (3.21)$$

where  $Q$  is artificial counter diffusion flux for each internal face,  $C$  is a constant used to adjust the local face normal velocity in the marker equation. The factor  $(1 - \Phi_{down})$  ensures that we do not push into a completely full cell and  $\Phi_{up}$  ensures that we do not take from cells without liquid;  $q$  is the current iteration convection flux which is used to transport all scalar variables [101].

$$q = |\underline{u} \cdot \underline{n}| \cdot A \quad (3.22)$$

where  $|\underline{u} \cdot \underline{n}|$  local face normal and  $A$  is the face area.

### 3.3.2 Particle tracking

A computational model has been developed to simulate the transport of particles. The model first simulates in an Euler framework the turbulent flow, heat transfer and free surface position as explained in the previous chapters. Coupled to this, a Lagrangian representation of 1000 and more argon bubble tracks was used to study the influence of injected gas on the liquid steel flow and fluctuating surface dynamics. The concentration of bubbles obtained from the Lagrangian computation is computed in any computational cell and used to adjust the local density, allowing for the effects of liquid displacement, buoyancy and local change in momentum. In this sense, the continuum equations representing the liquid are mixture equations for liquid plus gas.

Particle tracks are assumed to comprise swarms of particles (bubbles); each track entity carries a certain amount of gas mass, so that the total entering the inlet corresponds to the given flow rate. The number of individual bubbles in each track will then relate to the mass associated with the track. The particle velocity  $U_p$ , is then computed from the integral of the force balance equation:

$$m_p \frac{du_p}{dt} = (\rho_p - \rho_l)gV_p - \frac{1}{2}\rho_l V_{slip} |U_p - U| \frac{\pi d^2}{4} Cd - \frac{1}{2} m_p \frac{\rho_l}{\rho_p} \frac{du_p}{dt} \quad (3.23)$$

The first term on the right hand side of the above equation is the buoyancy force due to the gravity. The second term is the drag force, which is always opposite to the motion direction and the third one is an added mass force. This formulation includes the most significant forces of equation 2.5, expressing the volumetric displacement of fluid by the particles due to the buoyancy exchange and inertia changes affecting fluid and particle acceleration. In this model, the lift force, the pressure gradient force and the history forces are not considered as the main purpose of this research is to investigate influence of gas on the interface stability. The solution methodology begins by solving the flowfield assuming there is no bubble for the first 25 time steps. Then particle trajectories are computed, allowing for the effects of liquid displacement, buoyancy and local change of momentum. The free surface model is solved

again with the established changes in the flow field until new particles injected. The methodology illustrated is a variant of the Particle-Source-In Cell (PSI-CELL) model of Crowe et al. [102].

Equation (3.24) can be discretised as

$$\begin{aligned}
 U_p &= (U_p + S_u \cdot \delta_t) / (1 + F \cdot \delta_t), \text{ where,} \\
 F &= 0.75 \cdot C_d \cdot \rho_l \cdot V_{slip} / (d_p \cdot \rho_f) \\
 S_u &= F \cdot U_p + (\rho_p - \rho_l) \cdot g / \rho_f \\
 \rho_f &= \rho_p + \frac{1}{2} \rho_l \\
 V_{slip} &= U_p - U
 \end{aligned} \tag{3.24}$$

where  $F$  is the drag force on particle,  $S_u$  is the momentum force and  $C_d$  is drag coefficient. The particle time step,  $\delta t$  is chosen to give a selected number of steps in the current element. The minimum and maximum particle time steps are set through the PHYSICA user input file, INFORM (APPENDIX A). The bubbles' movement will mainly depend on the value of the drag coefficient,  $C_d$ . Two different assumptions have been used to calculate drag coefficient as a function of Reynolds numbers as described below:

Option 1:

$$C_d = \frac{24}{\text{Re}} \cdot (1 + 0.15 \text{Re}^{0.687}) + \frac{0.42}{1 + \frac{42500}{\text{Re}^{1.16}}} \tag{3.25}$$

Suitable for small bubbles with “rigid” surface – used in many bubble computations [103]

Option 2 : An alternative method [104], that assumes non-rigid surface and depends not only on Reynolds Number but also on Weber number are calculated as follows

$$\text{Re} = d_p V_{slip} / \nu, \quad \text{We} = \rho V_{slip} d_p / \gamma \tag{3.26}$$

where  $\gamma$  is the bubbles surface tension and  $\nu$  is the laminar viscosity.

The equations associated with the second method are:

$$i) Cd = 16 / Re, Re < 0.49,$$

ii)  $Cd = 20.68 / Re^{0.643}$ ,  $Re \leq 100$  this is the dirty water expression of Wallis [105] which the drag coefficient is calculated by the swarming correction equation,  $Cd = Cd(1 - Vfrac)^{-1.7}$  where  $Vfrac$  is the volume fraction of the particle swarm.

$$iii) Cd = 6.3 / Re^{0.385}, We \leq 8, Re \leq \frac{2065.1}{We^{2.6}},$$

$$iv) Cd = We / 3, We \leq 8, Re \leq \frac{2065.1}{We^{2.6}}, \quad (3.27)$$

$$v) Cd = 8 / 3, We > 8, Re > 100$$

The particles tracking scheme then proceeds as follows:

- i. The particles are randomly seeded just inside the SEN inlet or in a volume section in z axis, with a uniform distribution in the azimuthal direction at x and y axis.
- ii. Each random particle seed represents an equal fraction of inlet gas volume rate (2Nl/min, 5Nl/min<sup>3</sup>).
- iii. Particles are given an initial velocity close to the inlet velocity.
- iv. Particles are tracked through the domain at selected fluid computation time steps (every 25 time steps).

The time a particle spends in an element,  $\Delta t$ , is recorded and the particle volume fraction is adjusted at the end of air tracking by

---

<sup>3</sup> **normal litre (NI):**A unit of mass for gases equal to the mass of 1 litre at a pressure of 1 atmosphere and at a standard temperature, often 0 C (32 F) or 20 C (68 F)

$$V_{air} = \frac{\Delta t \left( \frac{\dot{m}_{air}}{N_p} \right)}{\rho_p} \quad (3.28)$$

where  $\dot{m}_{air}$  is the mass flow rate,  $N_p$  is the total number of particles and  $\rho_p$  is the density of particles. As a result main flow is fully coupled with the particle phase in respect to the density and momentum which is associated with volume fraction.

There is also a coupling of bubbles with the flow turbulence, which is important as it affects the dispersion of bubbles. The liquid phase velocity  $u$  used in the drag force is given by the sum of its fluctuating  $u'_i$  and average velocity  $\bar{u}_i$ . The present model refers to the stochastic model of Gosman and Ioannides [144], whose basic assumption is that particles are deflected by the eddies they cross. The model assumes an isotropic turbulence and that each of the components of the fluctuation velocity  $u'_i$  of continuous liquid phase follows a normal distribution with a mean value of  $\bar{u}_i = 0 \text{ m/s}$  and standard deviation of  $\sigma_T = \sqrt{(2/3) \cdot k}$  where  $k$  is the local value of the turbulence kinetic energy.

The fluctuating component  $u'_i$  calculated at a given particle time step, whose three components are equal for the assumed isotropy of turbulence, acts over a tracking time  $\Delta t$  which is the minimum of  $\Delta t = \min(\Delta t_e, \Delta t_r)$  where :

- i.  $\Delta t_e$ , lifetime of the local eddy the particle is crossing, given by:

$$\Delta t_e = L_e / |u'_g|, \quad (3.29)$$

where:

$$L_e = (C_\mu C_d)^{3/4} \cdot k^{3/2} / \varepsilon \quad (3.30)$$

is the eddy size, with  $(C_\mu C_d) = 0.09$  and  $\varepsilon$  is the rate of dissipation of turbulent kinetic energy;

- ii.  $\Delta t_r$ , transit time taken by the particle to cross the eddy, given by:

$$\Delta t_r = L_e / |u_g - u_p| \quad (3.31)$$

### 3.4 Water model details

The experimental rig, shown in Figure 3.1, has an adaptable full scale geometry according to Froude ( $Fr$ ) and Reynolds ( $Re$ ) numbers

$$Re = \frac{\text{Inertial forces}}{\text{viscous forces}} = \frac{u \rho l}{\mu} = \frac{ul}{\nu} \quad (3.32)$$

$$Fr = \frac{\text{Inertial forces}}{\text{body forces}} = \frac{u^2}{gl}$$

where  $u$  represents the flow velocity,  $\rho$  the density,  $\mu$  the dynamic viscosity,  $\nu$  the kinematic viscosity,  $l$  a characteristic length and  $g$  the gravitational acceleration. The kinematic viscosities of liquid steel and water at a temperature of approximately 20°C are close in value. In order to best represent the full scale model (table 3.1), the relevant dimensionless numbers of equation 3.32 have to be taken into account.. Thus, maintaining Reynolds and Froude criteria the steel flow pattern can be reproduce with water model, ensuring that the velocity ratios between the model and steel are the same at every location [96, 127]

The Reynolds similarity between water (w) model and real caster (s) indicate that

$$\left( \frac{ul}{\nu} \right)_w = \left( \frac{ul}{\nu} \right)_s \quad (3.33)$$

and since the steel and water have the same kinematic viscosities hence the equation 3.33 becomes

$$u_s = K u_w \text{ where } K \text{ is the length scale fcator equal to } l_w / l_s \quad (3.34)$$

Similarly, using Froude similarity it can be shown that

$$u_s = \sqrt{K} u_w \quad (3.35)$$

It is obvious from equations 3.34 and 3.35 that satisfying both Reynolds and Froude numbers is only possible with the use of full scale mode ( $K=1$ ). This water model use only the Froude similarity with a reduced scale factor of  $K=100/220$  (table 3.1).



Figure 3.1: Video stills of the water-model experiment performed by AMR (2009) without and with gas.

Water circulation is provided by a pump that draws water from the collector at the bottom of the mould and pushes it into the tundish located at the top of the mould. Different flow rates can easily be set. Both mould and SEN are transparent and they are located in a robust support.

	Industrial Case	Similarity Law	Scale Model
<b>Dimension of Mould(mm)</b>	1600x220	$L_{scale}=K.L_{real}$	727x100
<b>Immersion of the nozzle (mm)</b>	150	$L_{scale}=K.L_{real}$	68
<b>Internal diameter of the nozzle (mm)</b>	81	$L_{scale}=K.L_{real}$	37
<b>Vin=Inlet velocity (m/s)</b>	0.74 1.2 1.5	$V_{scale}=K^{1/2}.v_{real}$	0.5 0.8 1.018
<b>Qw=Liquid flowrate (m<sup>3</sup>/h)</b>	14 22.3 28.3	$q_{scale}=K^{5/2}.q_{real}$	1.94 3.1 3.94
<b>Qa=Gas flowrate (l/min)</b>	2.4 5.9	$q_{scale} = K^{5/2} . q_{real} \frac{T_{real} + 273}{T_{scale} + 273}$	2 5
<b>Temperature (°C)</b>	1500		20

Table 3.1: Water model parameters according to Froude similarity where  $K$  is the scale factor equal to 100/220 for the CC mould water model

Measurements are taken using Laser Doppler Anemometry (LDA) which is an optical technique for non-intrusive 1D, 2D and 3D point measurement of velocity and turbulence distribution [106]. The LDA measuring system consists of a two-component system. This method is based on the scattered laser light of a particle passing. The light intensity is modulated to create an interference fringe pattern between two laser beams. This produces parallel planes of high light intensity by the wavelength  $\lambda$  of the laser light and the angle between the beams  $\theta$  (Figure 3.2). Flow velocity information comes from light scattered by small enough particles carried in the fluid as they move through the measurement volume. It is collected by a receiving lens and focused on a photo detector producing a signal at the Doppler frequency  $f_D$ .

The velocity is calculated from the Doppler frequency and fringe distance:

$$U = d_f \cdot f_D = \frac{\lambda}{2 \sin(\theta/2)} \phi_D \quad (3.33)$$

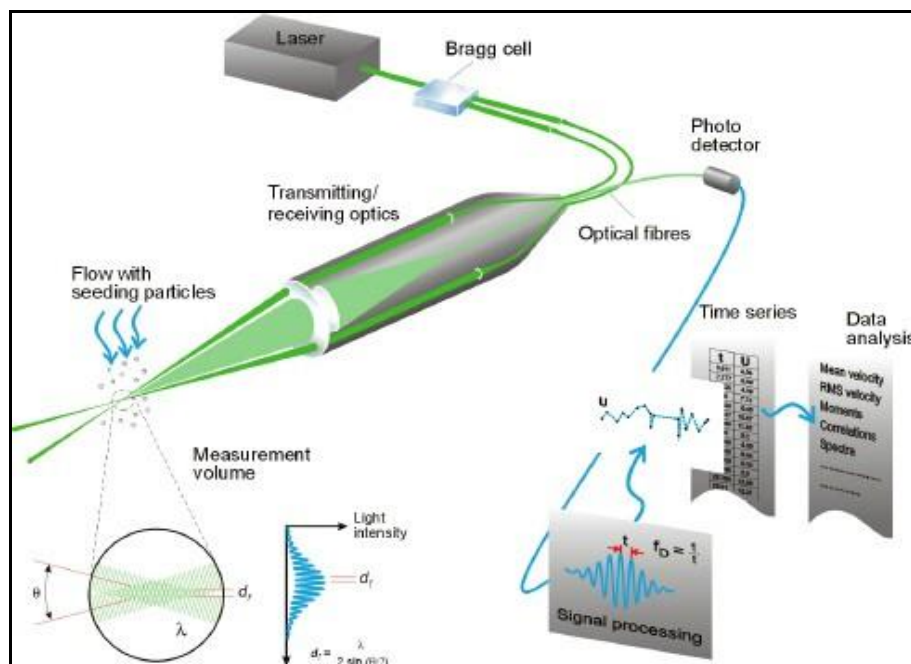


Figure 3.2: LDA technique (Official website from Data dynamic)

In the experiment silicon oil is used to mimic the slag layer, water to mimic steel and air is pumped through the SEN to mimic argon gas. Data for horizontal velocity and its distribution are collected for 7 different points using different water and gas flow rates and for 2cm of oil layer thickness or with 2cm of air. The SEN immersion depth which is the distance between the water level and the highest point of the nozzle ports has been set at 68mm in all measurements. Horizontal velocity and its distribution in time is monitored in seven points as shown in Figure 3.3 along the middle plane of the mould acquired by LDA during a ten minute period.

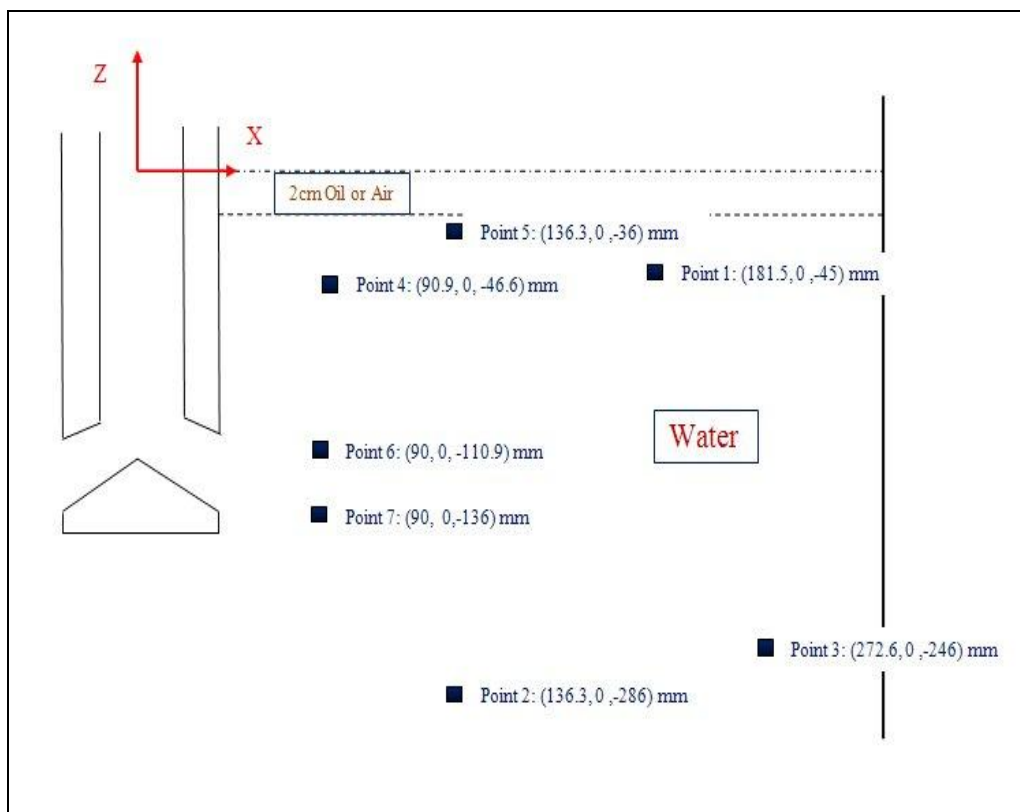


Figure 3.3: Experimental measurement arrangement

## *Chapter IV*

### **4 Description of Numerical Simulations**

#### **4.1 Steady state**

Initially the thesis deals with the implementation of heat transfer and the solidification across a continuous steel casting mould. For this purpose, a 3-D geometry of the mould region has been built, based on water geometry parameters (provided by AMR). A mesh was then constructed making use of the HARPOON [15] mesh generator tool and satisfying the suitability of PHYSICA in terms of the density and orthogonality of the mesh. The continuity, flow, heat transfer plus solidification and turbulence equations are then solved with appropriate boundary conditions. Some of the boundary conditions used were taken from industrial data used in previous research carried out by the University of Greenwich [5, 89]. This preliminary work was important in order to get an overall understanding of the problem and to test the suitability of the HARPOON mesh generator tool. The requirement is for a reasonably orthogonal hexahedral mesh, especially in the critical junction between the SEN outlets – which have an oval cross-section and have a downwards inclination- and the mesh in the rest of the mould which is Cartesian. Since the flow in the mould is determined by the jet exiting the SEN, error in this region would undermine the simulation.

##### **4.1.1 Mesh and boundary conditions**

The geometry required to generate the mesh was constructed using the Rhino [143] surface CAD software with dimensional parameters as presented in table 4.1. The geometry was then exported as an STL format so as to be compatible as import file for HARPOON.

	<b>WATER MODEL CONFIGURATION</b>
<b>Mould width</b>	727 mm
<b>Mould thickness</b>	100 mm
<b>Height</b>	1500 mm
<b>Nozzle design</b>	Roof type bottom nozzle
<b>Immersion depth (distance between mould surface and top of the nozzle port)</b>	68 mm
<b>Nozzle port diameter</b>	36 mm
<b>External diameter of the SEN</b>	63 mm
<b>Internal diameter of the SEN</b>	36 mm
<b>Height of the SEN bottom</b>	13 mm
<b>Nozzle port angle</b>	20°

Table 4.1: Water model geometry and dimensions

In order to have a functional mesh in PHYSICA a crucial prerequisite is the degree of orthogonality. For this mesh, the maximum resulting non-orthogonality angle is 61.5 degrees with refinement zones arranged in the critical area surrounding the nozzle, at the narrow and wide faces with 59896 elements as presented in Figure 4.1.

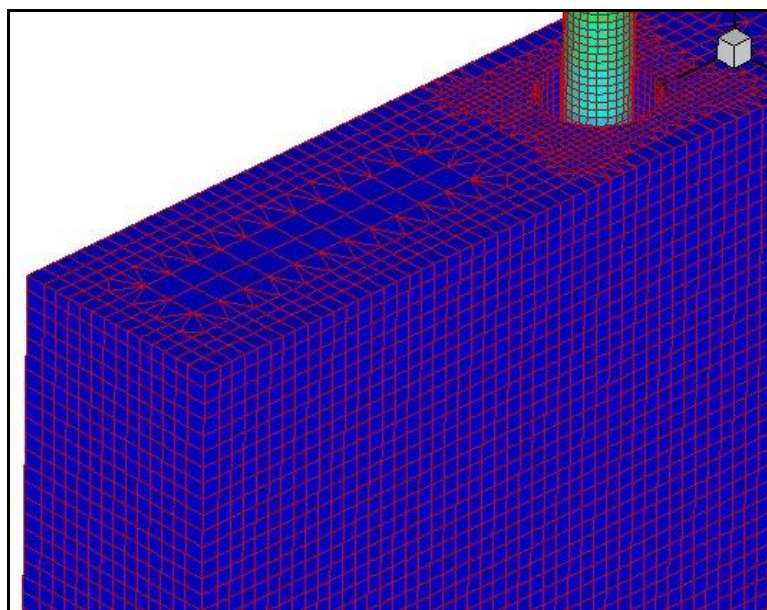


Figure 4.1: Hexahedral mesh created by HARPOON.

The wide and narrow faces of the mould are assumed to be planar walls with no-slip velocity conditions. The vertical velocity component is set at the inlet at the top of the pipe to the value corresponding to the casting speed, and the pressure at the outlet is fixed to zero. Furthermore, the initial values of the velocity are set to zero, and since there is no free surface calculation in this test, gravity is neglected. Molten steel enters the domain at a fixed temperature (1600°C) at a desired casting speed, calculated by the formula below:

$$\begin{aligned} \dot{m}_{inlet} &= \dot{m}_{outlet} \\ V_{inlet} &= \frac{\rho_{steel} V_c A_{inlet}}{\rho_{steel} A_{outlet}} \end{aligned} \quad (4.1)$$

The molten steel is cooled due to the presence of the water-cooled copper mould (using a fixed heat flux condition), and cooling water jets below the mould. The turbulent kinetic energy and dissipation rate at the inlet are estimated by the following empirical expression [22]

$$k = 0.01 v_{inlet}^2 \quad \varepsilon = \frac{2\kappa^{1.5}}{D_{SEN}} \quad (4.2)$$

The ambient temperature is set to 22°C. A fixed heat flux (131Wm<sup>-2</sup>) is extracted in the copper mould. The two water cooled spray regions are calculated by using the heat transfer coefficients (-980Wm<sup>-2</sup>K<sup>-1</sup> and -841Wm<sup>-2</sup>K<sup>-1</sup>).

### 4.1.2 Fluid flow

The flow patterns indicate two recirculation zones which are well known as “the double roll” [75]. The metal created flow is characterized by two vortices for each jet of the bifurcated nozzle. The upper recirculation flow is transported along the narrow faces upwards and along the top mould region. In addition, this flow may move towards the upper edge of the nozzle. The other large vortex moves downwards along the narrow faces and then upwards in the mould centre. The above is depicted using streamlines in Figure 4.2, clearly showing the two rotating loops and the impingement point of the port jet to the narrow face. Control of these loops is important in the CC operation for the distribution of heat within the cast and in the solidification process. Furthermore, control of these loops determines the transport of

inclusions (impurities, argon, gas, droplets). The pressure is highest at the closed bottom of the SEN pipe due to stagnation, as the inlet stream is diverted towards the two SEN outlets.

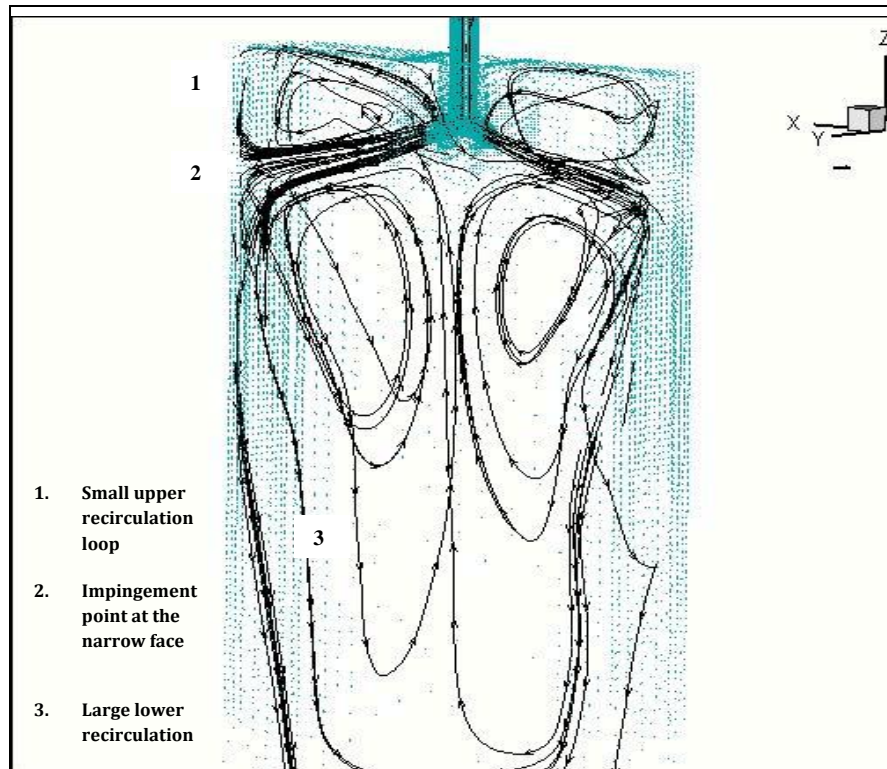


Figure 4.2: Streamlines starting from inside nozzle show the two characteristic recirculation zones.

### 4.1.3 Heat transfer and solidification

Referring to figure 4.3, the temperature in the mould is colder at the corners where it solidifies first. In the vertical direction, the highest temperature is observed, 120mm below the top of the mould. There is a hot region below the SEN and then decreases gradually towards the exit. Horizontally, the temperature decreases gradually from the symmetry centre to the corner. More specifically, the temperature in the corners between the top and narrow walls is the lowest. Thermal distribution is reduced from the middle to the narrow faces. The same observations are expected in the vertical direction, since temperature decreases gradually from the top of the mould to the bottom.

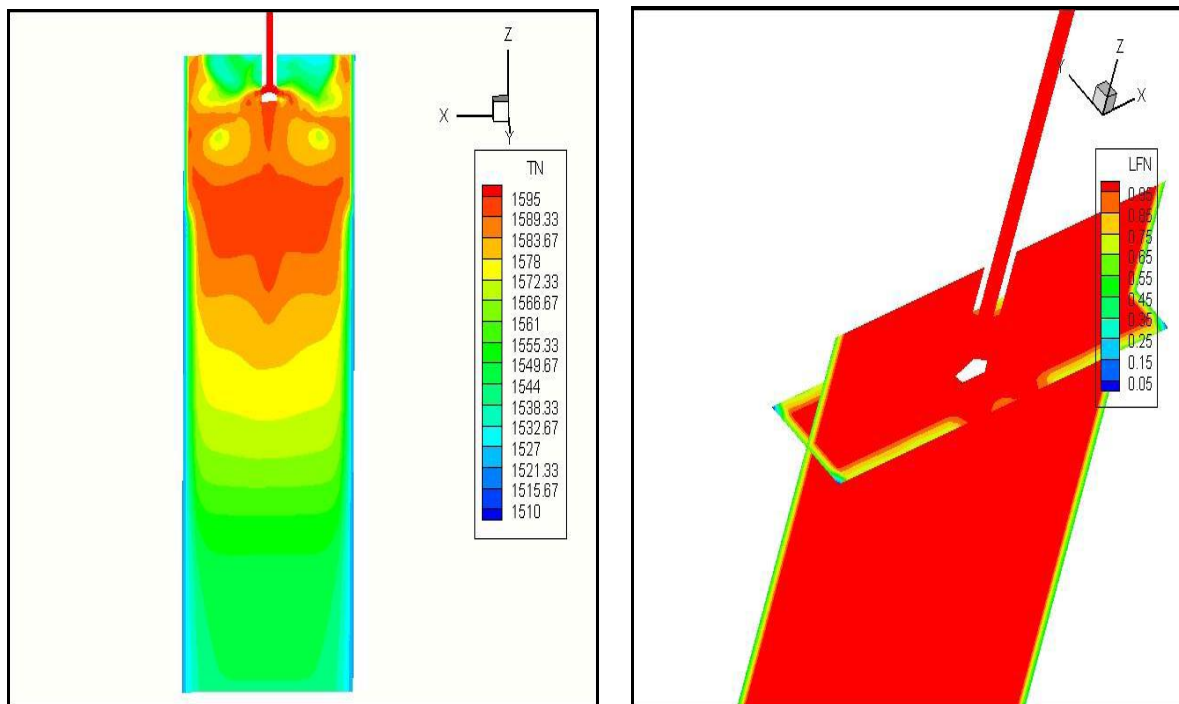


Figure 4.3: Mean temperature field in the x-z plane in the centre of the mould

The results for solidification (Figure 4.3) are illustrated with a contour of liquid fraction (LFN) showing the solid shell being formed at the wide and narrow walls (blue contours). Nevertheless, the temperature at the wide faces is high at 120mm below the top of the mould due to the high velocity in this area. Beyond the mould region, the shell thickness increases with distance as expected [107].

Since solidification is difficult to converge, an under relaxation factor of 0.1 is applied to the solidification solver and false time step of 1s is applied to temperature to provide a light relaxation to the temperature solver. A false timestep of 0.6s is applied to the momentum equation exhibiting the best convergence behaviour. The afore-mentioned results are achieved with a steady-state runs of 10000 iterations with 2 hours real computation time in a single machine of two processors. However this mesh was not suitable for capturing the free surface movement or the boundary layers lining the mould. Therefore reconstruction is needed in the top surface region and the SEN outlet/mould cavity interface. This issue seems to be a time consuming due to the size of the geometry and the complex design of the SEN with approximate time for the reconstruction takes more than two months.

## 4.2 Transient simulations

Despite the encouraging results with the HARPOON mesh, it was not considered suitable for capturing free surface behavior due to the high non-orthogonality of some cells in the SEN. In addition, there is an undesirable sudden jump in the mesh size from the nozzle to the mould region where calculated flow is most sensitive to the mesh. Instead, the unstructured finite-volume hexahedral mesh supplied by AMR (and created using the Gambit software) was used in order to reduce set up time, considering the amount of time required for the reconstruction of the HARPOON mesh.

Returning to the water model the Gambit mesh (following improvements described in the next section) was used to model the transient hydrodynamic aspect of the oil layer behaviour coupled with gas bubbles. This chapter includes a brief discussion of problems encountered and solution in order to overcome them during the numerical operation.

### 4.2.1 Mesh and boundary conditions

A Gambit-to-Physica filter was used to enable this mesh to be read by PHYSICA and its proprietary pre/post processor. Additionally, a new volume patch was created in the upper water region (volume area of the immersion depth) which does not include the high speed region of the submerged jet. This new region together with the oil layer can form an “active group” where the Donor-Acceptor method can be used. Therefore, it is not needed to make the time step excessively small as high speed region is not included.

The Gambit mesh showed good convergence behaviour for both transient and steady state simulations, with highest non orthogonality at 58.8 degrees and a total of 229664 elements. Despite a well-converged solution, comparisons of mean velocity values between experimental and numerical results (discussed in the next chapter) proved to be unsatisfactory. The above forced us to re-examine this mesh which in turn, enabled us to pinpoint a serious flaw. A close view at the critical area of the exit ports shows an asymmetry (Figure 4.4). Even worse, the front part of the nozzle is very coarsely meshed, and quite unsuitable to capture the strong gradients that occur in this location. Another problem that occurs with the same mesh is the extremely poor aspect ratio at the lower boundary of the

domain and narrow faces. This was the suspected cause for transient instability problems with the exit boundary condition (Pressure=0) and possible false oscillation in the time-dependent cases.

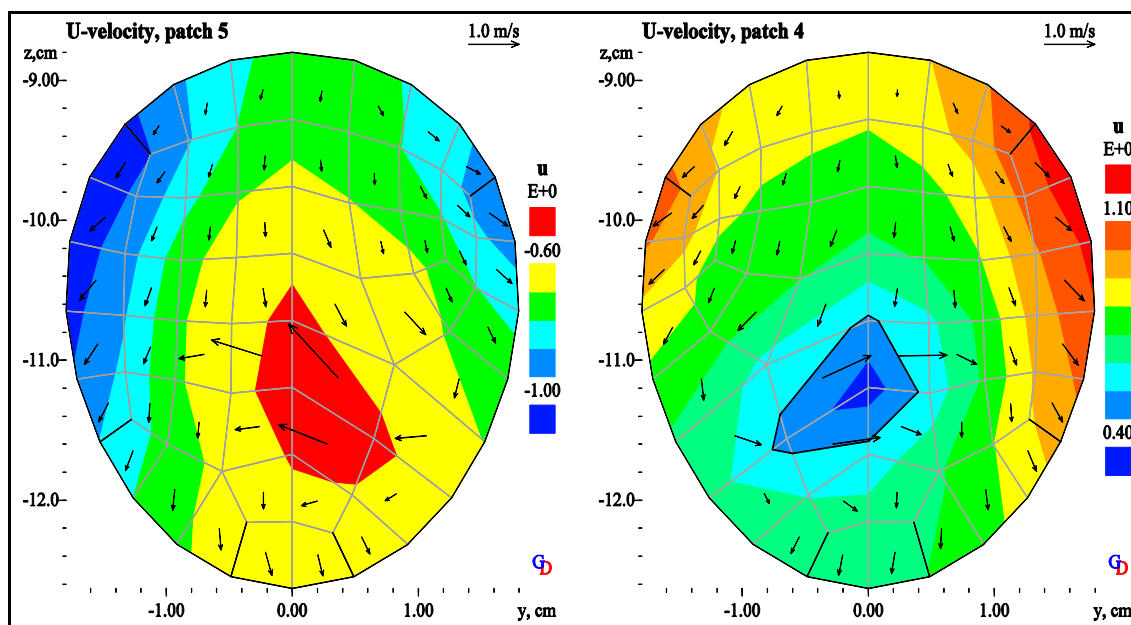


Figure 4.4: Left port and right port are shown to be not symmetrical across the middle plane

In order to correct the asymmetry, the best one-quarter domain of the Gambit mesh was cut and then mirrored in the x direction in order to achieve a half mesh or in both directions (x and y) so as to extract a full one. The corrected mesh with non-orthogonality contour is depicted in Figure 4.5. The above used the same water model dimensions geometry as given in detail in table 4.1.

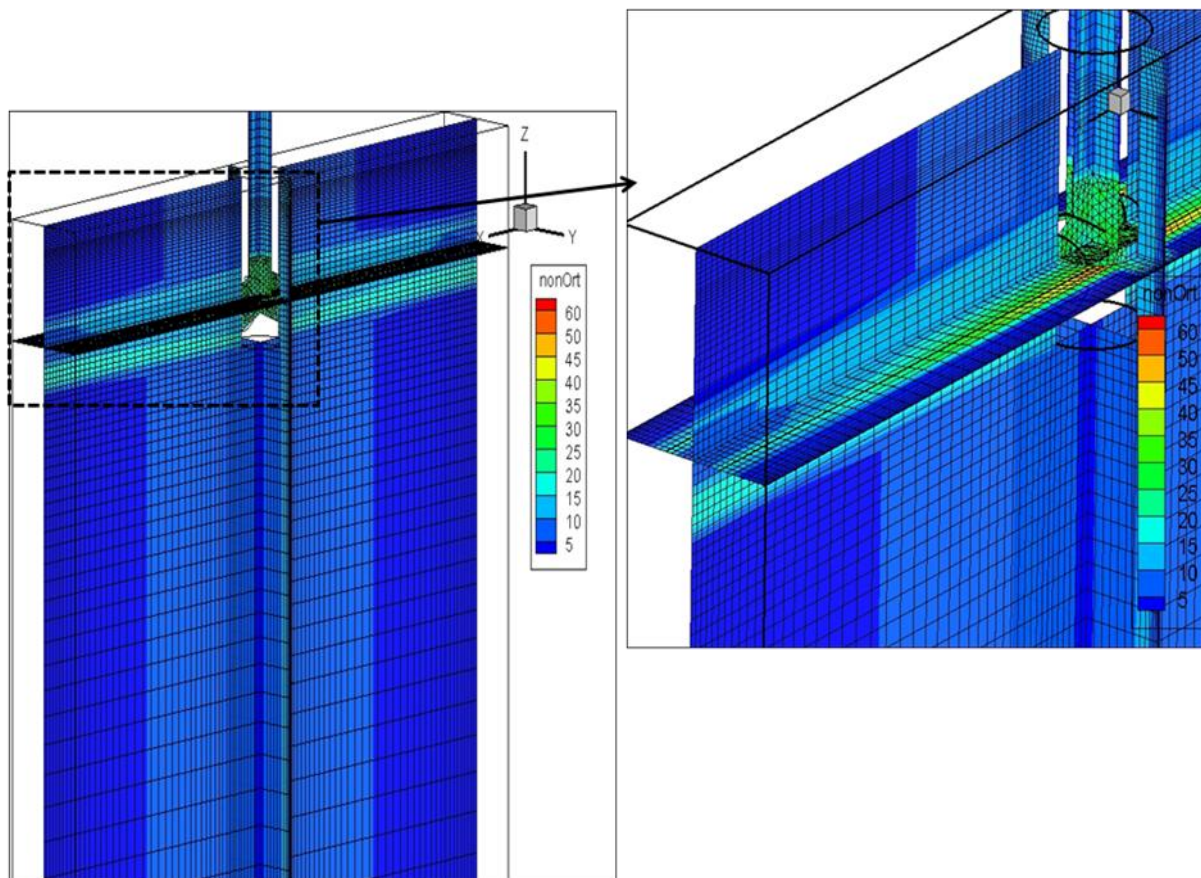


Figure 4.5: Corrected mesh with non-orthogonality contour

The pipe inlet velocity is set to a fixed value to reproduce the experiments (0.5m/s, 0.8m/s, or 1.018m/s) and thus the flow rate remains constant during a simulation as determined by empirical data from Arcelor. Since the water circulates in a closed loop between outlet and inlet using a pump, it is expected that some fluctuations are introduced in the system. These fluctuations were not measured in the experiments and so they were not modelled.

The reference pressure value is set to zero at the outlet of the domain. The narrow and wide faces are assumed to be plane walls. The inlet values for turbulence model,  $k$  and  $\varepsilon$  are calculated as in the equation (4.2). A summary of the boundary conditions and material properties is shown in table 4.2:

Multiphase Model			
Water	$\rho = 1000\text{Kg/m}^3$ $\nu=1.0\text{E-}6 \text{ m}^2/\text{s}$	Oil	$\rho = 860\text{Kg/m}^3$ $\nu=2.282\text{E-}5 \text{ m}^2/\text{s}$
Interfacial Surface Tension	0.035N/m	Air	$\rho=1.2\text{Kg/m}^3$ $\nu=1.48\text{E-}5\text{m}^2/\text{s}$
False Timestep Parameters			
Pressure	No	Momentum	0.1s
Turbulence Kinetic	No	Dissipation $\varepsilon$	No
Boundary Conditions			
Pressure Outlet	0Pa	Inlet Velocity	0.5m/s,0.8m/s, 1.018m/s
Inlet turbulent kinetic energy	$0.01v_{inlet}^2$	Thickness Of Oil	2cm
Inlet Dissipation of $k$	$\frac{2\kappa^{1.5}}{D_{SEN}}$	Outlet Kinetic energy	$1\text{E-}4\text{m}^2/\text{s}^2$
Outlet Dissipation	$1\text{E-}4\text{m}^2/\text{s}^2$		

Table 4.2: Physica properties for the case with water and 2cm Oil.

### 4.2.2 Turbulence model modification

The turbulence model has an important role to play in these simulations, since it is directly associated with the dynamic behaviour of steel meniscus. Previous work at the University of Greenwich [5, 47, 52] have successfully adapted standard k- $\varepsilon$  models in a transient simulation. The k- $\varepsilon$  model has proved to be the most popular, mainly because it does not require a near-wall correction term [108]. However, if the time step in a CFD simulation is not in the important range of flow induces-eddies, this will lead to an overestimation of the turbulence energy and consequently the excessive diffusion. This will suppress the energy leading to the elimination of the surface oscillations causing artificial damping. In an attempt to resolve the above problem, a k- $\varepsilon$  ‘filter’ in the Kolmogotov-Prandtl equation was introduced taken from the work of Johansen [10] to reduce the effective viscosity. The filter size is described by the following equation:

$$f = \text{Min}\left(1, \frac{\Delta \cdot \varepsilon}{\kappa^{3/2}}\right) \quad (4.3)$$

where  $\Delta$  is the filter size. This depends on the characteristic length  $D$  which in our case is related to the SEN port diameter. A suggested size for axisymmetric jet is usually taken as  $0.075D$ . This was determined by Johansen [10] during a comparison of the flow (vortex street) behind a square obstacle with experimental measurements.

A brief investigation of the  $k$ - $\varepsilon$  turbulence filter size (using the case with 2cm oil thickness without gas and an inlet velocity of 1.018m/s) shows that the filter function affects the flow, as observed by the two recirculation loops and the periodical oscillation. Figure 4.6 shows the velocity magnitude in the case where filtered turbulence models are used (left). Close observation of this figure highlights the spread of the jet coming out of the nozzle port. The filter removes turbulent energy from the diffusion term of the momentum equation: the mean value of the velocity is then reduced as a consequence, but the jet fluctuation increase. In the case of the standard  $k$ - $\varepsilon$  model (Figure 4.6 - right), the mean velocity magnitude is increased, leading to a stronger top recirculation loop and the oil/water interface becomes more distorted. In contrast, the filter leads to a weaker top loop but to higher oscillation amplitudes that do not decay in time (Figure 4.7).

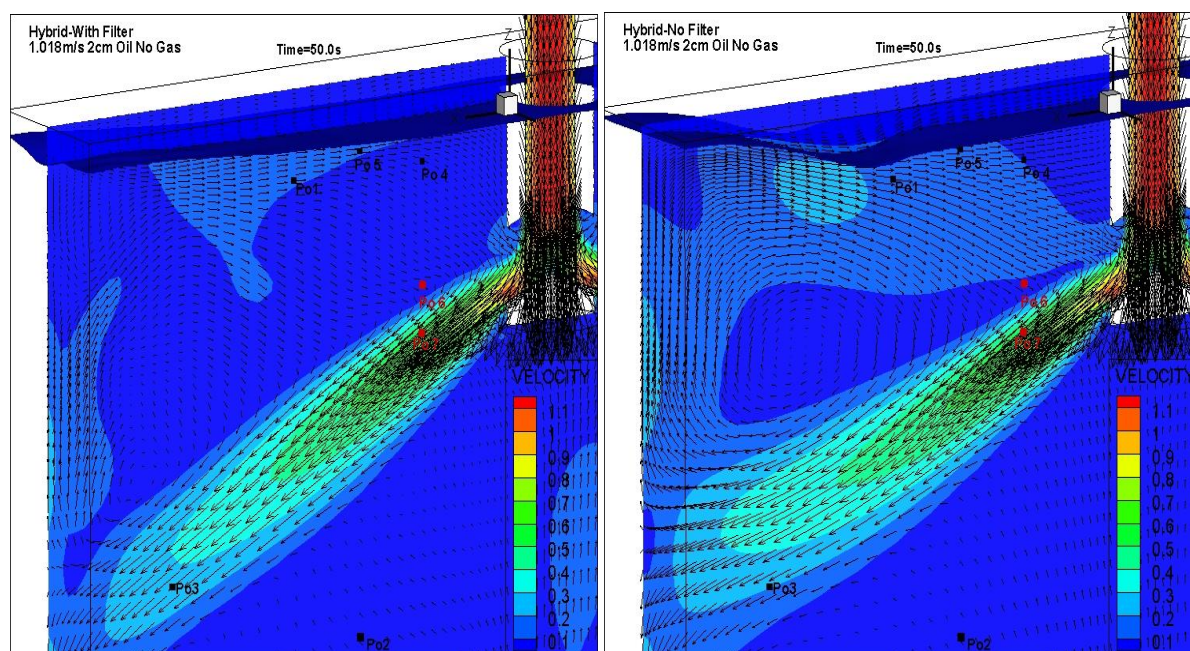


Figure 4.6: Velocity magnitude contours and velocity vectors (a) with filter (left) and (b) without filter (right).

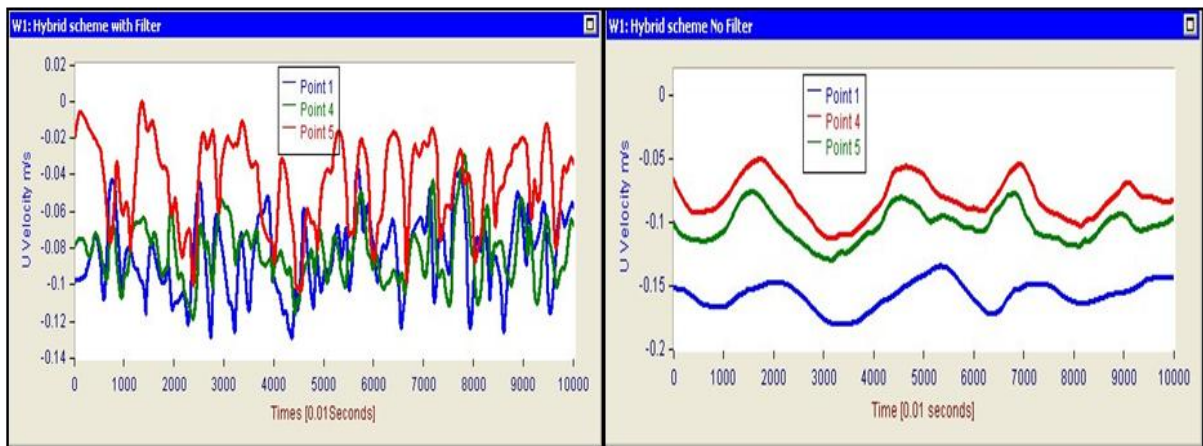


Figure 4.7: Monitor distribution of horizontal velocity at Points 1,4 and 5 (simulation with inlet velocity 1.018m/s). The oscillations persist at relatively constant amplitude throughout the simulation when the filter is used.

Using the initial flawed mesh (Chapter 4.2.1), the sensitivity of the filter was examined by comparing three different filter sizes: 0.05D, 0.075D, 0.15D against LDA measurements, assuming that the characteristic length D is 0.036m, that is the internal nozzle port diameter. Figure 4.8 is the comparison of mean values and fluctuations of horizontal velocity between the three filters and the experiment, exhibits that the application of the k-ε filter led to a big disagreement between computation and experiment results due to the filter. The largest discrepancy is between standard deviation (a measure of turbulent fluctuations) at points 6 and 7, which are closest to the jet.

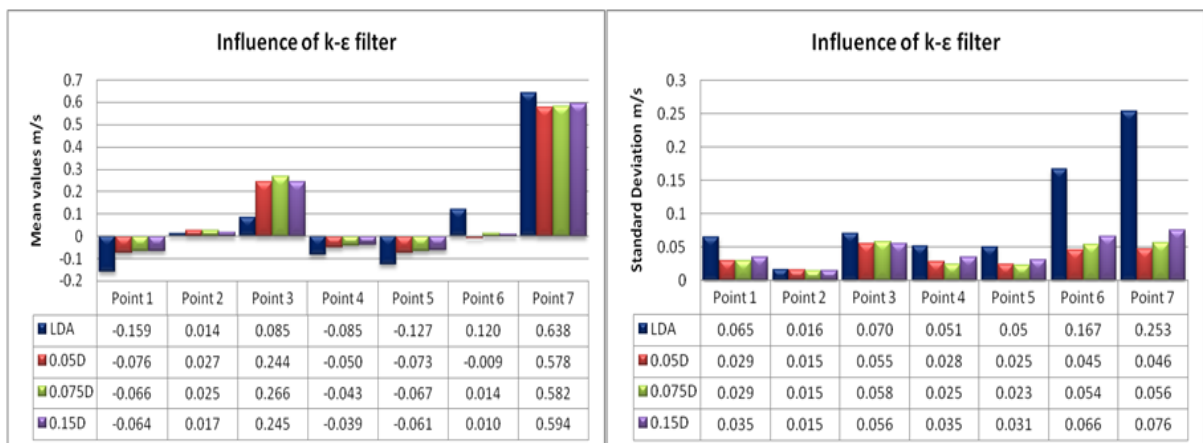


Figure 4.8: Comparing mean values and Standard Deviation of horizontal velocity for the seven measurements points between various k-ε filter lengths using original flawed mesh.

The filtered turbulence model increases the mean value of horizontal velocity for the points near the oil layer (points 1, 4 and 5). This probably happens because the filter reduces the effective viscosity that has already been accounted for in the NS equations, hence jet

momentum (plus oscillation amplitude) increases. The opposite observation holds true for standard deviation. In addition, the length of the filter for the range used is not a significant factor in the influence of the mean values and standard deviation of horizontal velocity.

Figure 4.9 (right part) shows that the standard deviation decreases when we turn on the  $k$ - $\varepsilon$  filter. However, the standard deviation measured by LDA is higher, except for points which are far from the oil layer (point 2 and 3), which means that turbulence levels are underestimated by the model. For standard deviation it is assumed that the low frequency velocity and turbulence are independent, and have isotropic turbulence, where:

$$k = \frac{3}{2} u'(t)^2 \text{ and standard deviation is given by } \sigma_T = \sqrt{\text{var } u(t) + \frac{2}{3} k} \quad (4.4)$$

where  $k$  is determined by averaging over the calculation duration and  $u(t)$  is the instantaneous velocity calculated by PHYSICA and  $\text{var}$  denotes variance.

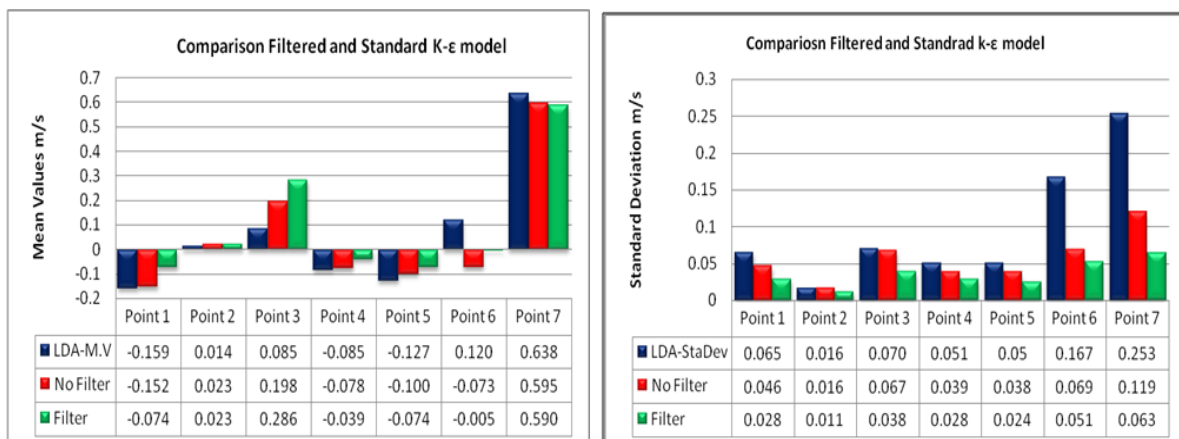


Figure 4.9: Comparing mean values and Standard Deviation between the case with  $k$ - $\varepsilon$  filter and without.

Despite the improved agreement obtained with the utilization of the standard  $k$ - $\varepsilon$  turbulence model, there is still disagreement between LDA and CFD attributed to the flawed mesh. This was confirmed by comparing between the original mesh (see Chapter 4.2.1) with a new improved mesh. It is clear that generally more accurate results were successfully obtained with the optimized mesh. Figure 4.10 depicts the mean values for the original and improved mesh without the activation of the  $k$ - $\varepsilon$  filter, using Hybrid scheme.

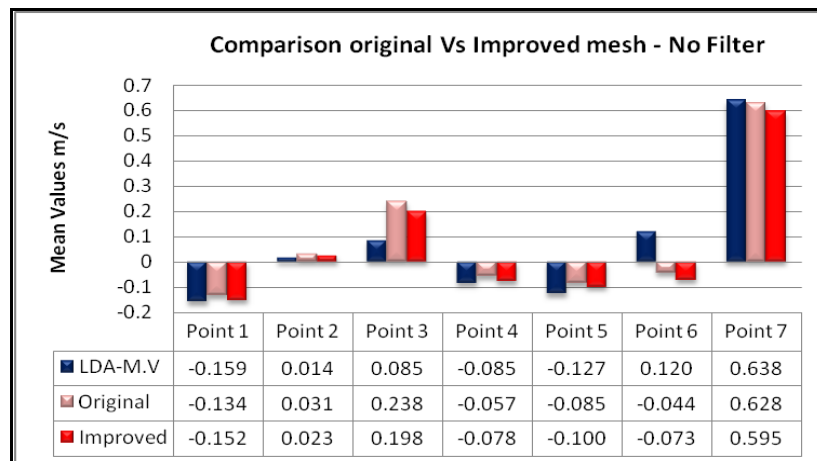


Figure 4.10: Comparing mean values obtained with the original mesh and the improved mesh using the Hybrid scheme without a  $k-\epsilon$  filter.

In conclusion, modification of the  $k-\epsilon$  turbulence model results in a better amplitude prediction of the horizontal velocity distribution in the oil/water interface but it also affects the mean value and the standard deviation. On the other hand the standard turbulence model gives a good quantitative agreement for both velocity mean value and its standard deviation, but visual observation and horizontal velocity distribution plots show the almost complete suppression of the oil surface oscillation.

Two approaches were analysed in order to solve the difficulties that have been raised above:

1. Vertical velocity fluctuation damping was introduced at the interface between water and oil when the simulation was performed utilizing the default Hybrid scheme. This is done by suppressing the turbulence in the oil layer so as to remove the high gradient of density (buoyancy stratification of turbulence).
2. The effect of higher-order differencing schemes (in combination with the standard  $k-\epsilon$  model) was studied since numerical diffusion error was suspected, affecting the jet coming out of the nozzle port at close to 45 degrees to the mesh direction. This numerical scheme was used to solve  $u(x)$  and  $w(x)$  momentum components and turbulence model, with a smaller false timestep ( $10^{-2}$ s) than that use in simulation with Hybrid (0.1s).

Validation between the two solution approaches and LDA results is dealt with in Chapter 5.

### 4.2.2.1 First order Hybrid scheme

The choice of numerical scheme was found to influence the results of the simulations. For this reason the two alternative schemes used are discussed here.

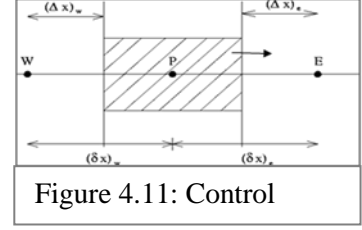


Figure 4.11: Control

The Hybrid scheme, developed by Spalding [110], is a combination of the central Differencing scheme and the Upwind Scheme which was first recommended by Courant, Isaacson and Rees [111]. The integration of the one dimensional steady-state equation with a convection and diffusion term becomes

$$(\rho u \phi)_e - (\rho u \phi)_w = (\Gamma(\phi_E - \phi_P) / \delta x_e) - (\Gamma(\phi_P - \phi_W) / \delta x_w) \quad (4.5)$$

where  $(\rho u \phi)_e$  is the property leaving the east face and  $(\rho u \phi)_w$  is the property entering the west face as depicted in Figure 4.11.

A simple average for properties  $\phi$  - properties is used for Central Differencing scheme,

$$\begin{aligned} \phi_e &= \frac{1}{2}(\phi_E + \phi_P) \\ \phi_w &= \frac{1}{2}(\phi_P + \phi_W) \end{aligned} \quad (4.6)$$

Equation 4.6 can be arranged in terms of the cell-centred values  $a_P \phi_P = A_E \phi_E + A_W \phi_W$ , if we use the convection and diffusion fluxes

$$F = \rho u \quad D = \frac{\Gamma}{\delta x} \quad (4.7)$$

where the influence coefficients are then defined as

$$\begin{aligned}
a_E &= D_e - \frac{F_e}{2} \\
a_W &= D_w + \frac{F_w}{2} \\
a_P &= D_e + \frac{F_e}{2} + D_w - \frac{F_w}{2} \\
&= a_E + a_W + (F_e - F_w)
\end{aligned} \tag{4.8}$$

The Central Scheme produces unrealistic results since with the change in flow direction, some of the coefficients may become negative. This can lead to the solution of the discretized equation becoming unbounded [112].

The Upwind scheme uses the value of  $\phi$  of the node upwind of the face, for the value at the face. The coefficients are then always positive and as a result lead to a bounded solution, given by,

$$\begin{aligned}
a_E &= D_e + \max(F_e, 0) \\
a_W &= D_w + \max(F_w, 0) \\
a_P &= D_e + \max(F_e, 0) + D_w + \max(-F_w, 0) \\
&= a_E + a_W + (F_e - F_w)
\end{aligned} \tag{4.9}$$

The disadvantage of the upwind scheme is that artificial diffusion is introduced into the solution leading to numerical smearing [97].

The Hybrid scheme uses a formula based on the local Peclet number to evaluate the flux through each control volume face, where the Peclet number is defined by  $Pe = \frac{F}{D} = \frac{\rho u}{\Gamma / \delta x}$ .

This scheme is reduced to the Central Differencing scheme for Peclet numbers in the range  $-2 \leq Pe \leq 2$ . Outside this range, the Upwind Scheme is used, in which the diffusion is set to zero. Then the influence coefficients are given by

$$\begin{aligned}
a_E &= \max(-F_e, D_e - \frac{F_e}{2}, 0) \rightarrow \text{for } -2 < Pe < 2 \\
a_W &= D_w + \max(F_w, D_w + \frac{F_w}{2}, 0) \rightarrow \text{for } Pe \geq 2 \\
a_P &= a_E + a_W + (F_e - F_w) \rightarrow \text{for } Pe \leq -2
\end{aligned} \tag{4.10}$$

### 4.2.2.2 Second order SMART scheme

The SMART scheme [11] is used to solve  $u$  and  $w$  momentum components and the turbulence model equations so as to minimise the error due numerical diffusion. In order to satisfy relaxation and convergence criteria (stabilised the solution, reduce the scaled residuals for all variables below a specified tolerance) a smaller false timestep of  $10^{-2}$ s is used in the momentum and  $k$ - $\epsilon$  equations in comparison to the false timestep used in the simulation with Hybrid. The tighter relaxation values mean more iteration in the solution and so lead to excessive computational time. The SMART scheme is formulated to satisfy the convective boundedness criterion [98], which states that in the absence of sources, the internal nodal values of the property  $\phi$  should be bounded by its boundary values. Additionally, all coefficients of the discretised equations should have the same sign [113]. The SMART scheme uses a third element to estimate the value of the dependent variable  $\phi$ , on a face. The face value of  $\phi$  is calculated using the equation

$$f_f = f_C + 0.5Y(r)(f_C - f_U) \quad (4.11)$$

where

$$r = \frac{\phi_D - \phi_C}{\phi_C - \phi_U} \quad (4.12)$$

Where subscripts  $C$ ,  $D$  and  $U$  represent the elements on the upwind, downwind and "upwind upwind" side of the face. The "upwind upwind" element is chosen based on the geometry of the mesh rather than on the flow pattern.

For the SMART scheme

$$\Psi(r) = \max[0.0, \min(2r, 0.75r + 0.25, 4)] \quad (4.13)$$

This class of schemes leads to a source contribution for both elements associated with the face equal to:

$$-f_a 0.5\Psi(r)(\phi_C - \phi_U) \quad (4.14)$$

### 4.2.3 Free Surface simulation

A 3-D model was developed to describe turbulent fluid flow coupled with the time dependent motion of liquid slag. Initial calculations were performed using either the Volume of Fluid method (Donor Acceptor) or the improved Counter Diffusion Method (CDM) interface tracking scheme. Preliminary tests of CDM were encouraging, but longer simulations of the water model showed a gradual depletion of the oil layer (Figure 4.12) since minute quantities of oil “leak” numerically towards the outlet. To combat this, we implemented a revised corrective mechanism in order to restore the upper fluid by a simple mass source. The new CDM used the normal vectors to the interface to apply a counter-diffusion correction. This is an addition to the previous correction of a fictional velocity term in the gravity vector direction, with which any droplets would move down towards the interface and any bubbles would rise up towards the interface. The afore-mentioned improvements ensure a sharper interface when there is strong flow along interface.

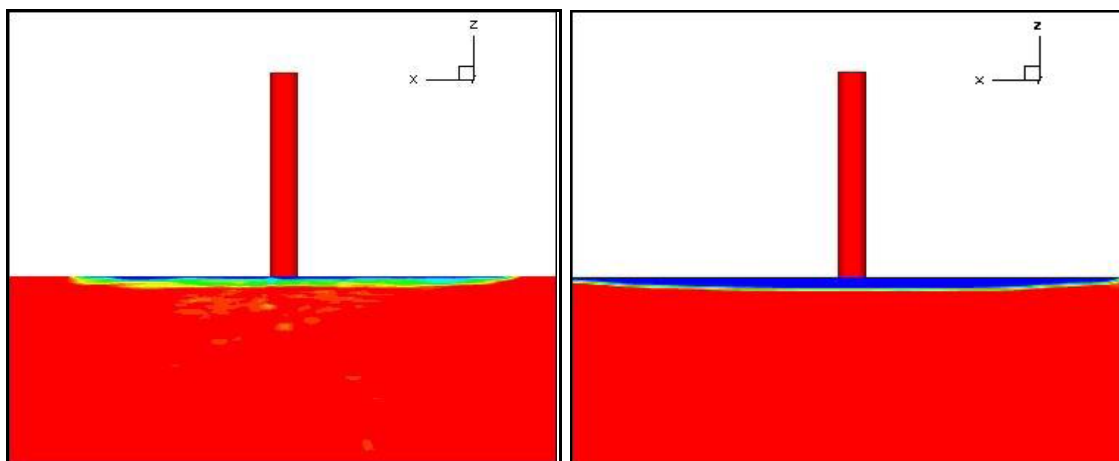


Figure 4.12: Free surface with CDM (left) and Donor Acceptor (right) using 0.01s time-step

The thickness of the oil is important in the deformation of the interface. The oil layer is pushed upwards by the top loop of the SEN jet. In our case of a 2cm oil thickness, the upper loop exposes the water free surface to air as shown in Figure 4.13. Transient fluctuation causes time-variations in the interface level that may lead to surface defects in a real caster, such as entrapped mould powder or oxidation of the exposed surface.

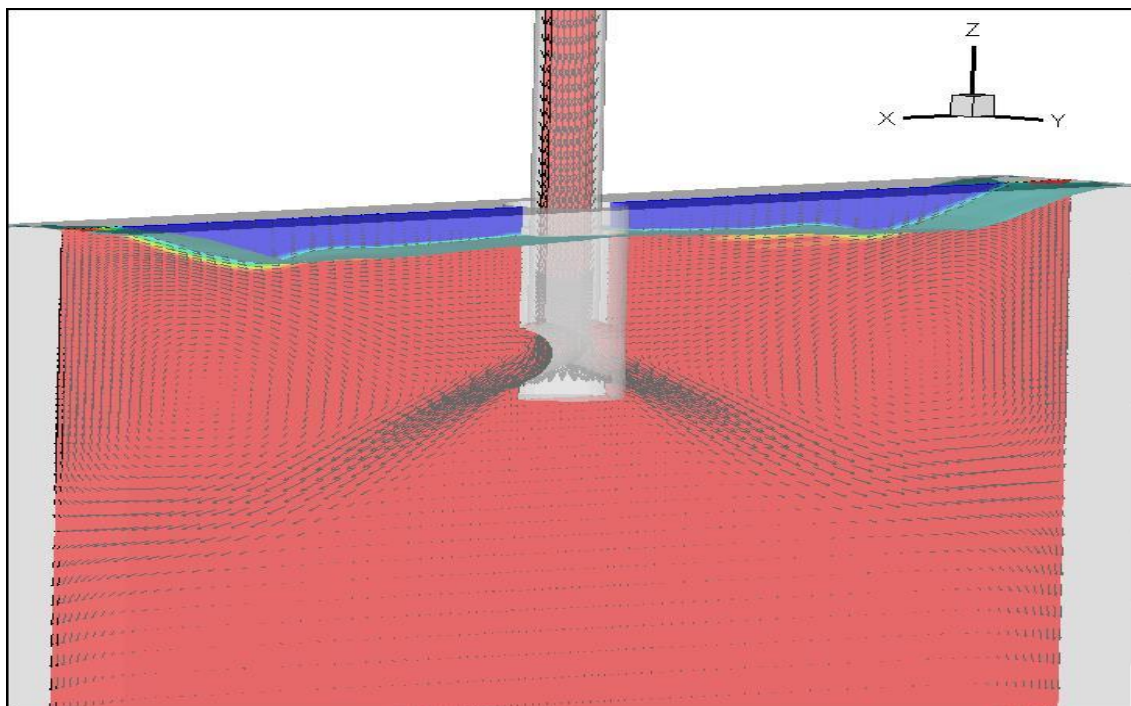


Figure 4.13: Oil/water inter-surface and contour of the surface tracking variable  $\phi$  'fs-phi' at the symmetry plane,  $y=0$  showing velocity vectors using the SMART scheme.

#### 4.2.4 Particle tracking simulation

One of the main aims of this research is to determine the influence of gas bubbles, which disturb the interface as they flow through the oil layer to the surface. Bubble behaviour in multi-phase flow is of paramount importance in many engineering applications. Two approaches were used in previous investigations to model the bubbles' behaviour: The Eulerian [114, 115] and Lagrangian [55, 26, 116] approaches. The Eulerian approach uses a fixed frame of reference and a continuum formulation of the conservation equation for both phases. The interaction between phases is then handled through interface sources in the transport equations. In the Lagrangian approach, the equations of motion and transport of representative samples of discrete particles are solved explicitly and the particles are tracked through the flow field. To couple the discrete particle phase with the liquid phase, sources again are exchanged to represent momentum, mass, energy and turbulent interactions.

Care needs to be taken when specifying the inlet boundary conditions for the SEN, when gas bubbles are introduced. When a fixed velocity is specified at the inlet, most of the bubbles, which are injected in a plane just downstream, tend to move upwards to the pipe inlet due to the buoyancy. Observations of the critical area near the SEN outlet revealed that the inlet

momentum for water eventually changes that for gas, leading to gradually weakening jets. The problem was solved using a mass flow rate condition at the inlet. Sources can then be linearised for stability using a convectional **Coefficient-Value** format as follows:

$$S = C_o (V_{al} - \Phi) \quad (4.15)$$

The source for this boundary type is then equal to:

$$C_o = A\dot{m} \quad (4.16)$$

$$V_{al} = u \quad (4.17)$$

where  $\dot{m}$  is the mass flow rate,  $A$  is the inlet face area and  $u$  is the face velocity.

It was observed that under the same conditions of Figure 4.13 the oil layer now spreads out to cover the water surface under the action of the gas bubbles (Figure 4.13). To allow the bubbles to escape into the atmosphere, the oil top boundary condition is modified from a default option (which employs symmetry) to an open boundary which in turn, becomes an inlet/outlet for oil, as well as for the bubbles.

The results presented in this section are produced for a 2Nl/min gas flow rate (5.95e-5Kg/s) and a water flow rate of 1018Kg/m<sup>2</sup>s (1.0946Kg/s). Initial calculations were performed using one thousand representative particles, separated into nine size groups with diameters ranging from 1mm to 5mm. The bubbles are injected in the SEN downpipe at a random position in the radial direction, a uniform distribution in the azimuthal direction and a random position along the z-axis within specifies volume. Using the above assumptions we obtained reliable well converged results.

As noted above the oil is spread along the interface and in contrast to the case without bubbles there is some mixing between oil and water (shown as a smearing of the interface where the gas passes through the oil layer). Using a range of bubble diameters shows that large bubbles leave the SEN jet early and rise to the surface while the small bubbles are more likely to reach the narrow end of the mould, as shown by a typical track in Figure 4.14. The same figure also shows an iso-surface of gas volume fraction, which is used to compute the local mixture density. The dense plume of large bubbles is clearly shown flowing towards the

surface near the SEN, whilst a secondary plume containing the smaller bubbles reaches the narrow end whence it flows towards the surface.

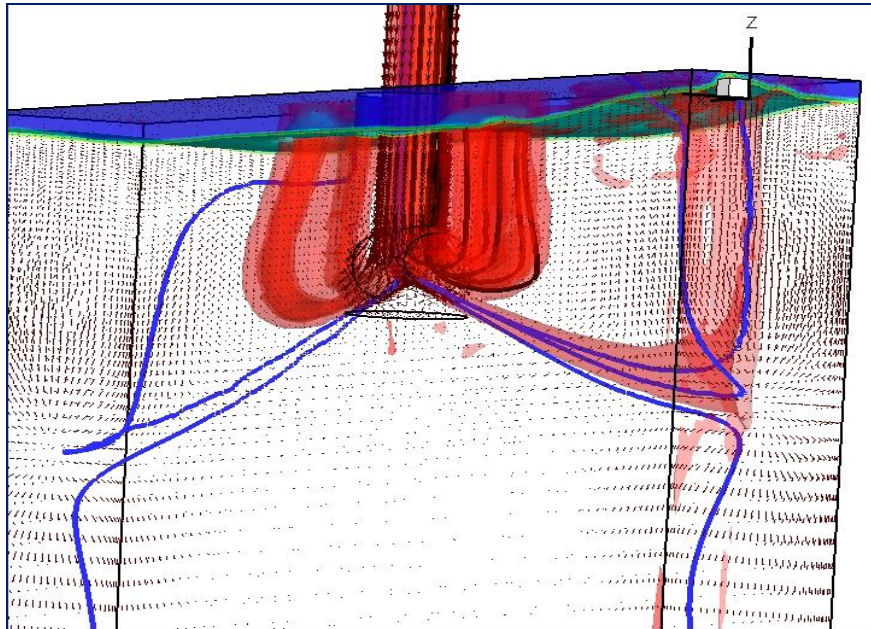


Figure 4.14: Flow pattern in the middle plane of the mould with the interface fs-phi iso-surface, iso-surface of gas volume fraction and typical particle tracks. Large bubble tracks are in black and small bubbles are in blue colour.

The presence of large quantities of gas affects the flow field due to buoyancy, especially near the nozzle (Figure 4.15). This figure also illustrates the velocity vectors coloured with the velocity magnitude, that demonstrate a wider jet exit and an upturned flow near the nozzle due to the presence of gas. In addition the buoyancy forces of the bubbles cause a weakening of the flow in the corner between the top and the narrow wall of the mould. In the case with gas, the stronger flow near the nozzle is observed to affect the oil/water interface deformation. The buoyancy, induced by the change in mixture density, alters the top recirculation which breaks into two counter-rotating vortices as depicted in Figure 4.14. This appears as a bulging of the interface where the gas exits, and may also explain the effect of gas on the measured frequency spectrum that will be introduced in a later chapter. The actual size distribution and mass injected per diameter will affect the results of the simulation, since bubbles affect both the flow field and the frequency spectrum.

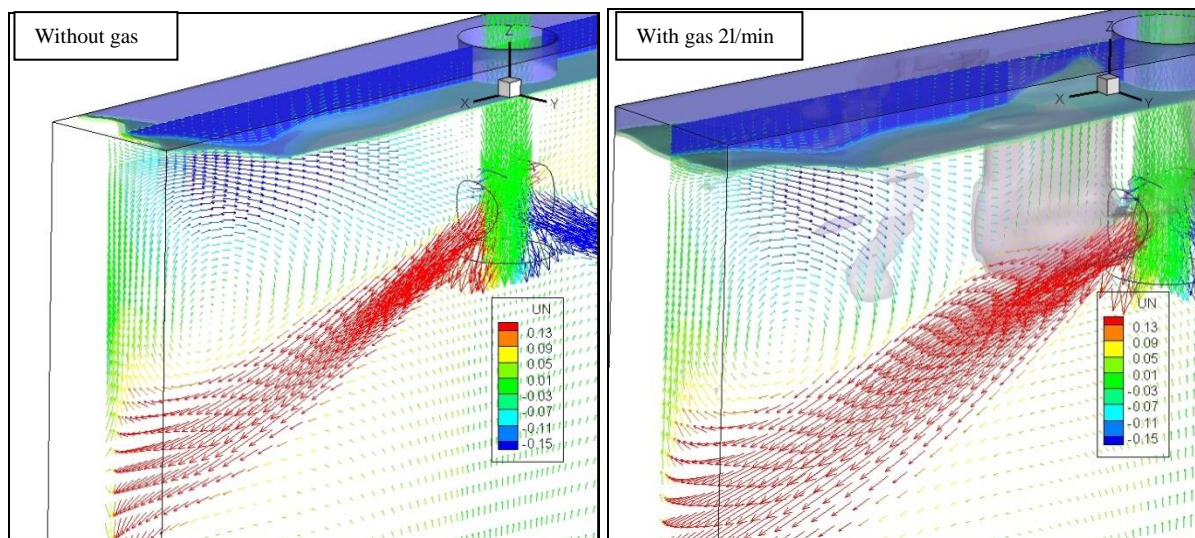


Figure 4.15: Influence of gas in the flow pattern in the case with inlet velocity 1.018m/s and a 2cm Oil layer.

### 4.3 Industrial configuration

Finally, the thesis concerns the development of a model representing an industrial configuration for which a limited experimental data exist for validation. For this configuration it is necessary to implement in addition to fluid flow heat transfer and solidification coupled with the transient behaviour of slag and particle tracking. This case includes a free surface model to allow the steel flux interface to move and the Lagrangian model to capture the influence of argon gas buoyancy. The physical behaviour of the slag layer is important as, its deformation and thickness variation due to the flow of metal, leads to uneven heat transfer across the slag layer. No article investigating this behaviour has been found in the literature review for this thesis.

#### 4.3.1 Mesh and boundary conditions

The mesh was constructed using MB3 [117] which is an extended mesh generation module inbuilt in PHYSICA, with geometric details as shown in Table 4.3 and provided by AMR. The grid was first generated in one-quarter of the mould and was then copied to ensure and avoid the undesired asymmetric flow conditions encountered initially.

The CFD calculation model includes the following characteristics:

1. Transient turbulent fluid flow (Standard k- $\epsilon$  model) and heat transfer in the mould.

2. Full time-dependent simulation tracking the steel/slag interface in real time, under the influence of bubble buoyancy forces.
3. Solidification model for the formation of the solid shell growth using heat transfer boundary conditions that are a function of the vertical position along the mould.
4. Lagrangian tracking of argon particles which are injected with the molten steel in the top of the nozzle and their influence on the flow pattern.
5. Solidified regions are allowed to move relative to the mould at the prescribed casting speed.

	INDUSTRIAL CONFIGURATION
Mould width	1900 mm
Mould thickness	229 mm
Height	1600 mm
Nozzle design	Flat type bottom nozzle
Immersion depth (distance between mould surface and top of the nozzle port)	120mm,160mm,200mm
Nozzle port diameter	Stepwise (Oval section )
External diameter of the SEN	194x122 mm
Internal diameter of the SEN	135x67 mm
Height of the SEN bottom	30 mm
Nozzle port angle	0°

Table 4.3: Industrial model configuration geometry and dimensions

It is important to mention that the initial calculations were performed assuming that the density and thermal conductivity of solid flux are equal to its liquid phase so as to simplify the model. The model was first applied to study the effect of gas flowrate and casting speed on mean flow behaviour. The influence of these two parameters is already seen in real industrial caster measurements. A steady-state calculation was performed for this task assuming a flat steel/slag interface either with gas or without. The calculation includes heat

transfer analysis and solidification in the mould, using temperature dependent properties for steel.

The aforementioned phenomena are then coupled with the heat transfer conduction of powder, taking into account its solid and liquid states. For an accurate prediction of the solid-liquid transformation of phases a suitably fine mesh is required. Therefore, the mesh is refined in the critical top region and near the narrow faces where rapid changes of heat flux and thermal profiles are expected. The mesh density was increased from 69738 to 133610 elements, as depicted at Figure 4.16.

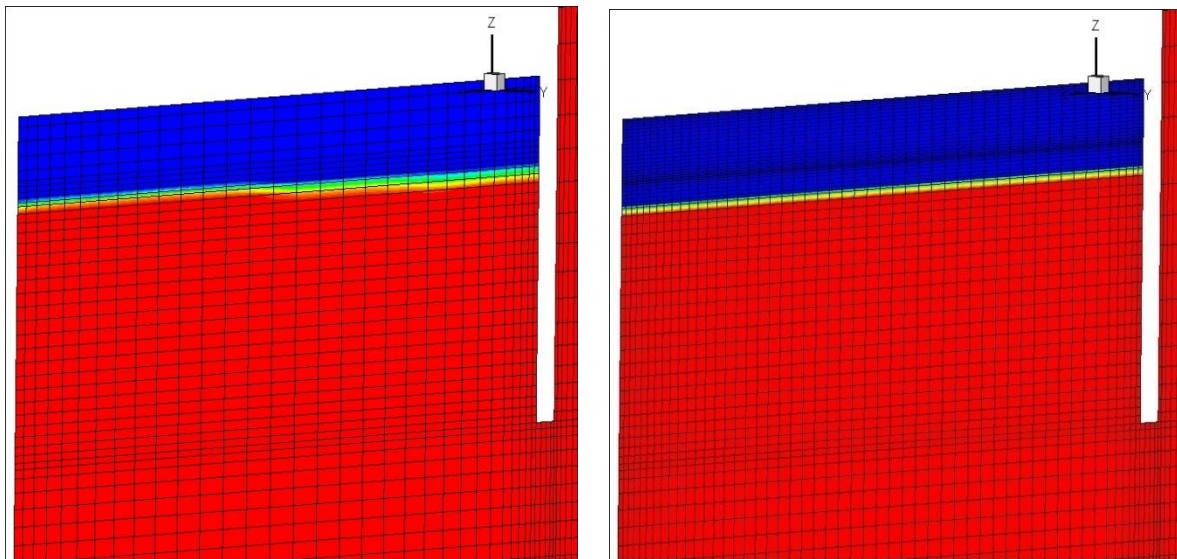


Figure 4.16: Two different meshes used for the investigation of the influence of gas (Left) and finer mesh to capture the phase transformation of the slag layer (Right).

The casting mould and SEN, including 700mm of slab length below the mould exit with the boundary conditions employed in the simulation are represented in Figure 4.16. Furthermore, the oval section of the nozzle port is simplified with a stepwise mesh and a rectangular approximation for the nozzle (Figure 4.17).

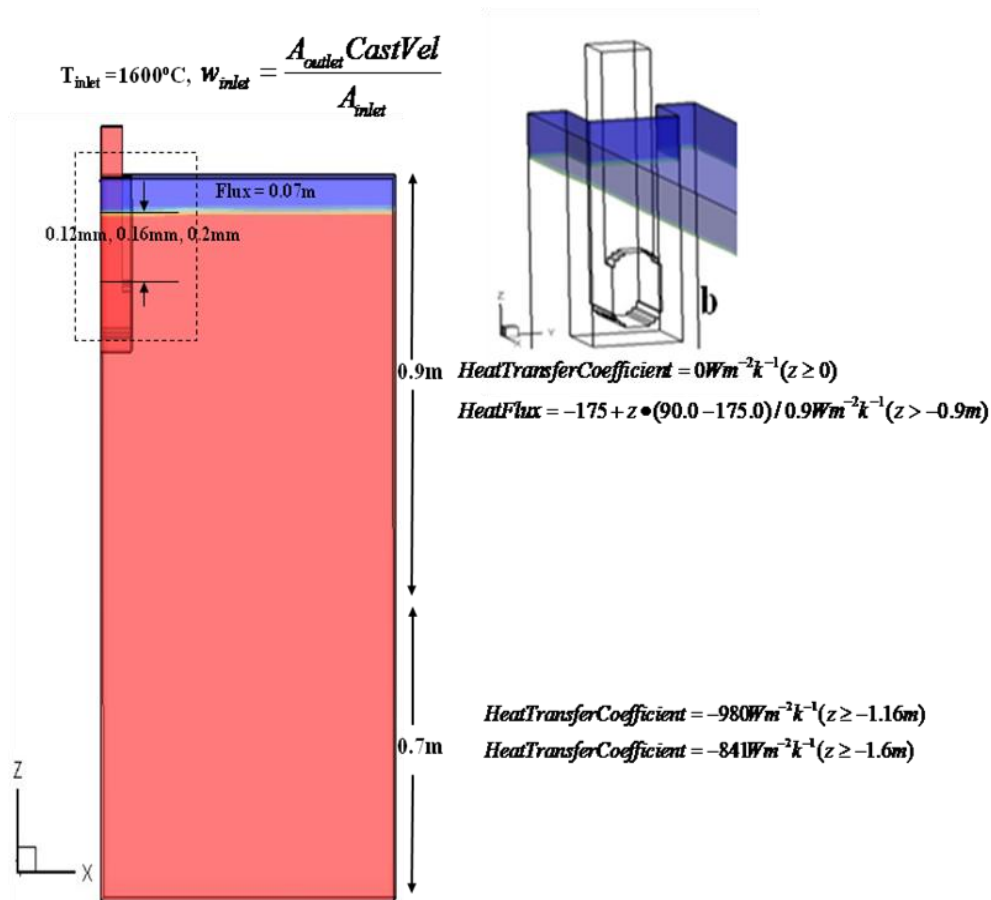


Figure 4.17: Dimensions and boundary conditions plus nozzle design.

The inlet velocity at the top of the port is calculated by the mass balance equation, and the inlet turbulent quantities of  $k$  and  $\varepsilon$  are dependent on the inlet diameter. These parameters are calculated by empirical expressions as in equation 4.2. The steel enters the domain through the inlet at a fixed temperature of  $1600^{\circ}\text{C}$ . The ambient temperature is  $22^{\circ}\text{C}$ . The solidified steel moves vertically in the casting direction and mould oscillation for this model is ignored. The boundary conditions for heat transfer are taken from previous investigations by the University of Greenwich [5, 52]. The heat flux in the mould is dependent on the  $z$  axis with a heat transfer coefficient of  $-980 \text{ Wm}^{-2} \text{ K}^{-1}$  between the mould exit and the 1.16m slab region. A heat transfer coefficient of  $-841 \text{ Wm}^{-2} \text{ K}^{-1}$  is applied to simulate the second spray region.

The predicted results are compared to previous computations and plant measurements as well as industrial data provided by Arcelor. Validation with a detailed description of the results is presented in Chapter 6.

## Chapter V

### 5 Data Analysis and Validation using the Water Model Configuration

Water model experimental techniques, such as PIV and LDA, have been applied by many scientists [118, 119, 120], in order to establish the flow pattern and enhance the understanding of the phenomena present inside the CC process. Experimental measurements using the LDA technique were conducted by ArcelorMittal Research in Metz, with the purpose of measuring the horizontal velocity and to visualise oil plus gas behaviour in the CC mould. The data so obtained enhances both quantitative and qualitative understanding of the meniscus behaviour, and related phenomena. The measurements and visualization are then used to validate the CFD model described in Chapter 3.

The main purpose of this chapter is to comprehend the dynamic oscillation of the steel/slag interface in terms of the physical parameters of the CC process, by analysing the experimental data and correlating the information against the flow field determined by the simulation. To achieve this, it is important to examine the transient behaviour of the flow and several parameters which affect it. Seven measurements points track the transient behaviour of the free surface and these will be used for the validation.

Calculations were carried out for various SEN casting velocities and gas flow rate with a 2cm oil top layer and without. The nine cases studied are presented in table 5.1.

Velocity	With 2cm oil/without gas	With air /without gas	2cm oil –Gas 2Nl/min
0.5m/s	1A	1B	1C
0.8m/s	2A	2B	2C
1.018m/s	3A	3B	3C

Table 5.1: Experimental and numerical cases studied.

A qualitative evaluation of the results against the water model visualizations is used to explain the main flow patterns observed and to validate the predicted deformation of the meniscus. A quantitative comparison against the LDA velocity measurements is provided at the seven measurement positions based on mean values and standard deviations of horizontal velocity. The nature of the observed wave action is analyzed by its spectral pattern. The dominant measured frequencies are correlated against the turnover time of the top and bottom recirculation regions in the caster for various SEN casting velocities and gas flow rates.

## 5.1 Qualitative results

Due to the overestimation of turbulence energy, as discussed in section 4.2.2, the initial use of a first order Hybrid differencing scheme (with the standard  $k$ - $\epsilon$  turbulence model) was not very successful in reproducing the experimental results. Drastically improved correlation is obtained with the higher-order scheme SMART (bounded QUICK variant) or by using the Hybrid scheme but with turbulence suppressed in the oil layer. The use of the second order scheme reduces false diffusions and generally leads to more accurate predictions for validation of the LDA data for the mean value and standard deviation of horizontal velocity.

The turbulent viscosity and predicted oscillation of the horizontal velocity for both schemes are illustrated in Figures 5.1 and 5.2. They indicate that the two solutions, discussed in the previous chapter, are capable of resolving the oscillation of the oil/water interface. Nevertheless, the monitor history of the horizontal velocity distribution at the point near the oil (point 4, Figure 5.2) reveals that the SMART scheme produces a better match with the water experiments. Unfortunately, a visual observation demonstrates that the simulation performed with the first-order scheme leads to oil layer suppression approximately after 50s simulation time.

Figure 5.1 shows that the features of the flow fields predicted by the two schemes are essential the same, with the highest turbulence being in the centre of the upper loop, and a second maximum close to the impingement region on the narrow faces. However, there is a significant difference in the size of the high turbulence region, which is more extensive in the SMART simulation. The shape of the interface remains similar between the two cases.

As we shall see in the next section the evolution of the gas field and its influence on the oil/water interface are more accurately represented by the SMART scheme.

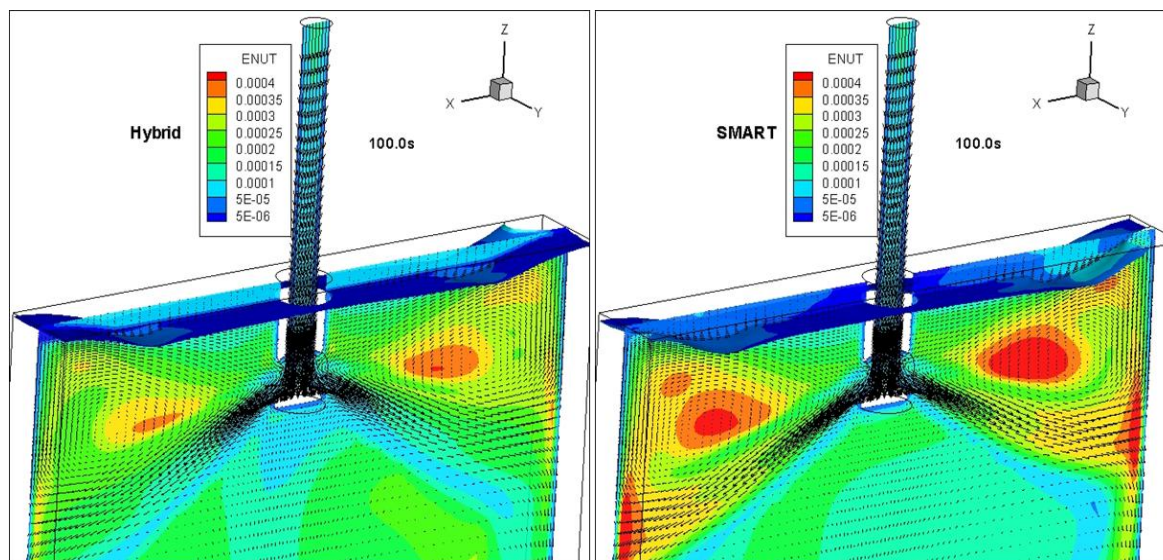


Figure 5.1: Comparison of turbulent viscosity between Hybrid (turbulence model is eliminated in the oil layer) and SMART schemes, shown together with velocity vectors and the iso-surface of the interface.

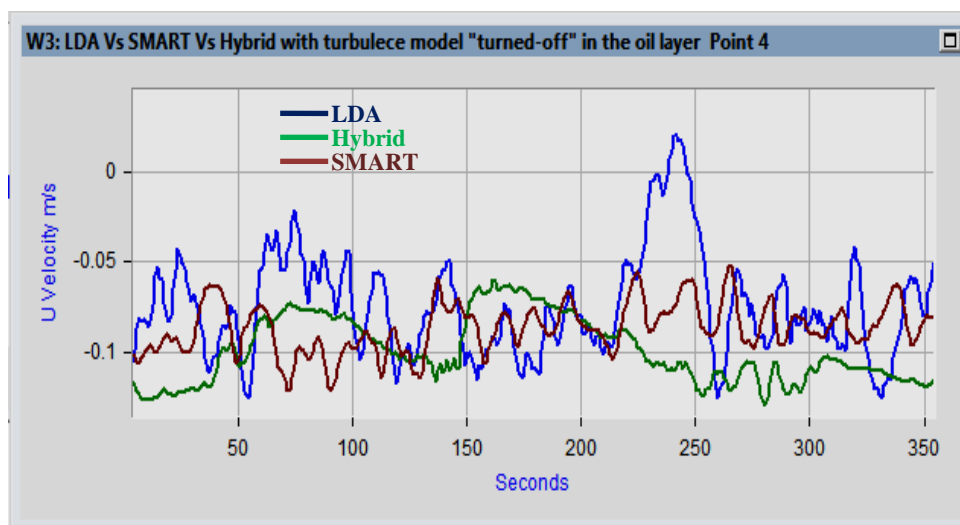


Figure 5.2: Monitor point history comparison between the SMART scheme, Hybrid scheme (turbulence model eliminated in oil layer) and experimental point 4.

### 5.1.1 Oil behaviour

Water/air and water/oil interfaces are tracked through time in the numerical simulation and LDA experiments so as to examine the influence of the slag layer. Numerical and experimental results show an almost flat water/air interface (Figure 5.3) but a disturbed water/oil interface (Figure 5.4), its deformation increasing with water flow rate. This

characteristic is pointed visually by observing the experimental interface profile and plots of the free surface contour of the numerical results. The first comparison between CFD and experiments is carried out making use of a 2cm-thick oil layer without gas and for an inlet velocity of 1.018m/s. Based on these results, there is evidence that the oil/water interface is pushed upwards near the narrow faces of the mould due to the momentum carried by the top recirculation loop as depicted in Figure 5.3.

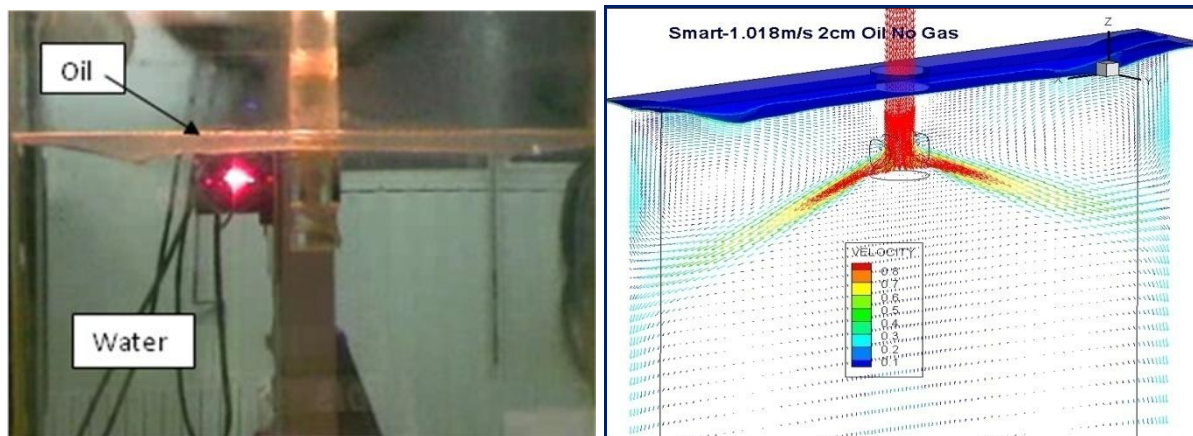


Figure 5.3: Qualitative comparison between experimental and numerical results with a 2cm oil layer and inlet velocity of 1.018m/s.

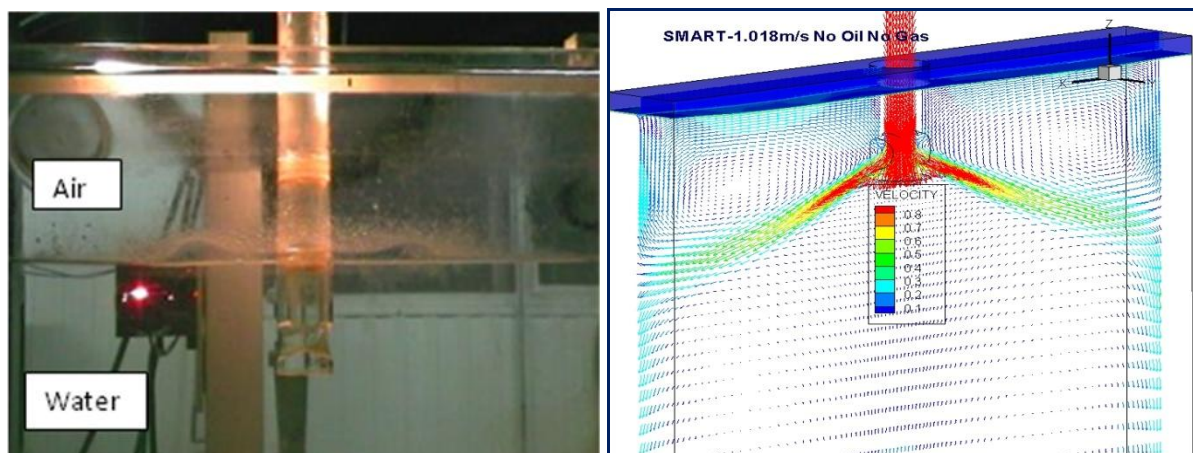


Figure 5.4: Qualitative comparisons between experimental and numerical results without oil and an inlet velocity of 1.018m/s

In continuous casting, a low value of steel flow rate is the main factor for clogging phenomena [67]. On the other hand, high flow rates force the oil layer away from the narrow faces due to the strongest flow presented in the top loop of the SEN jet. This may also expose the steel free surface to the air causing oxidation of the steel and loss of heat in the steel. Moreover, the higher shear close to the interface is linked to the entrapment of the mould powder.

These observations are tested in the water model experiments and the CFD simulations. The immersion depth, that is the distance between the water level and the highest point of the nozzle ports, is kept stable at 68mm in these simulations and there is a top oil layer representing slag which is 2cm thick. Figure 5.5(water model) and Figure 5.6 (simulations) show the level of qualitative agreement obtained with the SMART scheme for three water flow rates. Figure 5.5c and Figure 5.6c show that the increase in the water flow rate causes bigger deformation in the oil layer and, leads to uncovered edges of the caster, as expected.

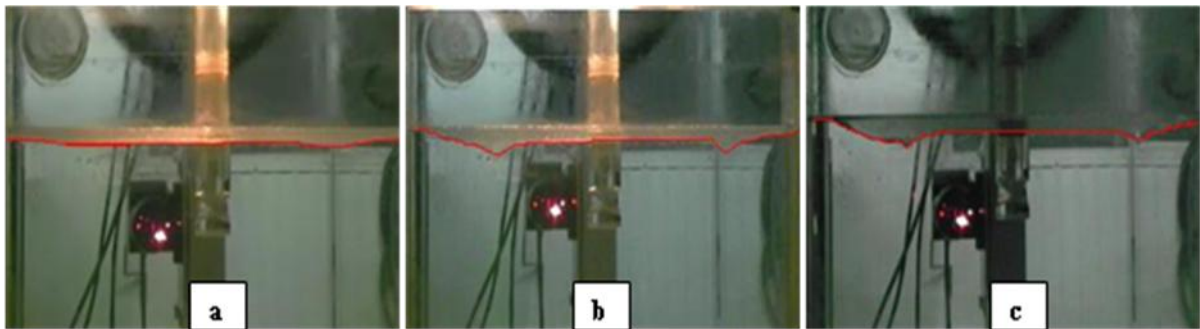


Figure 5.5: Free surface profile for different water flow rate in experiments. a) 0.5m/s b) 0.8m/s c) 1.018m/s. The interface has been highlighted in the pictures for ease of identification.

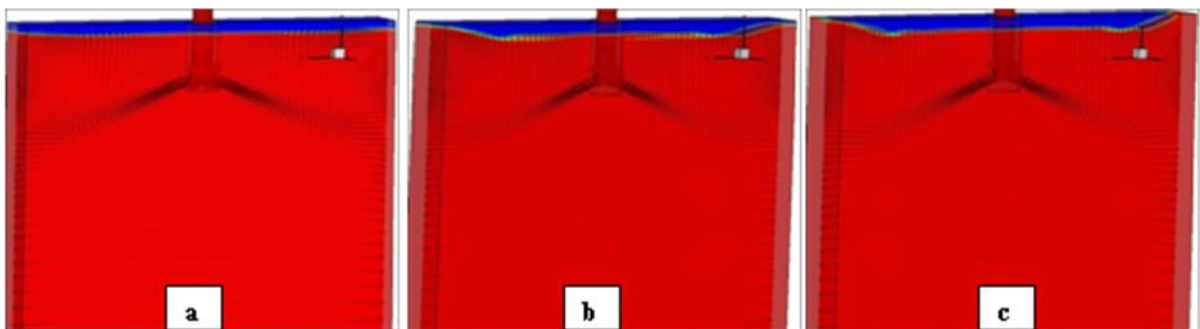


Figure 5.6: Free surface profile for different water flow rate in CFD simulations with velocity vectors shown in the middle plane. a) 0.5m/s b) 0.8m/s c) 1.018m/s

### 5.1.2 Gas behaviour

It has been observed through LDA experiments that the injection of gas at a rate of 2Nl/min has an important influence on the flowfield in general, but also on oil/water interface behaviour. The main observation in the water model measurements is that the presence of air near the nozzle creates an upturned water flow which forced the oil layer to spread out over the whole surface preventing the exposure of the water as depicted in Figure 5.7. At the same time, there is a significant mixing of air, water and oil in the region surrounding the SEN tube.

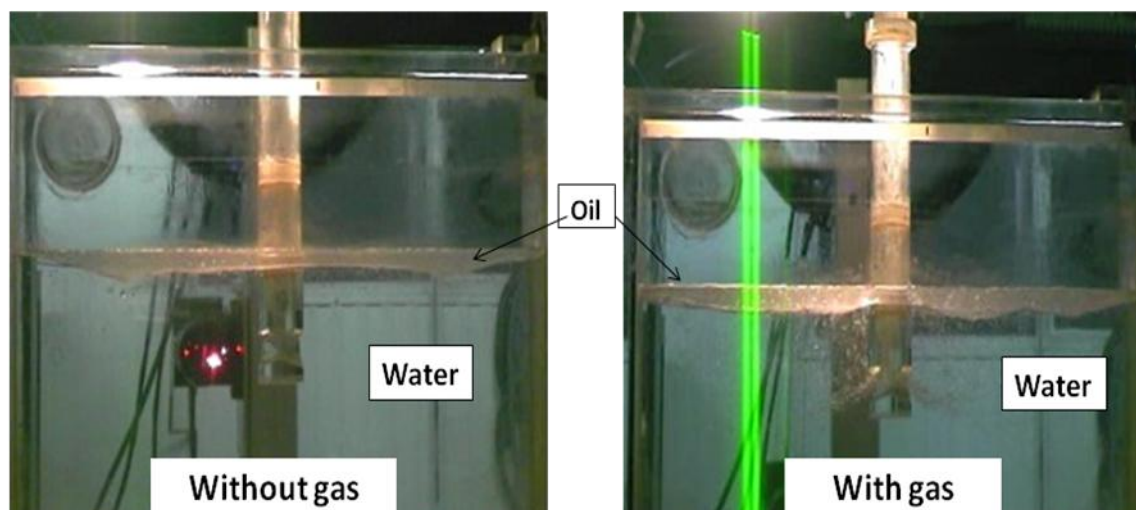


Figure 5.7: Influence of gas flow rate in the LDA experiment: (a) No gas, (b) 2Nl/min - Inlet velocity 1.018m/s.

The influence of the gas on the wave action is depicted in Figure 5.8 by the combination of instantaneous water-oil interface, contours of argon volume fraction and velocity vectors. However, the main difference is that the gas, in the experiments, is concentrated very close to the nozzle, whilst in the simulations, the gas appears to travel further along the jet before it turns to the surface due to buoyancy. In addition, it is difficult to see the small bubbles in the experiment but the large bubbles are clearly seen in Figure 5.7, behaving in a similar fashion. In both cases, the free surface shape is affected by bubbles coming out of the mould, which locally drag up the free surface. It is observed that the jet is strongly affected due the forces exerted by the bubbles, creating an upward movement of water flow near the nozzle while the classical double roll structure still persists. In addition, it can be declared that particle trajectories and removal rate depend on particle size as already reported in previous studies [23, 26, 121]. In Figure 5.8 the largest bubbles are represented by black traces illustrating that they are readily escaping through the top surface and in their passage affect the slag layer. In contrast the smallest ones, represented by red, are transported deeply into the slab, following the downward circulation of steel flow below each jet. Additionally, these small bubbles flow very close to the wall and may become entrapped in the solidifying strand in a real caster.

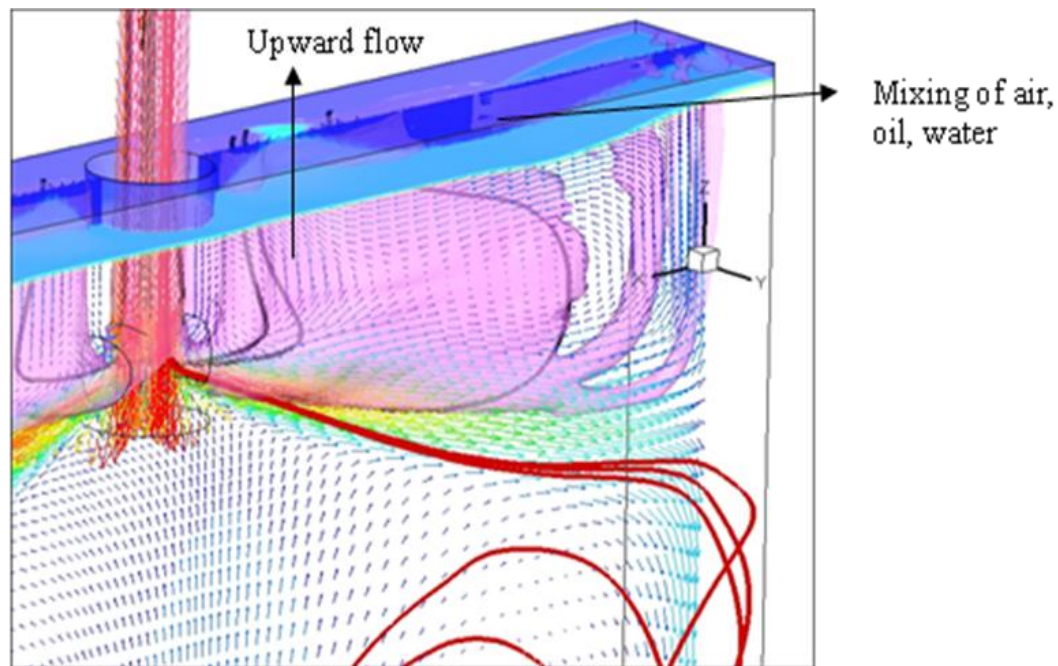


Figure 5.8: Influence of gas flow rate - 2Nl/min - 2cm Oil - Inlet velocity 1.018m/s

In the simulation, 5000 representative “particles” are tracked, with the total gas volume of 2l/min divided into nine distinct size groups, ranging in diameter from 0.1mm to 6.8mm. Typical bubble trajectories of six different sizes are presented in Figure 5.9, where the colour of each track corresponds to the diameter size of bubbles. Computed particle trajectories with a diameter greater than 1mm move upwards to the top surface from where they escape. A closer view of the port exits shows that the position within the port also depends on the particle size, with large bubbles exiting at the top of the ports, and moving close to the SEN walls. As mentioned before, the large particles deform the oil layer at the top, near the SEN. Particles of 0.1mm (blue colour) exit the lower edge of the nozzle port and tend to follow the liquid flow. As a result their movement is linked either to the upper roll or the lower roll. The influence of gas is further examined numerically by analysing the meniscus velocity fluctuation. Numerical confirmation of the qualitative predictions is presented in the next section, including details of the spectral analysis carried out and of several parameters which affect the stabilization of the steel flow pattern.

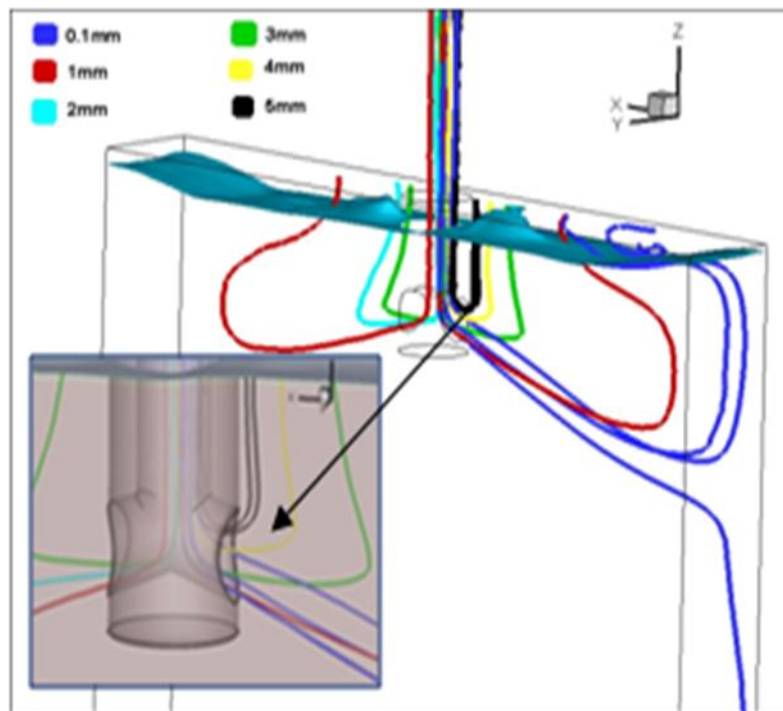


Figure 5.9: Particles tracks of six different diameter sizes

## 5.2 Quantitative results

The distribution of the horizontal velocity in time was monitored at 7 points along the middle plane ( $y=0$ ) of the mould acquired by LDA in a period of 10 minutes. Points 1, 4 and 5 are close to the oil layer and are affected by the top recirculation loop as depicted in Figure 5.10.

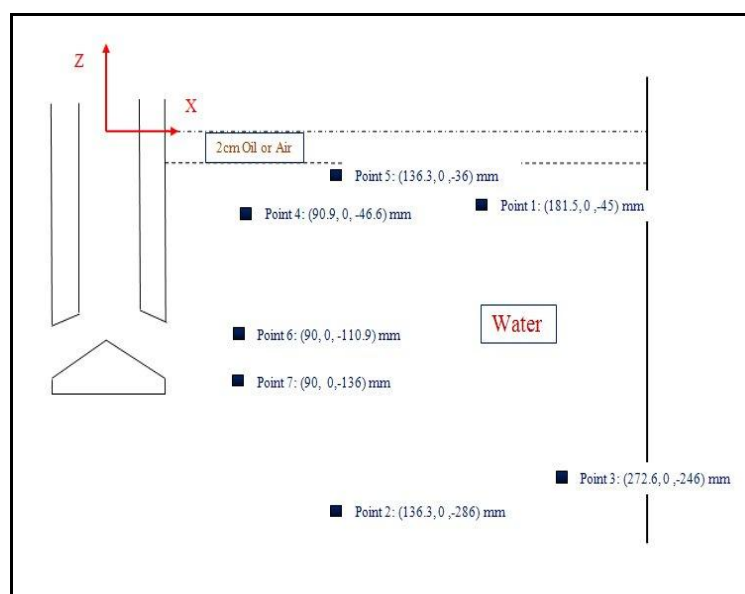


Figure 5.10: Experimental measurements arrangement for LDA and computation results.

Consequently these points give information about the strength of the top recirculation loop and the influence of the oil layer on the meniscus velocity. Points 2 and 3 are in the lower part of the mould and are influenced by the bottom recirculation loop. Points 6 and 7 are at the exit port where high velocities are obtained and their values are affected by the strength and the oscillation of the SEN jet. Special attention is given to the horizontal velocities close to the meniscus (points 1, 4 and 5) since they provide knowledge of the possible entrainment of slag. Furthermore, they characterise the hydrodynamic aspects of the water/oil interface behaviour and in particular the effect of injected gas bubbles.

Simulations of the order of 400s are necessary, in order to capture the longest period of the lower loop oscillation. Consequently, 40000 samples are recorded with time step of 0.01s, which proves costly in total calculation time. It takes approximately 2 months for the SMART scheme and 27 days for the Hybrid scheme for each case studied. The simulations ran in serial mode in a cluster machine with sixteen cores in each node and 32 GB memory. It is important to note that in the following results those obtained with the Hybrid scheme entail the elimination of turbulence within the oil layer. Simulation results with the second order SMART scheme were performed without any modification in the turbulence model and all the results were obtained with the improved mesh shown in chapter 4.2.1. Since the SMART scheme proved more accurate, its output horizontal velocity distribution is was for spectral analysis.

Numerical comparisons concern the mean value and standard deviation of the horizontal velocity component and with these we try to explain the dynamic behaviour of oil by examining its frequency of oscillation.

### 5.2.1 Spectrum analysis

A Fourier analysis of the signal explains the nature of the observed wave action. For the spectral analysis the DADisp [122] software was used. A Fourier analysis was carried out on both the experimental and numerical signals obtained at the 7 measuring points shown in Figure 5.10. Before the raw signal (Figure 5.11) can be used, it has to be processed as follows:

1. The data are filtered with a base of 1s.

2. Averaging around each point of the filtered signal of experiments takes place in order to obtain a smoother signal and remove high frequency noise.
3. The mean value and any linear trend are removed and only the last available 2n data samples are kept;
4. Multiplication with a smooth curve, called a Hamming window is used.
5. A fast Fourier Transform is performed.

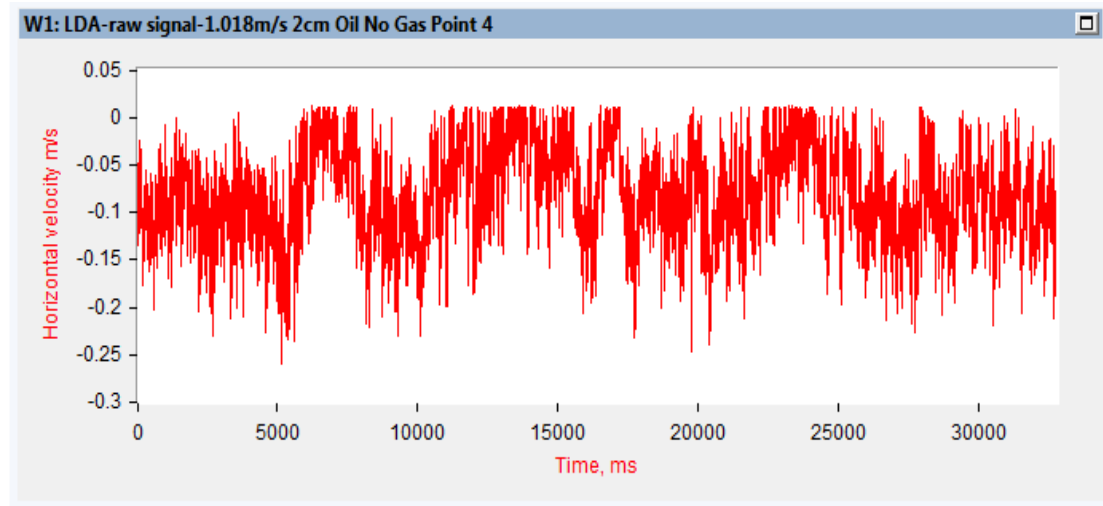


Figure 5.11: Raw signal of LDA for point 4- 2cm oil no gas and inlet velocity set at 1.018m/s.

The data set is first filtered on a base of 1s using FORTRAN code. Then the moving average function of the DADiSP software is used on the filtered signal of the experiments in order to smooth out thig high frequency noise. This function takes as input a series  $S$  and a specified number of points  $n$  to average. The output signal is attained by averaging around each point using the average of  $n$  points. A general example with 3 points is given below.

Input Series:  $S = \{S[1], S[2], \dots, S[n]\}$

Points: 3 (Number of points to average as the series is processed).

Return series:  $\{ (S[1])/1, (S[1]+S[2])/2, (S[1]+S[2]+S[3])/3, (S[2]+S[3]+S[4])/3, \dots, (S[n-2]+S[n-1]+S[n])/3, (S[n-1]+S[n])/2, (S[n])/1 \}$

A spectral analysis is then performed so as to get a normalized magnitude plot, applying Hamming window. The mean value of the data is removed and only the last available 2n data samples are kept. The same process is followed in the filtered signal of the numerical result. Using the above process we predict the characteristic oscillations observed throughout the

experiment. The oscillations are composed of several periodic components such as upper and lower recirculation loop, oil/ water interface and nozzle jet flapping.

Figure 5.12 shows a comparison between the experiments and the numerical simulation for case 2B of table 5.1, with inlet velocity of 0.8m/s for point 4. The red traces are for LDA using the already filtered original signal. The blue traces are numerical results with a simulation time of 400s and a time-step of 0.01s using the SMART scheme. The upper line shows the filtered data with a base of 1s, the middle line is the smoother signal applying average function for each case and the lower line is the power density spectrum with two main peaks. Furthermore the spectrum result in the lower line can be multiplied by itself in order to remove weak peaks and depict only the major peaks.

Both results highlighted two low main frequencies, one peak at  $\sim 0.025\text{Hz}$  (period of 40s) and another at  $\sim 0.037$  (period of 27s). The LDA peaks are higher than the numerical spectrum results (note that the amplitudes scale is different). Considering that point 4 is in the upper loop area and close to the free surface, it can be assumed with some certainty that the one frequency represents the oscillation of the upper loop and the other frequency represents the jet oscillation. This will be clarified later on.

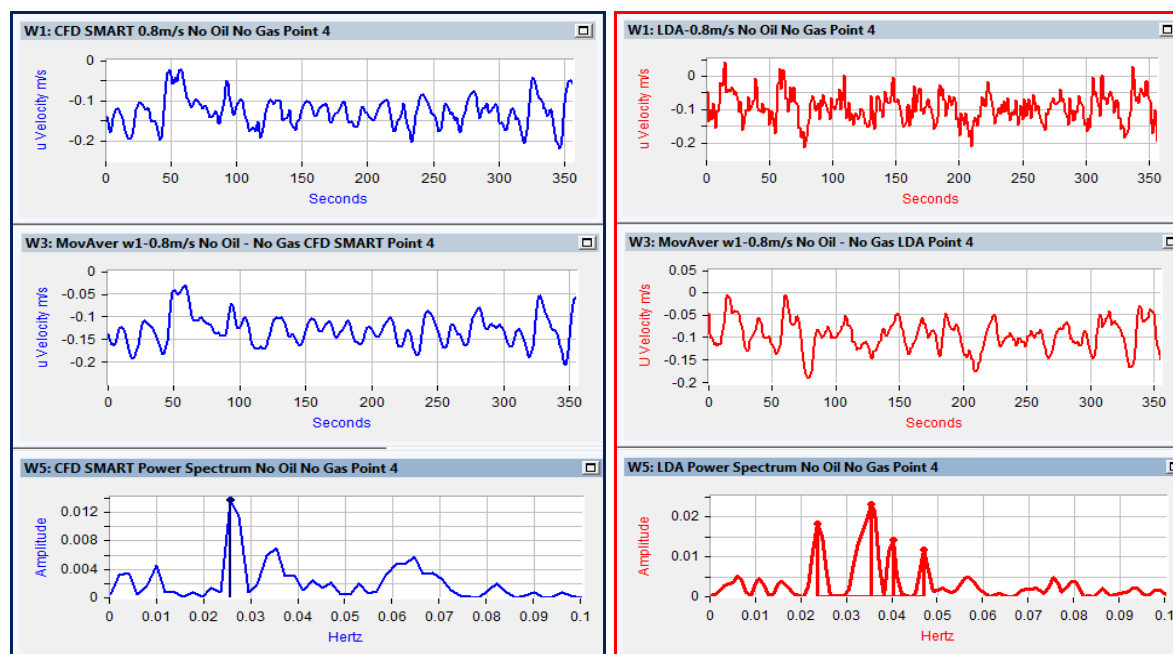


Figure 5.12: Comparisons of filtered signal and spectrum between LDA (red) and CFD (blue). The spectrum is for point4 for case 2B of table 5.1 and inlet velocity set at 0.8m/s.

## 5.2.2 Comparing numerical results against LDA experiments

Comparisons refer to the mean value and standard deviation of the velocity; they are used to explain the dynamic behaviour of oil by linking the frequency of oscillation to the predicted flow pattern. Typical comparisons between LDA measurements and both numerical schemes are illustrated in Figures 5.13-5.15. As a reminder, the numerical results are accomplished with Hybrid (turbulence model “turned off” in the oil layer) and SMART schemes using the standard  $k$ - $\epsilon$  model. Note that the initial transient, of approximately 10s, is excluded from the statistics. Figure 5.13 presents the mean values and standard deviation of the x-component of the horizontal velocity for case 1A (0.5m/s 2cm Oil) of Table 5.1. Figures 5.14 and 5.15 show the case with an inlet velocity of 0.8m/s, with air (case3B of table 5.1) and oil (case 2A of table 5.1) respectively. Both measurements are characterized by a negative horizontal velocity at the meniscus (Points 1, 4 and 5). Note that the total velocity fluctuation of the horizontal velocity is estimated considering two contributions; one is the low frequency variation which is resolved by the calculation and the other part is due to the turbulence derived from the kinetic energy of turbulence in the  $k$ - $\epsilon$  model (variable  $k$ ) as described in equation 4.4.

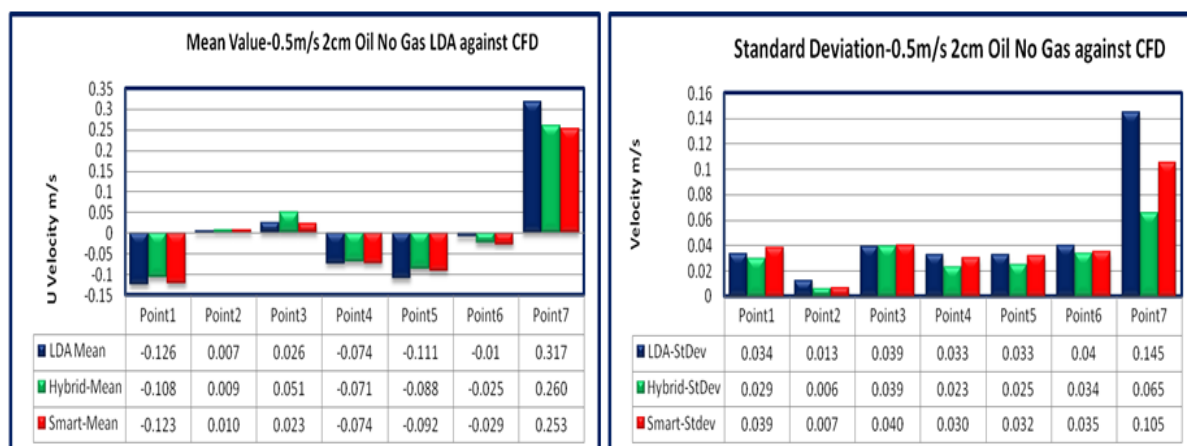


Figure 5.13: Comparisons of Mean values and Standard Deviations between LDA and CFD for the case with inlet velocity of 0.5m/s with 2cm Oil and without gas.

Commenting on the accuracy of the simulations, it is clear that the quadratic upwind scheme SMART, gives a markedly better agreement to the experiments in almost all points, although the Hybrid scheme performs reasonably well, especially for mean value calculations. The SMART scheme provides a superior match for standard deviation, a measure of reduced numerical diffusion.

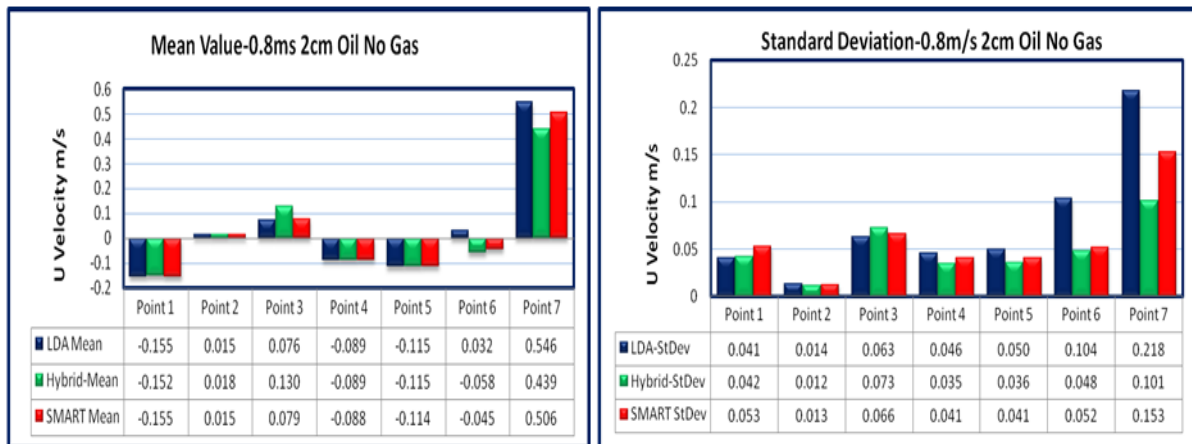


Figure 5.14: Comparisons of Mean values and Standard Deviations between LDA and CFD for the case with inlet velocity of 0.8m/s with 2cm oil and without gas.

Figure 5.15, shows the case without an oil layer cover, which means interfacial waves are absent or have a very small amplitude. Nevertheless, fluctuations persist inside the mould as shown in the standard deviation values which are of the same order of magnitude as the case with oil. Regarding the relative scheme performance, the same comments apply as above.

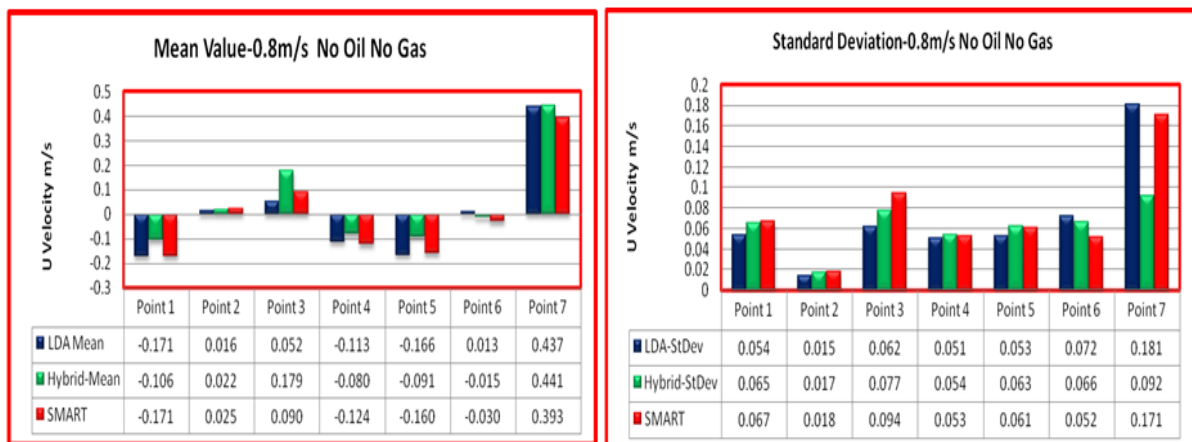


Figure 5.15: Comparisons of Mean values and Standard Deviations between LDA and CFD for the case with inlet velocity of 0.8m/s with 2cm air and without gas.

The largest discrepancy tends to be in positions 6 and 7, which lie in the high shear region at the edge of the SEN jet, where small errors in positioning can have a large effect on the measured/computed value. The main reason for the disagreement for point 6 is the oscillation of the jet during water experiments. The positive and close to zero mean values of the horizontal velocity in LDA, demonstrate that point 6 is located between the exit jet area and the end of the upper recirculation loop. This can be proven by taking the distribution of the horizontal velocity, whose samples get both positive and negative values in LDA. In contrast, numerical results show that point 6 is closest to the end of the upper loop area where negative horizontal velocity is expected (Figure 5.16).

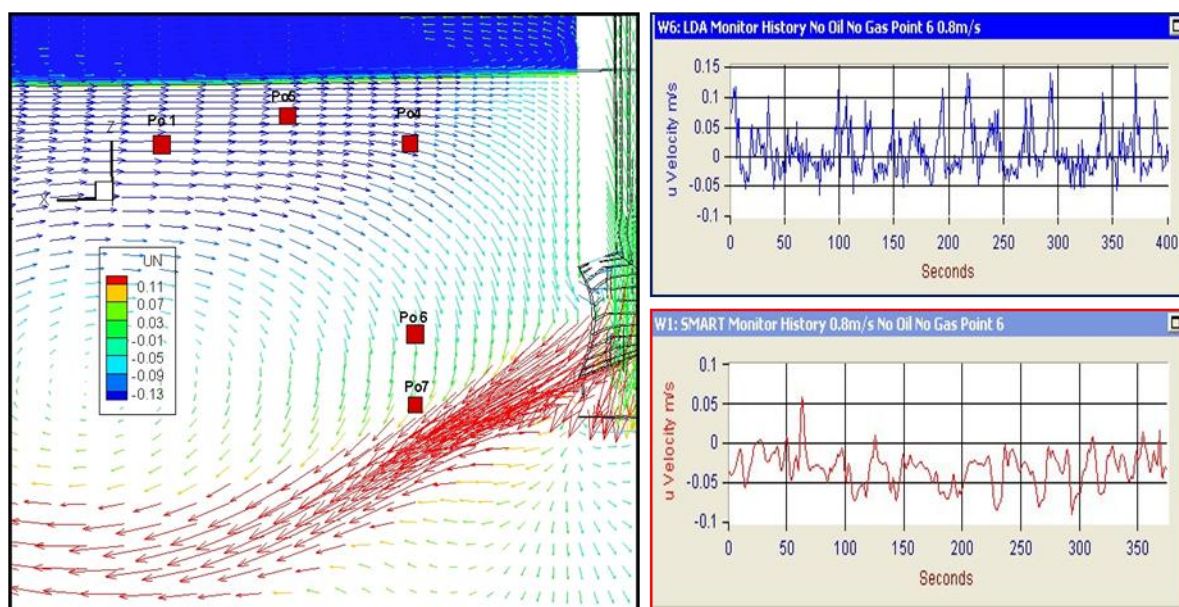


Figure 5.16: Comparison of horizontal velocity distribution between LDA and CFD at point 6.

### 5.2.3 Influence of water flow rate

Comparing the results between the three different water flow rates is interesting as the value of the steel flow rate is linked to the speed of production and therefore considered to be one of the important factors that affect the quality of the steel product. It is already observed from qualitative comparisons that the entry flow rate variations have a strong influence on the flow pattern, hence affecting the free surface profile in the continuous casting of steel.

Comparing LDA and numerical results for the case with 2cm oil and without gas (column A of table 5.1) one can clearly examine the influence of water flow rate. Figure 5.17 shows that the mean value increase is proportional to the water flow rate. The opposite behaviour is observed for point 4 with a higher velocity of 1.018m/s when we have an oil layer. The only explanation for this change is that the oil seems to appear at this area due to its highly dynamic behaviour which is also an evidence of the entrapment of the oil layer. However this phenomenon was not investigated and should be considered for future study. This discrepancy does not exist when considering the influence of water flow rate with no oil at the top (column B of table 5.1) which suggests the presence of oil in the area of point 4 may be the reason. In this case, the horizontal velocity for all points increases with the inlet velocity (Figure 5.18). Furthermore the negative horizontal velocity at the meniscus implies that the two major loops persist either with air or oil at the top. The absolute mean values of

the meniscus velocity (point 1, 4 and 5) increase with the inlet velocity, producing a stronger upper loop, hence lead to bigger amplitudes of oil fluctuation. The latter was presented previously in qualitative comparisons between experiments and computational results. The same effect is observed on the standard deviation as shown in Figure 5.19. In conclusion, it can be stated that the quantitative results are entirely consistent with the previous qualitative observations.

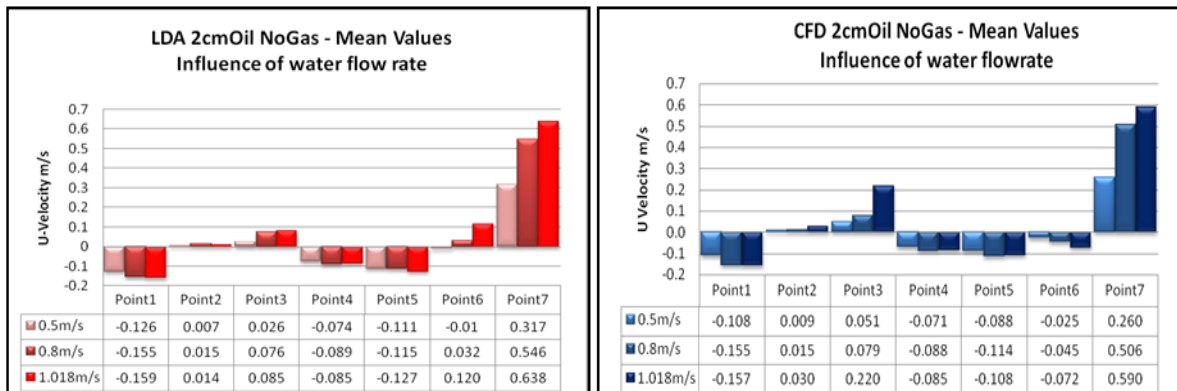


Figure 5.17: Influence of water flow rate in mean value of horizontal velocity in case with 2cm Oil without gas using LDA and CFD results.

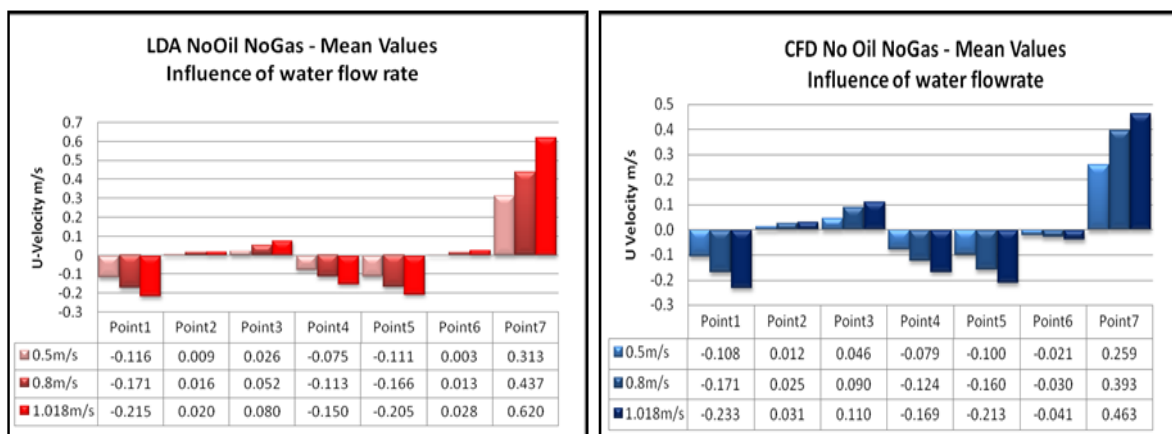


Figure 5.18: Influence of water flow rate in mean value of horizontal velocity in case with 2cm air without gas using LDA and CFD results.

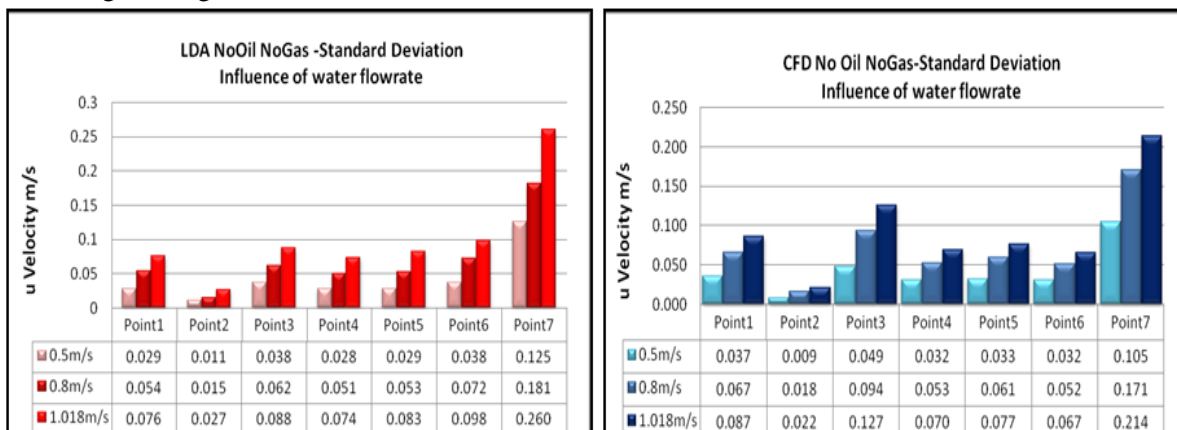


Figure 5.19: Influence of water flow rate in standard deviation of horizontal velocity in case with 2cm air without gas using LDA and CFD results.

### 5.2.4 Influence of oil (Free surface)

The influence of oil can be illustrated by comparing the case of 2cm oil but without gas against the case of air at the top without gas. Particular attention is paid to the points near the oil layer since they characterize the flow pattern of the upper loop and the velocity fluctuation in the meniscus.

Figure 5.20 presents the LDA measurements, where negative horizontal velocity means that a double flow pattern exists either with oil or air. In the case of inlet velocities set at 0.8m/s and 1.018m/s with the presence of the oil layer above the water the negative mean values of horizontal velocity increase (absolute values decrease). This observation verifies that the oil layer can affect flow stability. Observations for the case of inlet velocity at 0.5m/s predict almost the same mean values and standard deviations. This verifies the qualitative visualization in the previous chapter, where oil/water or air/water interface are almost stable for the lower velocity. For the standard deviation it is observed that at lower velocities standard deviation increases due to the oil but decreases at higher velocities (Figure 5.21).

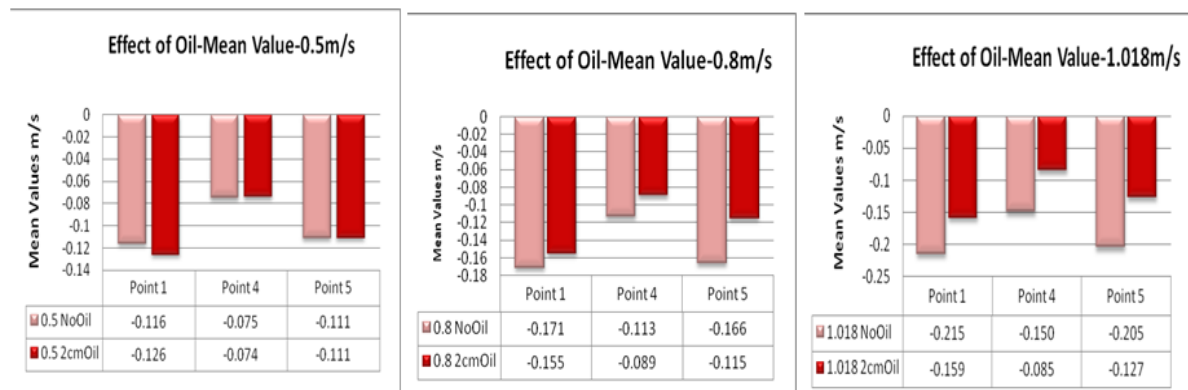


Figure 5.20: Influence of oil layer on the horizontal velocity at the meniscus - Mean Values for point 1, 4 and 5 using LDA.

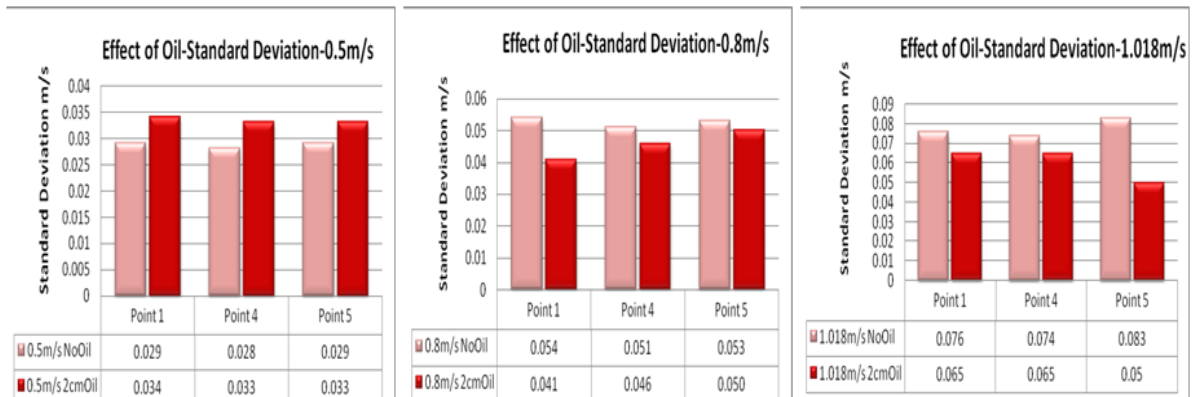


Figure 5.21: Influence of oil layer on the horizontal velocity fluctuation at the meniscus- Standard Deviation for point 1, 4 and 5 using LDA.

Numerical results are then used, in order to validate the influence of oil occurring in experiments. Mean values and standard deviations in Figure 5.22 and Figure 5.23 respectively, show that the presence of oil at the top increased the horizontal velocity and decreased the horizontal fluctuations in higher velocities. In the cases with low velocity, almost the same mean values and standard deviations between the two cases are observed. Nevertheless, according to both LDA and CFD results, it can be stated that there is no influence of the slag layer on the flow pattern at the lower steel flow rate. In addition, there is an obvious quantitative and qualitative connection, as numerical measurements establish the fluid flow stabilization determined by visualizations.

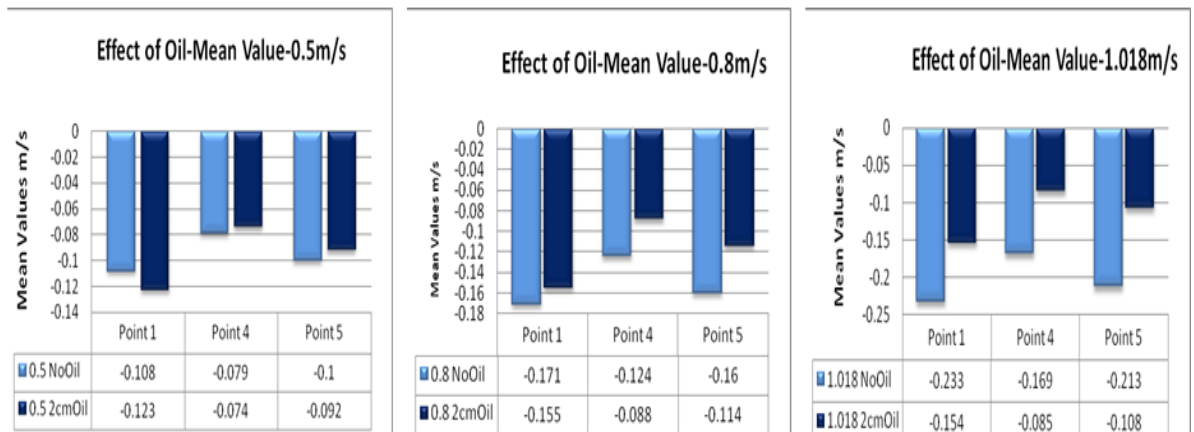


Figure 5.22: Influence of oil layer on the horizontal velocity at the meniscus - Mean Values for point 1, 4 and 5 using CFD.

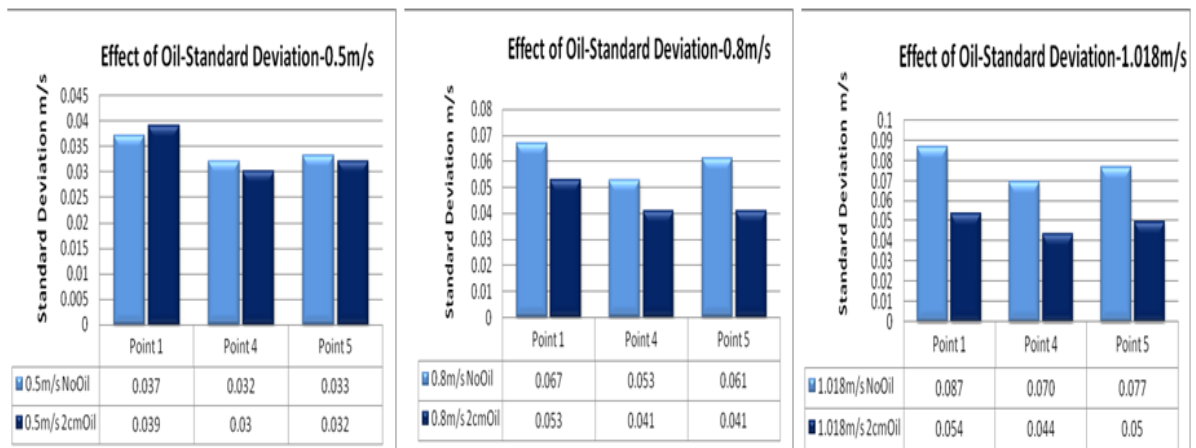


Figure 5.23: Influence of oil layer on the horizontal velocity fluctuation at the meniscus- Standard Deviation for point 1, 4 and 5 using CFD.

### 5.2.5 Influence of gas

Qualitative observations presented in the previous chapter predict that the loop in the upper part with a flow coming from the narrow face towards the SEN is slowed down by the gas injection. This is because the bubble-laden fluid rises to the surface near the nozzle wall taking some of the initial jet momentum with it. The elimination of the air bubbles induces flow modification and the meniscus velocity is directly affected. This can be verified by calculation of the mean value and standard deviation of the horizontal velocity component.

Figures 5.24-5.26 present the influence of gas flow rate (2L/min) on the mean value and standard deviation of the velocity at the meniscus for three inlet velocities using LDA. As expected the mean value of the velocity at the meniscus increased and standard deviation decreased due to the presence of the gas. A different trend is presented for the mean value of point 4 in the experimental measurements at an inlet velocity of 1.018m/s (Figure 5.26). The reason for the above discrepancy is still not clear at present.

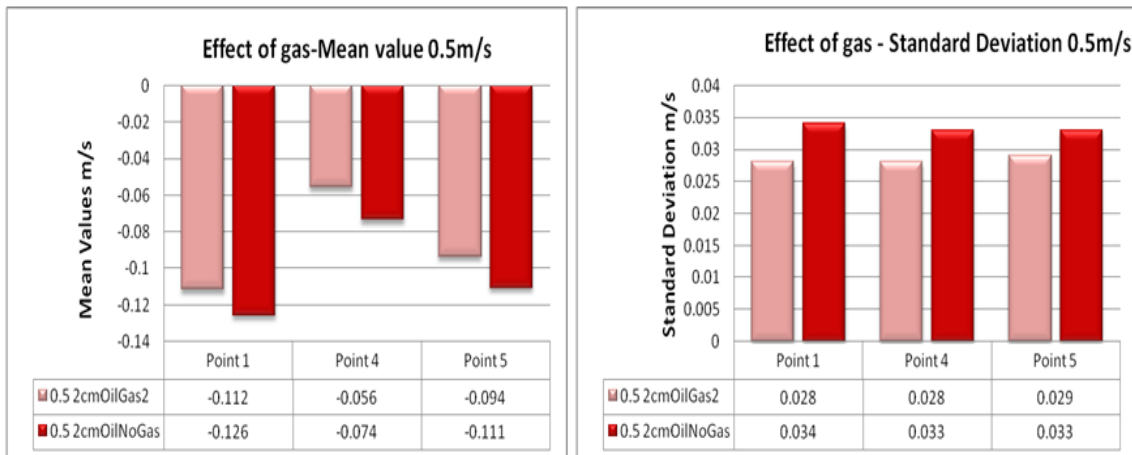


Figure 5.24: Influence of gas injection on the horizontal velocity (mean value) and fluctuation (standard deviation) at the meniscus using LDA. Comparison between case 2A (0.5m/s 2cm Oil No Gas) and 2C (0.5m/s 2cm Oil Gas 2L/min)

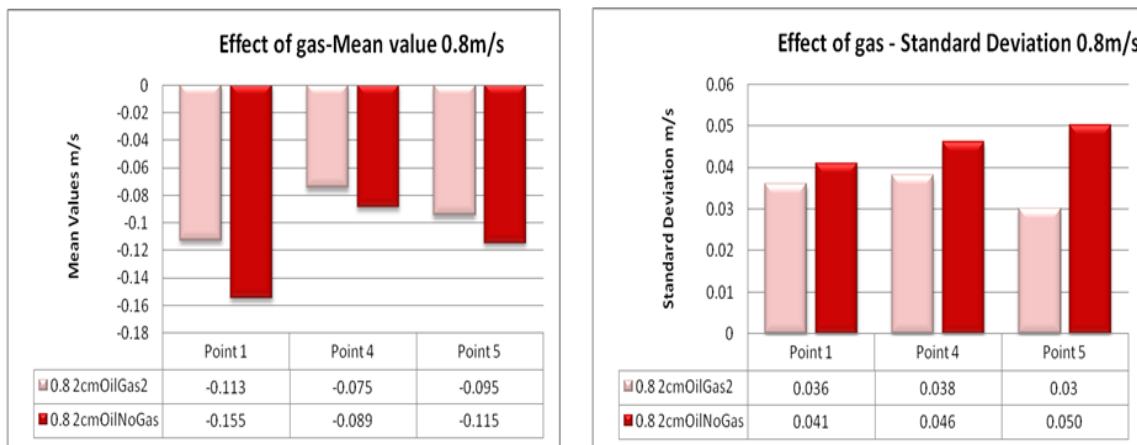


Figure 5.25: Influence of gas injection on the horizontal velocity (mean value) and fluctuation (standard deviation) at the meniscus using LDA. Comparison between case 2A (0.8m/s 2cm Oil No Gas) and 2C (0.8m/s 2cm Oil Gas 2L/min)

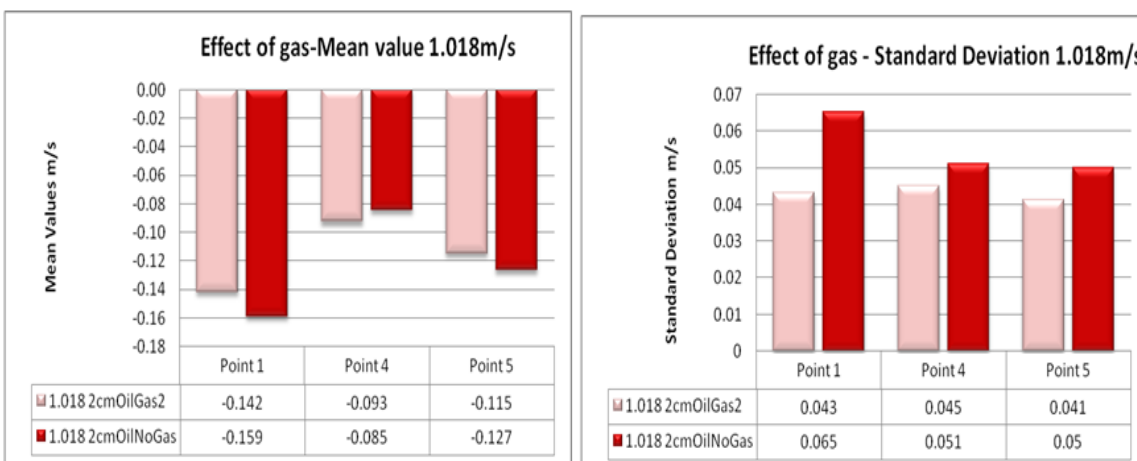


Figure 5.26: Influence of gas injection on the horizontal velocity (mean value) and fluctuation (standard deviation) at the meniscus using LDA. Comparison between case 3A (1.018m/s 2cm Oil No Gas) and 3C (1.018m/s 2cm Oil Gas 2L/min).

Generally, numerical predictions lead to the same deductions as the experimental results which state that the injected air gas bubbles aid the meniscus stability as the presence of buoyancy forces decreases the absolute mean value and the fluctuation of horizontal velocity at points near the meniscus (Figure 5.27 and Figure 5.28). In addition the same behaviour as in the experiment is predicted for the absolute value of mean value for point 4 in case of inlet velocity of 1.018m/s. Mean value of this point is slightly lower due to the presence of gas (Figure 5.28-left) confirming the experimental results and giving numerically an unlike behaviour. In contrast to the influence of oil, the injection of gas affects the horizontal velocity at the meniscus for all water flow rates and not only for higher rates. The same behaviour exists in the horizontal velocity fluctuation at the meniscus with the standard deviation decreasing with lower and higher velocities due to the presence of gas. On this point of view the CFD results are in disagreement for point 4 which shows a bigger fluctuation in the horizontal velocity. The numerical disagreement occurs mainly due to uncertainty in the size distribution of the bubbles which is a critical parameter of the gas flow pattern and hence to its interaction with the steel flow and the free surface. Also, complex effects, such as coalescence or breakup of the bubbles were not considered in this work.

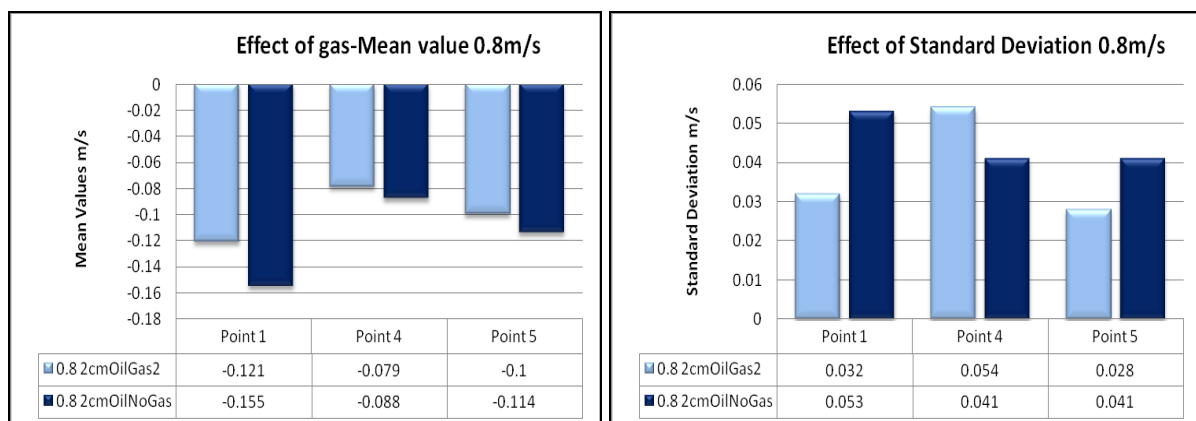


Figure 5.27: Influence of gas injection on the horizontal velocity (mean value) and fluctuation (standard deviation) at the meniscus using CFD. Comparison between case 3A (0.8m/s 2cm Oil No Gas) and 3C (0.8m/s 2cm Oil Gas 2L/min).

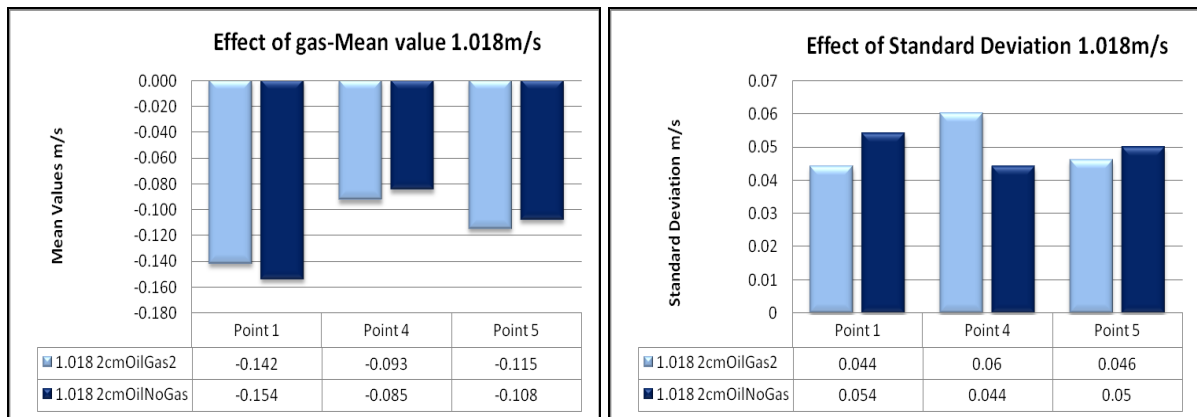


Figure 5.28: Influence of gas injection on the horizontal velocity (mean value) and fluctuation (standard deviation) at the meniscus using CFD. Comparison between case 3A (1.018m/s 2cm Oil No Gas) and 3C (1.018m/s 2cm Oil Gas 2L/min).

Validation of the numerical model was successfully achieved using the LDA water model data. Bubbles distribution is applied considering an example methodology provided by ARM described in the Figure 5.29 below.

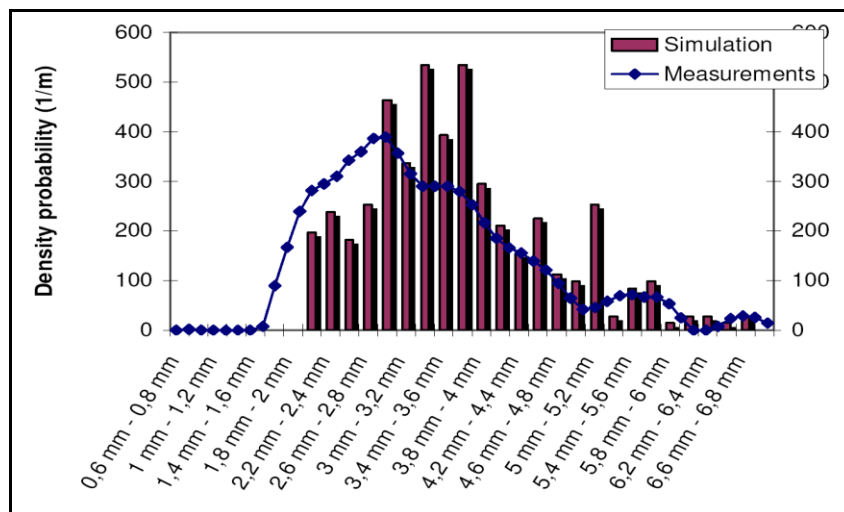


Figure 5.29: Bubbles diameter distribution provided by ARM for water model configuration.

The model first computes transient turbulent flow coupled with free surface tracking. Next this data is used as an input database to simulate the transport of the particles using a Lagrangian approach. This system is modelled as a 3-species model; this means a single liquid with a variety of components, which may have different densities and other physical/thermal properties. It is important to note that the computational time is very expensive when the gas flow rate is included. Approximate computation time is two months for 200s of a real time simulation. However the mathematical model corroborates the experimental predictions about the influence of gas. Computational results prove what is already observed by qualitative visualization and the main trends are correctly determined.

The following results show that the horizontal fluctuations decrease in the meniscus when the gas injected through the SEN, indicating that the SEN jet flapping is less active. There is an important difference between experiments as the standard deviation for point 4 increases while for points 1 and 5 decrease due to the injected gas as depicted in Figure 5.27 and 5.28.

### 5.2.6 Flow oscillation prediction

Spectral analyses are performed with the purpose of explaining the flow oscillation prediction and getting new insights on the transient flow behaviour. Previous investigations by AMR [123] identified a very low frequency of oscillation (0.012Hz) and a higher frequency (0.05Hz) oscillation. Our investigation suggests that these frequencies are linked to the lower and upper flow loops in the mould. In addition to the verification of the oscillation of these two main loops, the aim is to go one step further from previous investigations [82, 84,123] so as to give explanations of the several other predicted peaks. According to the numerical visualizations there is also an indication that the periodical jet oscillation which affects the lower loop has a role to play.

Figures 5.30-5.32 display the frequency spectrum for point 5 which is near the oil layer. Figure 5.30 is the analysis with the lowest inlet velocity with the oil layer at the top of the mould, but without gas. The LDA result is represented by the red figure while the CFD result is represented by the blue figure. A main peak is observed at 0.034Hz (29.4s) and 0.043Hz (23.3s) with LDA and CFD respectively. Figure 5.31 presents the spectrum for an inlet velocity of 0.8m/s but without the protective oil layer or gas. In this case, the main peak is observed at 0.041Hz (24.4s) in the experiment and at 0.044Hz (22.7s) in the numerical results.

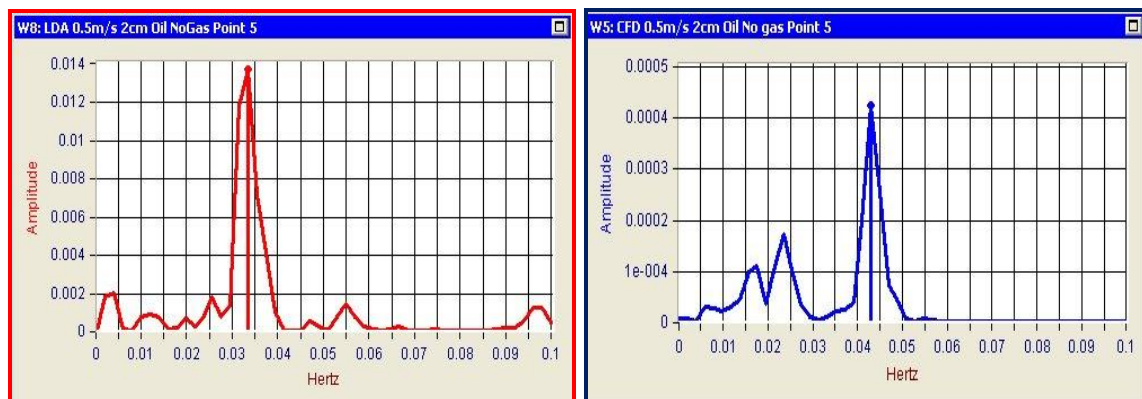


Figure 5.30: Experimental and numerical spectra for horizontal velocity components – 0.5m/s 2cm Oil no gas Point 5.

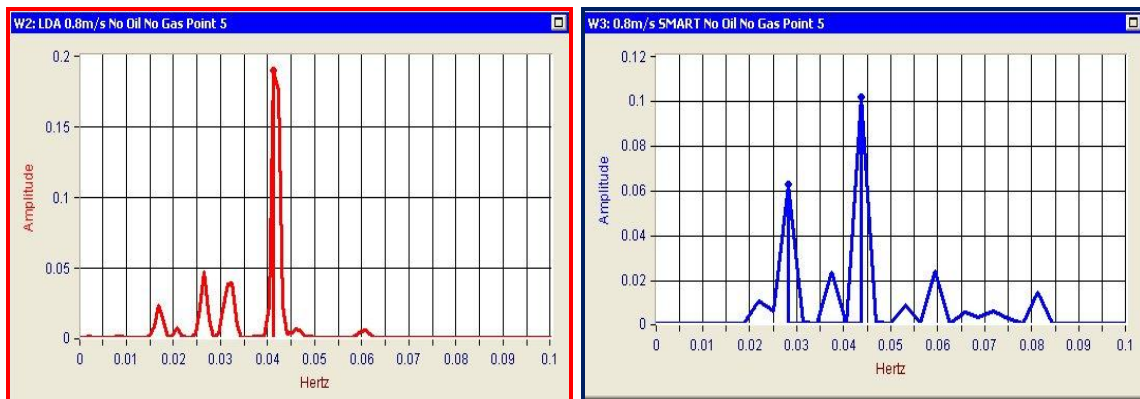


Figure 5.31: Experimental and numerical spectra for horizontal velocity components – 0.8m/s No Oil no gas Point 5.

Figure 5.32 depicts the spectrum results in the case of air being present at the top without gas and an inlet velocity of 1.018m/s for point 5 (top line) and point 2 (bottom line) located at the meniscus and the lower recirculation loop respectively. A main peak at 0.05Hz (20s) is observed for point 5 and a peak at 0.012Hz for point 2. It can be clearly seen by calculation and experiments that the periodic oscillation of this upper loop is close to 20-25s and the lower loop has an approximate period of 83s.

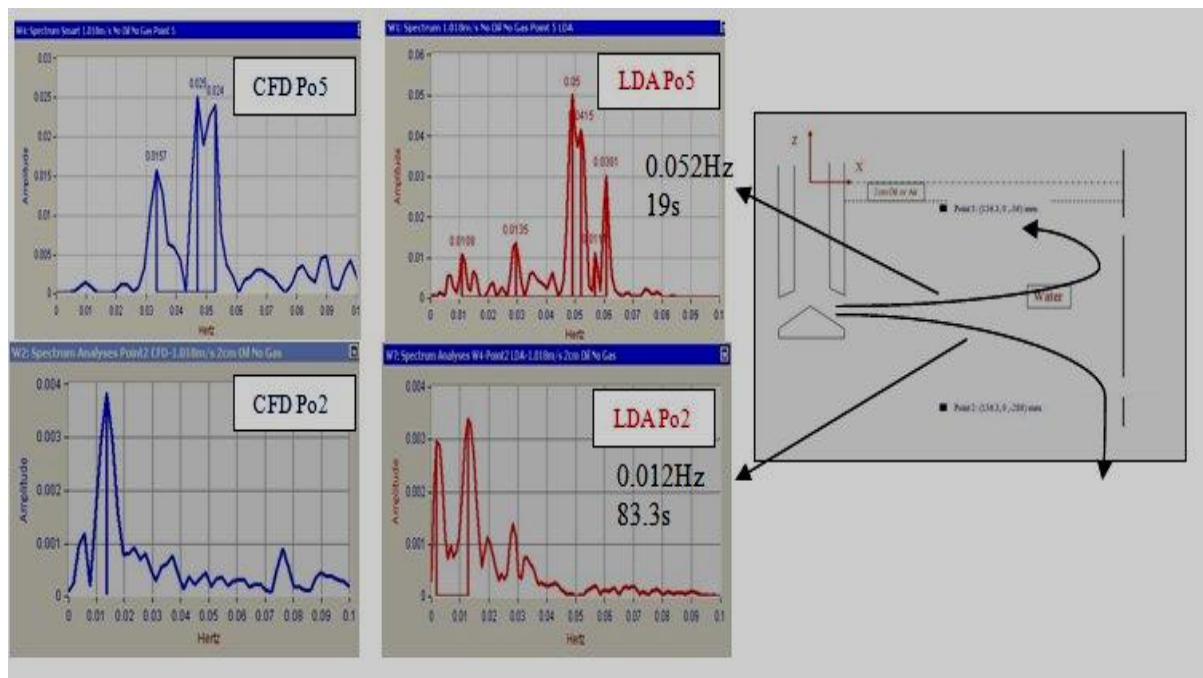


Figure 5.32: Experimental and numerical spectra for horizontal velocity components – 1.018m/s no Oil no gas, Point 5 and Point 2.

As already mentioned, small particles follow the flow, and therefore either the upper or the lower loop. For this reason they can be used as markers for investigating the total time taken for each particle to exit the domain either from the bottom outlet or through the top region.

Figure 5.33 shows four small particles which exit the port, moving with the jet. As expected [124], they split into two groups: one group enters the upper loop and is removed when it reaches the top surface. The other group follows the lower recirculation roll with its particles circulating in the lower region of the mould before exiting from the bottom of the domain. Despite the chaotic motion of the particles, the typical trajectories validate the periodic oscillation which is observed by spectrum analyses for both characteristic loops.

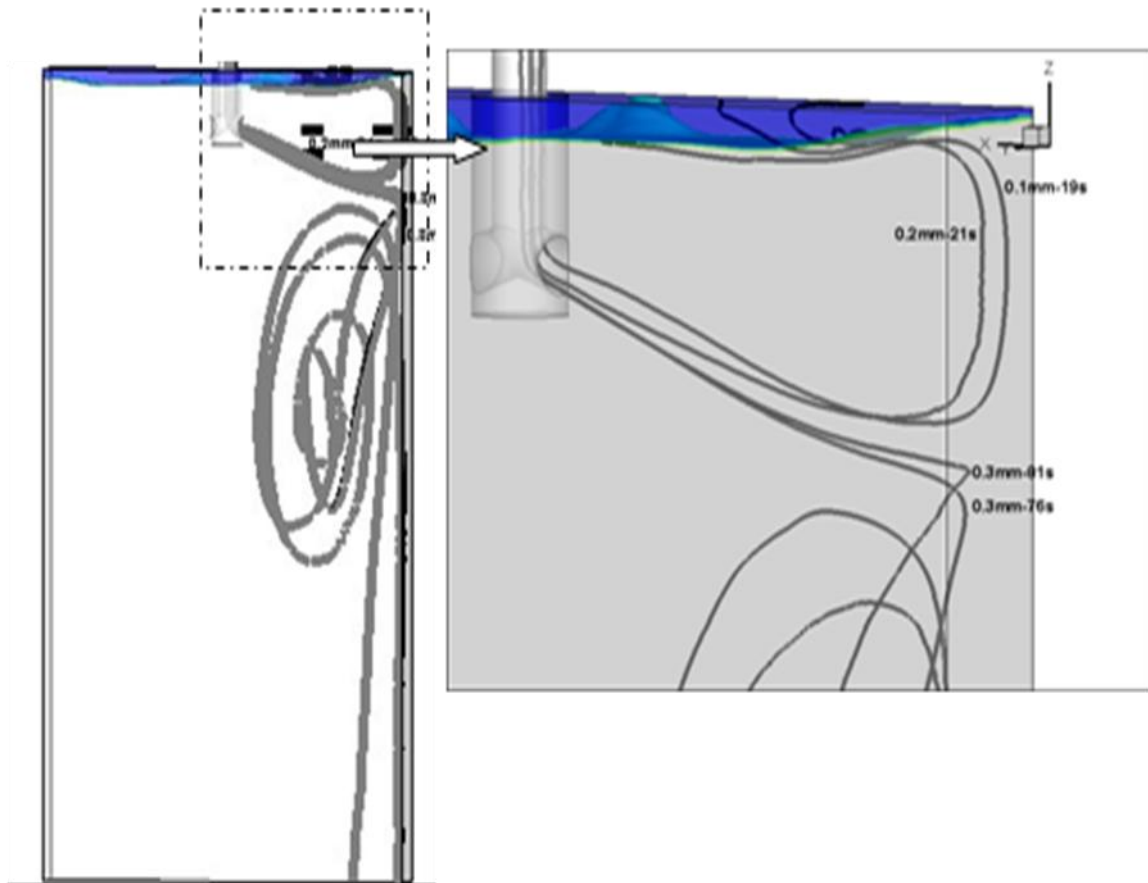


Figure 5.33: Four typical computed particle trajectories.

### 5.2.6.1 Influence of water flow rate in the meniscus stability

A spectrum analysis of the collected horizontal velocity data provides plausible explanations of the oscillation mechanism apparent during the continuous casting process. The observed frequencies characterize the periodic evolution of the horizontal velocity at the meniscus which seem to be directly related to the oscillating movement of the SEN jet, the size of its roll and the SEN casting velocity. Considering the magnitude of the spectral signal, the results validate the influence of oil and gas in the flow instability observed in qualitative

comparisons of experimental video and numerical visualization. For the first time, the calculation validates the flow oscillation prediction of experimental results providing a new insight in the hydrodynamic parameters which affect the transient behaviour of steel flow in the CC process.

It has already been observed that the behaviour of the upper loop oscillation depends on the water flow rate. In general, it is clearly detected by calculation and experiments that the periodic oscillation of this upper loop is close to 20-25s with an approximate period of 83s for the lower loop. Figure 5.34 represents the spectral analyses with the associated filtered signal for the case with air layer at the top of the mould for each inlet velocity. The first line, with the lower inlet velocity has a main peak observed at 0.035Hz (28.57s). Lines with inlet velocity of 0.8m/s and 1.018m.s have main peaks observed at 0.041Hz (24.4s) and 0.052Hz. The two latter frequencies are validated by numerical results as shown in Figure 5.35. In conclusion, experimental and numerical analyses of the results predicts an important increase in the frequency (smaller period) when the inlet velocity increases. In fact the strongest upper recirculation loop consists of a stronger signal, reducing the upper loop period.

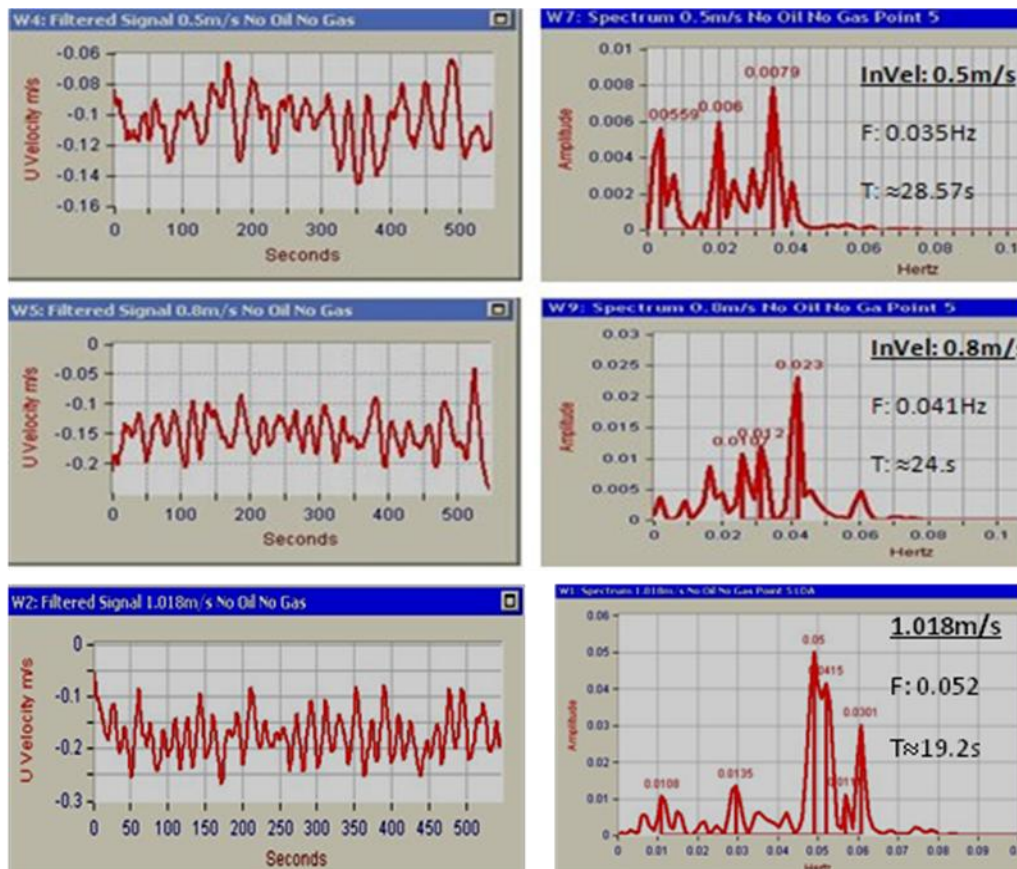


Figure 5.34: Influence of water flow rate, Spectrum Analyses comparisons with LDA data

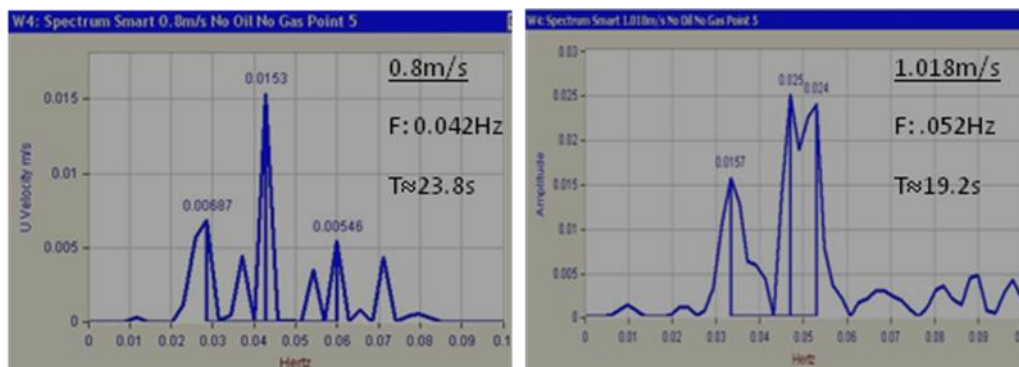


Figure 5.35: Influence of water flow rate, Spectrum Analyses-CFD results using SMART scheme.

### 5.2.6.2 Influence of oil and gas on the meniscus velocity

The influence of oil and gas injection is also investigated by spectral analysis shown in Figure 5.36 for points 4 which is near the interface using the case with an inlet velocity set at 0.8m/s. The left column shows the LDA signal filtered to remove high frequency noise, and the right column the signal spectrum. The presence of oil (2<sup>nd</sup> row) leads to a drastic reduction in the strong peak at 0.04Hz, and a significant reduction of the peak at 0.024Hz. Instead, a strong very low frequency oscillation appears at 0.05Hz. The addition of air further reduces the 0.024Hz peak.

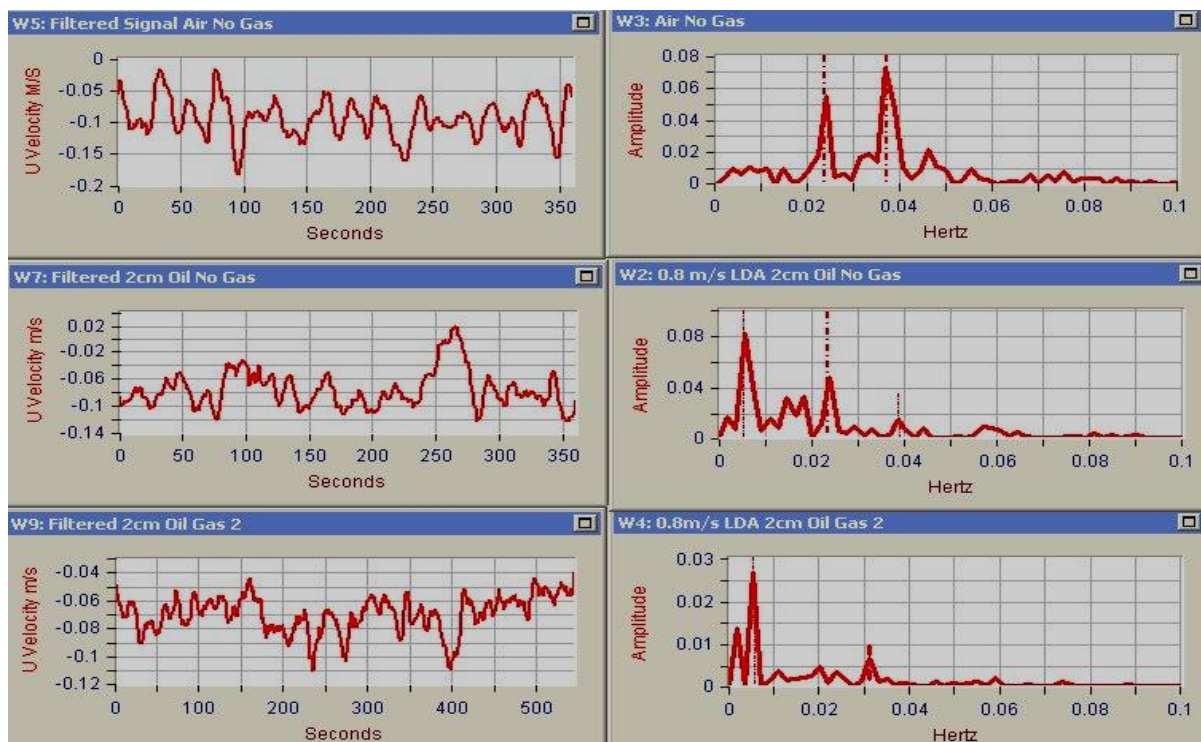


Figure 5.36: Influence of Oil and gas for point 4 –  $V_{in}=0.8\text{m/s}$ . The left column shows the filtered LDA signal and the right column the spectrum. The three rows correspond to: no oil layer, oil layer, oil+gas.

Experimental and numerical analyses tend to the same conclusion stating that most of the energy of fluctuation of the upper oscillation is stabilized by the oil. Furthermore, the top flow loop, which is responsible for the oil layer deformation, seems to be weakened when the gas enters with the steel. According to Figure 5.37, (note the scale of y axis is different) spectral analyses of numerical results display the affect of oil in the flow stabilization. The results show a weaker signal due to the active dynamic forces of oil, hence the oil is a vital parameter which can be of assistance to the flow stability. Additionally, it is obvious that quantitative results are linked to the qualitative examination and confirm flow pattern stabilization detected in the visual observation.

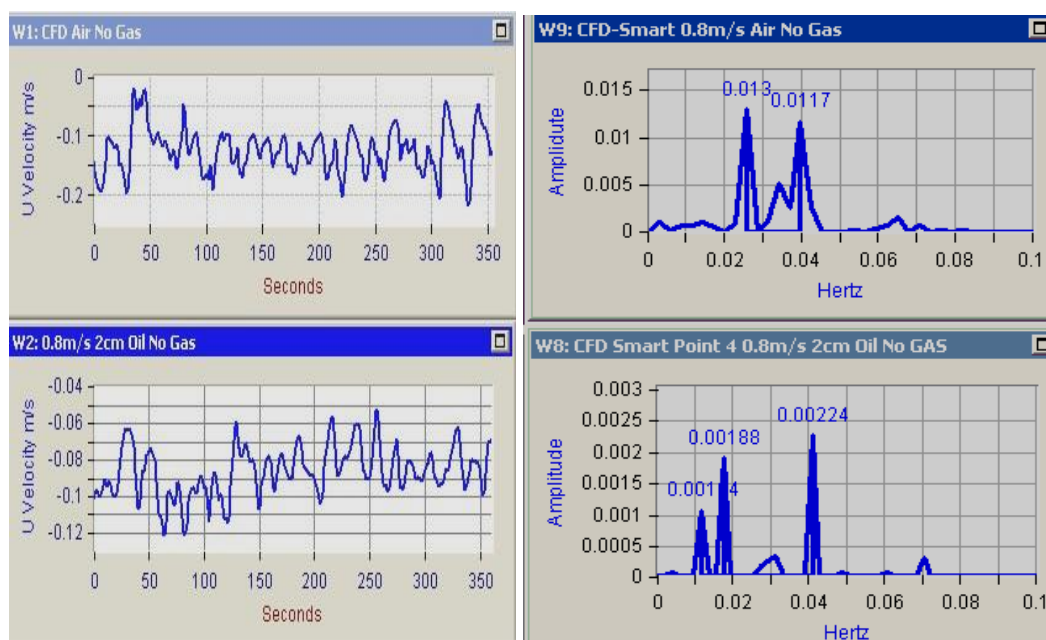


Figure 5.37: Influence of Oil for point 4 – CFD-Inlet Velocity 0.8m/s

Spectral analyses of both results predict a common peak close to 0.02Hz either with oil or air layer. The aforementioned frequency disappears when the gas flows through the SEN as depicted in Figure 5.36 for the LDA result. The frequency of 0.02Hz (50s) is suspected to characterise the jet oscillation which occurs during the process.

## ***Chapter VI***

### **6 Validation against Industrial Configuration**

The last chapter of this thesis concerns the validation of the model for coupled flow dynamics, heat transfer and solidification, in addition to steel/slag interface behaviour and argon buoyancy forces. The latter were shown to alter the flow pattern in the upper recirculation zone in the water model studies, which in turn affects the flux layer, superheat extraction and inclusion movement [69]. The study aims towards an understanding of the turbulent metal flow in the mould and its influence by the buoyancy forces of argon bubbles. This, of course, has as an effect on other related phenomena, such as the shell thickness, flux/slag and steel/slag interface behaviour.

Initially, the mathematical model developed and validated for the water model configuration is adapted for real caster simulation by appropriate alternative material properties and boundary conditions. This is coupled with the solution of heat transfer and solidification in the mould as described in Chapter 3. The main parametric study concerns flow modifications due to the effect of argon gas and the prediction of shell thickness. A final investigation aims at acquiring information on skin thickness using temperature-dependent material properties for flux powder and steel. The melting of powder and liquid slag depend on the thermal conductivity and the thickness of each layer. Viscosity is also indirectly involved as it affects the flow field within the molten flux layer. These parameters are therefore the main factors needed in order to perform an accurate computation of the heat transfer across the flux layer. Flux properties as a function of temperature are quite similar to those used by McDavid et al. [66] and steel properties correspond to those used by Ramirez and Meng et al. [125,65].

The various conditions tested and material properties for two cases studied are listed in Table 6.1.

PROPERTIES				
	Steel		Flux	
	Case1	Case2	Case1	Case2
Density(kg/m <sup>3</sup> )	7240	Appendix B	2500	2500
Viscosity(Kg/ms)	5.4E-3	Appendix B	0.09	Appendix B
ThermalConductivity(W/mK)	Appendix B	Appendix B	Appendix B	Appendix B
Specific heat(J/kgK)	822	Appendix B	2040	Appendix B
Liquidus temperature(°C)	1527.7	1527.7	1100	1100
Solidus Temperature(°C)	1495.1	1495.1	1000	1000
Latent heat(J/k)	263250	263250	500000	500000
CASTING CONDITIONS				
CASTING SPEED(m/min)	0.8m/min,1.6m/min			
Immersion Depth(mm)	120mm,160mm,200mm			
Tinlet(°C)	1600			
Interfacial Tension	1.4N/m			
Argon Flow Rate	7NL/min			

Table 6.1: Properties and casting conditions reported in two cases studied.

The numerical results have been validated against industrial caster measurements provided by AMR. The experimental operations, in a real caster, include measurements of surface velocity and depths of the powder/liquid plus the steel/flux interfaces using *Sub-meniscus Velocity Control* (SVC) and Nail Board, respectively [109]. The process includes an argon gas flow rate of 7NL/min and a thickness of the mould powder of about 7 cm. The liquid steel velocity measurements take place at the quarter of the mould width, in the middle plane for a period of 2 to 3 hours. The immersion of the refractory probe used for the velocity measurement in the liquid steel is around 2 cm. The nail board is made of two rows of 5 steel nails and 5 aluminum wires. Each row of nails is located 60 mm from the wide faces of the mould. The nail board is inserted in the top of the mould and is removed after 5 to 10s (quasi instantaneous measurement). The position of the interface between the liquid slag and mould powder is measured by the melting point of the aluminium nails, while the position of the steel/slag interface is measured by the

covered length of solidified steel on the nails. Additionally, the slope of the solidified steel indicates the flow direction.

### ***6.1 Assumptions and solution methodology***

The validation procedure consists of two tasks. The initial effort is the verification of the change that takes place in the steel velocity profile from a double roll to a single roll as the relative casting speed decreases. Hence, the initial computations include time-dependent metal flow coupled with metal/flux interface and particle tracks of argon. In addition, the model contains boundary condition for heat transfer from the mould to estimate the solidification of the steel shell. The latter is implemented via a user routine as a function of mould height (Appendix C). The argon gas is injected through the inlet of the nozzle, imposing a size distribution of the particles. The heat loss through the flux-slag layer is not considered at this step. Nevertheless, a slag layer of 70mm is added at the top of the mould in a liquid phase with a constant viscosity and thermal conductivity. The density and viscosity of steel is maintained constant for both liquid and solid states assuming that it behaves as an isotropic Newtonian fluid. However, the thermal conductivity and specific heat capacity of the steel are calculated as linear functions of temperature. The specific functions are the same as those used in previous studies [100, 126]. The solidified steel moves downwards at the casting speed and the effect of the mould oscillations is not considered.

Since solidification takes place at a much longer timescale than interface oscillation, a steady-state heat transfer equation is then solved so as to predict heat distribution and shell thickness, assuming a flat top surface covered by a protective flux layer. The thickness at the mould exit is then compared to previous experimental data and studies.

The second step investigates the influence of gas and immersion depth in the temperature distribution considering the thermal behaviour of the flux and slag layer. We determine the solid/liquid flux behaviour by the implementation of heat transfer analysis with adapted boundary conditions and properties for slag. The phase transformation of the powder to liquid or

to a re-solidified flux layer is calculated by its temperature-dependent properties such as viscosity, thermal conductivity and specific heat. A finer mesh is required in order to accurately capture the powder melting and steel solidification. As a result, the previous mesh is refined at the top of the mould and at the narrow faces. Furthermore, the density of steel depends on the temperature, in contrast to the assumption of constant density for steel which was used in the previous task.

## ***6.2 Metal flow in the mould and the effect of argon gas***

In order to reduce computation time, symmetry was used in this simulation with only half the mould thickness included in the computational domain. The numerical simulations are performed to compute a three-species flow, taking into account the liquid steel with the argon flow in the mould plus the flux layer of 7cm thickness at the top. The results of the transient computations are achieved using two different casting speeds and three different SEN immersion depths with 3.5 NI/min (because of the half geometry) gas flow rate for all numerical cases. The following figures show that the observed flow field verifies the plant measurements and agrees with reported findings of previous research [127, 128]. At a higher casting speed, the jet leaving the nozzle flows and reaches the mould's solidified wall impinging at the narrow face. In the case of the lower casting speed an upward movement of steel flow is observed due to the argon forces. The effect of argon in the metal flow is validated quantitatively and qualitatively by comparison with SVC measurements. In addition, the velocity distribution on the flux layer is verified qualitatively by the slope of the solidified steel nails in five locations.

Figure 6.1 shows the velocity measurements at the meniscus in the case of mould width of 1900mm and a gas flow rate of 7NI/min using real caster experiments. It corresponds to the interpolated velocity at the meniscus considering the mean value of immersion depths which is 160mm. The velocity measurements take place using immersion depths of 120mm and 200mm. However, according to the plant measurements, it can be stated, that for the casting speed value of 0.8m/min, a single roll is detected whatever the immersion depth. On the other hand, a casting speed of 1.6m/min generates a double-roll pattern.

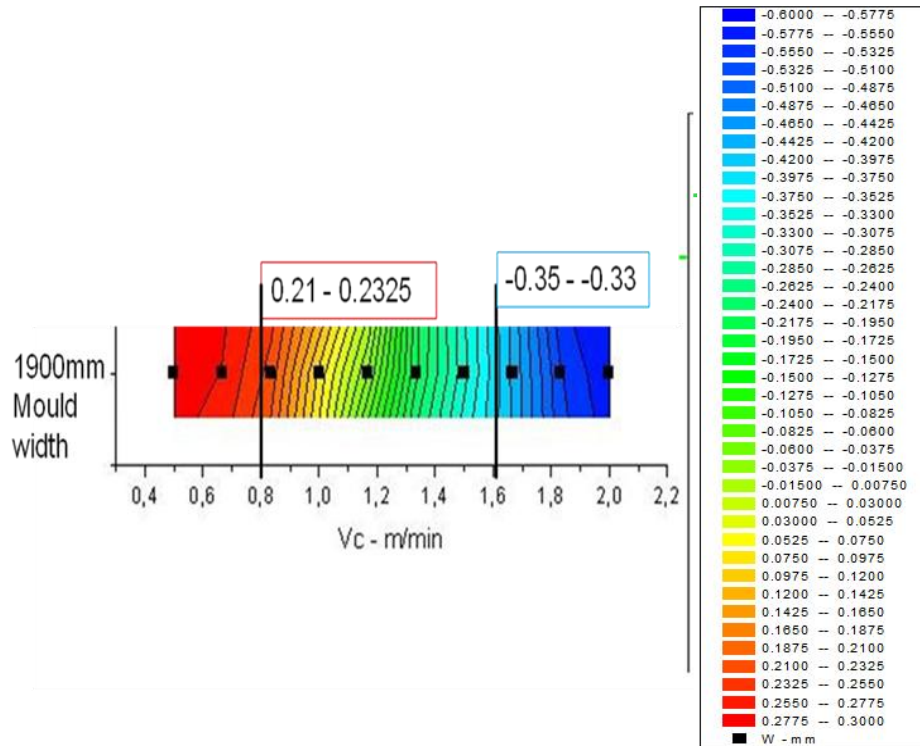


Figure 6.1: Interpolated velocity at the meniscus considering all immersion depths from industrial measurements.

Numerical simulation confirms the change of metal flow due to the gas flow rate. A casting speed of 0.8m/min generates a single roll while a casting speed of 1.6m/min produces the optimal double-roll flow pattern [127]. Figure 6.2 presents the numerical case with the immersion depth set at 120mm. In addition, the shell thickness and behaviour of argon flow are illustrated by the iso-surface of liquid and volume fraction respectively. The jet is weaker in the case of 0.8m/min casting velocity, creating an upward movement for steel flow as it is dominated by argon buoyancy. At the higher casting velocity the jet moves through the narrow faces with a small change in flow near the nozzle where a great concentration of argon exists. However, the steel flow separates in the narrow faces into the characteristic upper and lower loop. Moreover, the bubbles' spread and the corresponding gas volume rate increase as the casting velocity increases. Figure 6.3 illustrates the typical double and single roll patterns observed for the immersion depth set a 160mm. The same flow pattern is predicted as in the case of the immersion depth of 120mm. This figure shows the flow pattern by typical paths of velocity streamlines which form from the nozzle and the calculated heat distribution in the mould. Bigger variation is observed at the central of the mould with the heat distribution associated with the

steel flow. The higher casting speed tends to decrease the temperature in the center of the mould whilst the temperature between the meniscus and the narrow faces seems to decrease due to the lower flow pattern. However in case with lower casting speed, as expected, causes a bigger solidified shell (blue contour).

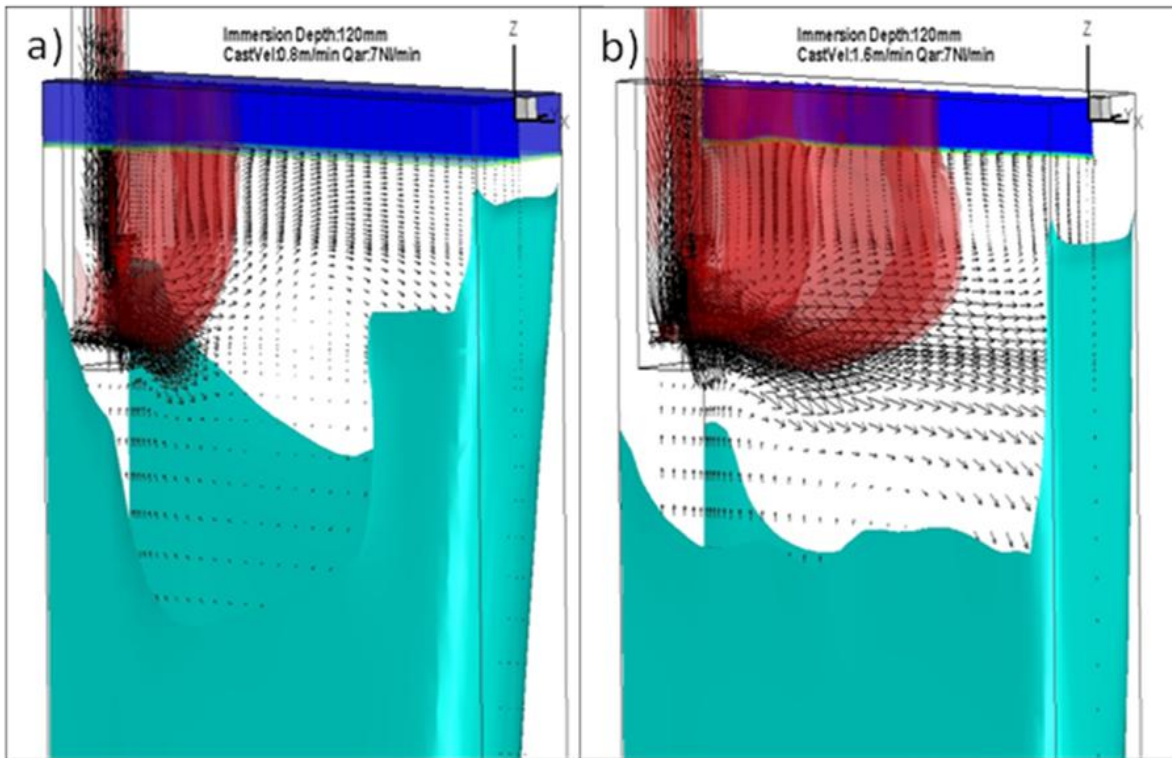


Figure 6.2: Flux surface with velocity vectors in the middle plane and contours of argon concentration, calculated and iso-surface of liquid fraction equal to 0.5. a) 0.8m/min, b) 1.6m/min.

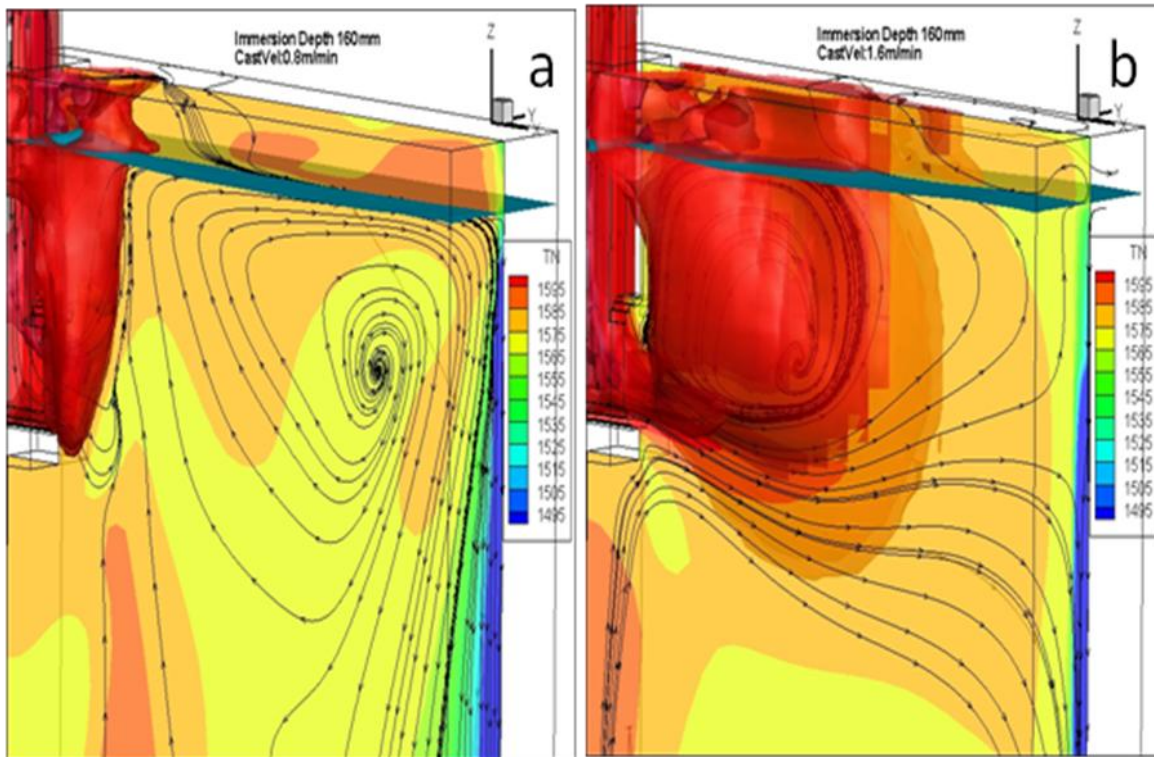


Figure 6.3: Flux surface with velocity streamlines from inside the nozzle in the middle plane, temperature distribution and argon concentrations contours. a) 0.8m/min, b) 1.6m/min.

Figure 6.4 and 6.5 depict the comparison between the velocity vector experiments in the meniscus, computed from the slope of the solidified steel nail, and the meniscus, horizontal velocity computed by the simulation. Qualitatively, the velocity field, 2cm under the slag/steel interface show the same trend between measurements and numerical results. These results suggest the single roll observed at the lower casting velocity dominates at this gas flow rate. On the other hand, in the case of the higher casting velocity, the argon gas spreads out with the jet which is strong enough to reach the narrow face, creating a double flow pattern.

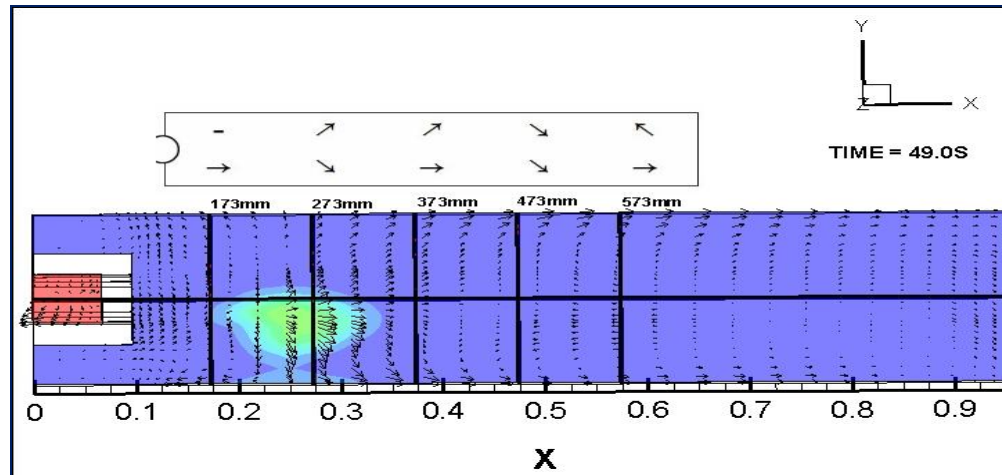


Figure 6.4: Comparison between Industrial velocity vectors (according to the slope of the solidified steel nails) and simulation vectors in the meniscus. 0.8m/min - Immersion Depth 160mm. Single roll is predicted.

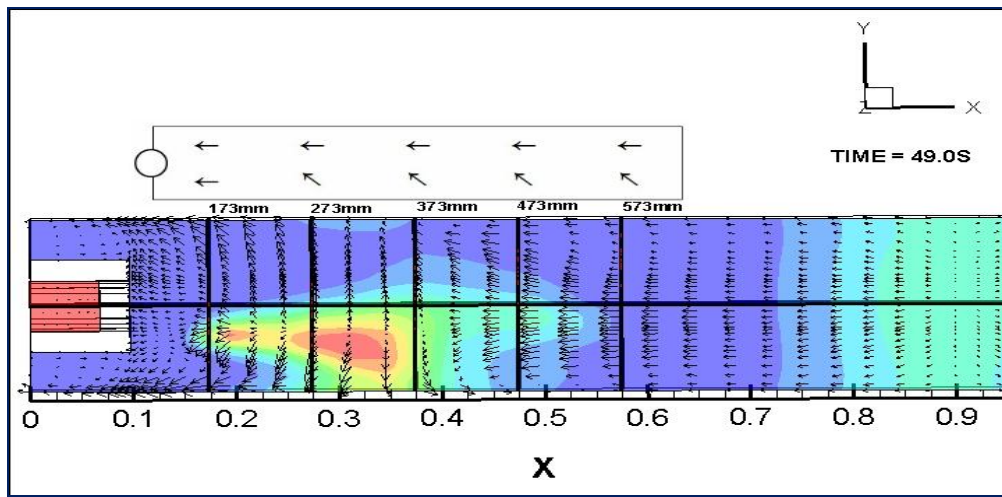


Figure 6.5: Comparison between Industrial velocity vectors (according to the slope of the solidified steel nails) and simulation vectors in the meniscus. 1.6m/min - Immersion Depth 160mm. Double roll is predicted.

Quantitative monitoring of the history of the horizontal velocity confirms the single roll pattern observed at the lower casting velocity, but it is in disagreement with the real caster measurement. The disagreement is depicted in Figure 6.6 which presents a comparison between the plant measurement (interpolated horizontal velocity at a mean value of immersion depth at 160mm as presented in Figure 6.1) and monitor history of the numerical results for the case with immersion depth set at 160mm with a 0.8m/min casting velocity (left single roll-positive values) and with 1.6m/min casting speed (right-double roll-negative values). The disagreement may be partially due to uncertainty as to the actual depth of metal below the slag layer and the actual bubble size

distribution. Although the data for bubbles distribution was not available, the use of reasonable values of bubbles distribution in the simulation yields the changes occurring in a real caster experiment due to the injected argon gas.

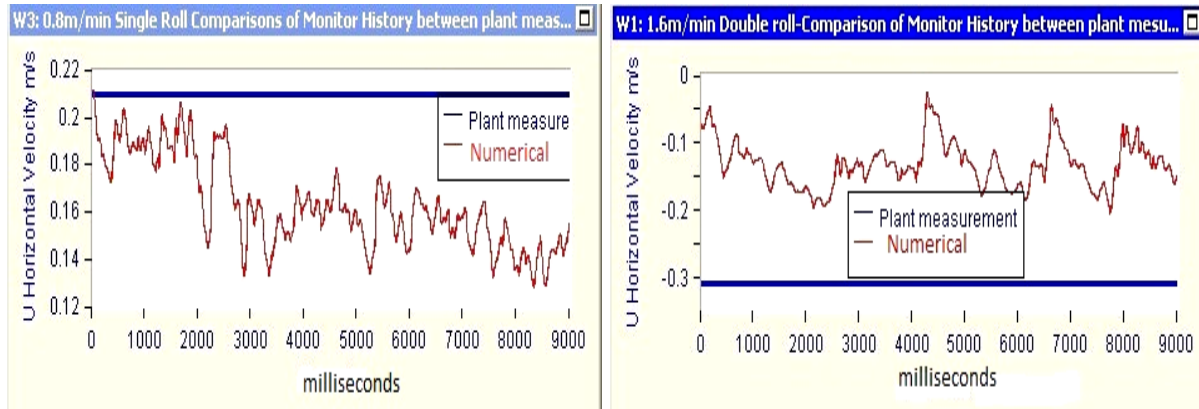


Figure 6.6: Comparison of the average horizontal velocity of plant measurement against numerical monitor history- Left:  $V_c$  0.8m/min , Right:  $V_c$  1.6m/min.

### 6.3 Influence of argon and immersion depth in the of shell thickness

A steady-state simulation is performed for the prediction of the shell thickness profile, since a considerable amount of time is required for heat transfer due to the heat capacity of steel. The three-dimensional turbulent calculations are performed assuming a flat steel/slag interface with temperature dependent properties as reported in appendix B. Despite the fact that the mould oscillation is not included in the model, the amount of solidification caused by convective heat transfer is basic in understanding the process. Figures 6.7 and 6.8 depict the heat distribution in the mould for immersion depths of 120mm and 160mm, respectively, and a constant velocity of 1.6m/min. These figures also show the shell thickness predicted at the narrow wall exit of the mould and the impingement point. A weaker flow at the top region of the mould can be observed for the case of the immersion depth set at 160mm in contrast to the case of the immersion depth set at 120mm. However, there is little influence of the immersion depth on the temperature profile in the mould. In general, the increase of the immersion depth seems not to affect the shell thickness at the mould exit while the shell profile at the impingement point is slightly higher due to the weaker flow created by the increase of the immersion depth.

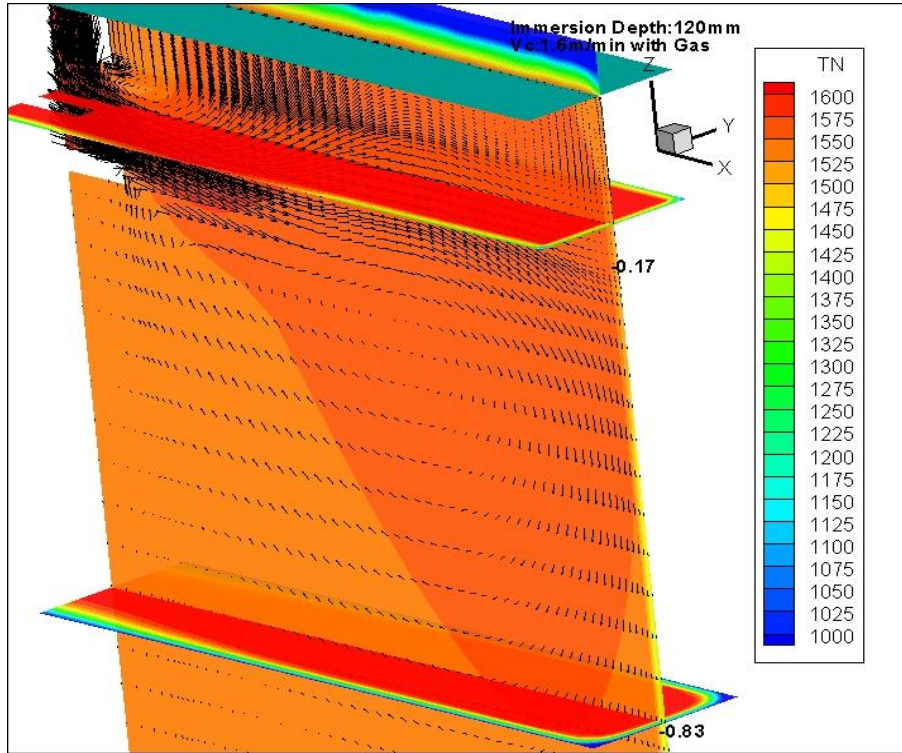


Figure 6.7: Temperature distribution with shell profile at the impingement point and the mould exit. Immersion depth set at 120mm with  $V_c=1.6\text{m/min}$ .

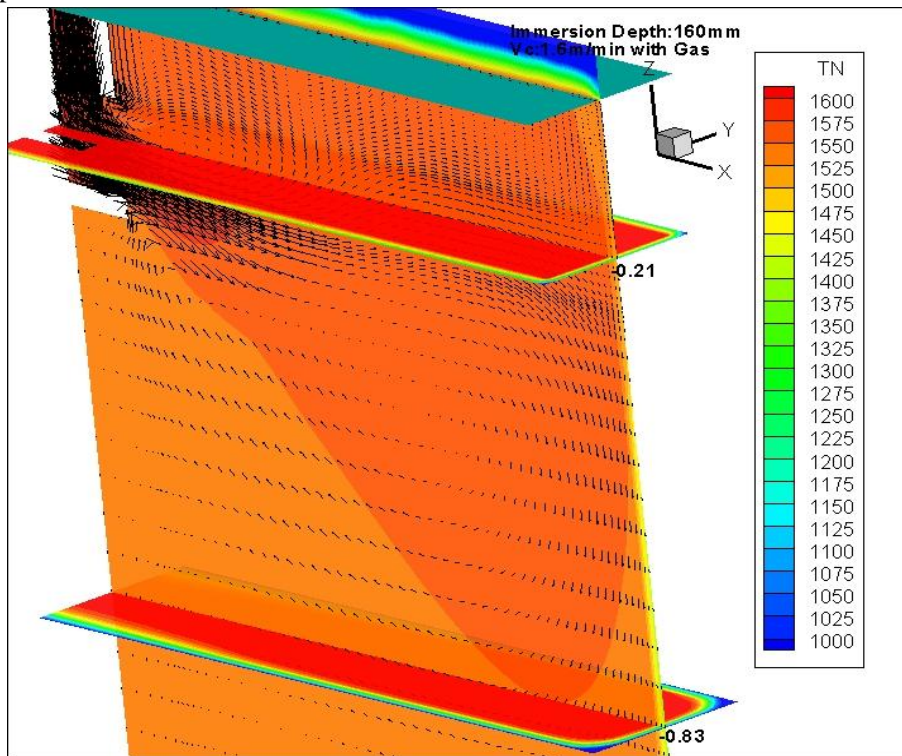


Figure 6.8: Temperature distribution with shell profile at the impingement point and the mould exit ( $Z=-0.83$ ). Immersion depth set at 160mm with  $V_c=1.6\text{m/min}$ .

In order to investigate the influence of gas on the shell thickness, the calculated data are also compared to the case with gas and without gas for a constant casting speed and immersion depth. The results show almost the same thickness profile at the mould exit, calculated at the narrow faces either with or without gas. In addition, slightly higher solidified steel in the area between the nozzle and the broad faces is observed, due to the weaker flow occurring when gas is injected through the nozzle. These observations are depicted at the top of Figure 6.9 with a combination plot showing the solid-liquid flux interface, contours of liquid fraction (and argon volume fraction in the right plot) and velocity streamlines which form inside the nozzle. The figure confirms the influence of gas in the top recirculation loop and its effect on the shell thickness. The main difference is observed in the velocities at the meniscus close to the narrow face which the temperature is lower in case with gas which may cause a freezing meniscus.

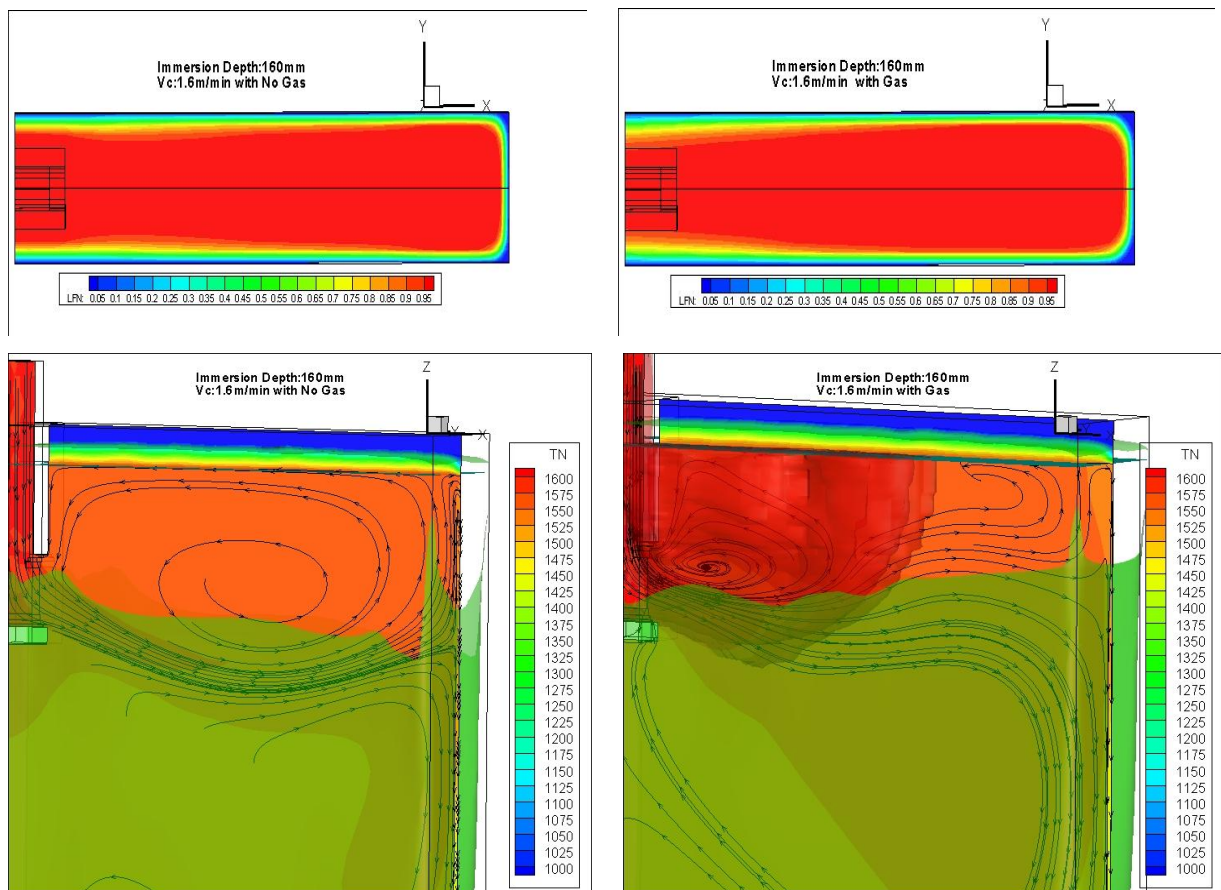


Figure 6.9: Influence of gas on the shell thickness at the mould exit (top), the flow pattern and in the temperature distribution within the mould. Left figures present the results without gas while the right figures are with argon gas.

### 6.3.1 Validation of shell thickness

The shell thickness (Figure 6.10) is calculated as the average distance between the narrow wall and the region where the liquid fraction is 0.5 at the copper mould exit. The predicted thicknesses (29mm and 8mm) are in agreement with available data from previous works [65, 89, 129, 130]. The discrepancy in the shell thickness, mainly in the case of the higher casting velocity, may be caused by uncertainty in the thermal boundary conditions, or the temperature-dependent properties used for powder. It is also important to examine the transient behaviour of the slag layer deformation by the steel flow and the infiltration of the molten flux into the steel-mould interface [133,134]. The behaviour of this layer has a very important role to play in the efficiency of the process, since it affects several defects [135]. A further extension of the model is required to address these key issues, in order to correctly represent the heat transfer evolution of the process, which is a challenging subject for future work.

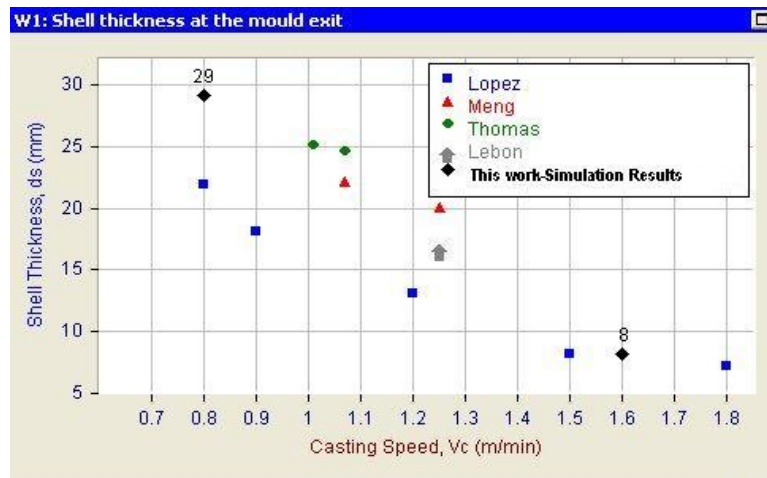


Figure 6.10: Validation of shell thickness profile in the mould exit with previous work from Ramirez-Lopez et al [129] Meng et al [65], Thomas et al [130] and Bruno [89].

However, the model as it stands reflects, with reasonable accuracy, observations from both a water model and a real caster and gives a true representation of the phenomena observed in the experiments. A number of important conclusions and recommendations regarding the CC operation will be addressed in the next Chapter.

## *Chapter VII*

### **7 Conclusions and Further Work**

#### **7.1 Conclusions**

A mathematical model was developed in order to enhance the understanding of the physics involved in the Continuous Casting process. The model highlights the unsteady nature of the steel/slag interface and in particular the influence of gas bubbles on the flow behaviour. Consequently, a three-phase transient simulation was considered, making use of the multi-physics finite volume code PHYSICA with special emphasis on free surface characterisation and gas-liquid coupling. The multiphase model includes an implicit interface tracking scheme using the Counter Diffusion Method (*CDM*) and a Lagrangian particle tracking method to describe the gas behaviour treated as discrete bubbles. It is important to note that numerical diffusion and artificial damping of the interface posed problems in this research and were overcome by activating a second-order bounded numerical scheme coupled with the standard k- $\epsilon$  model, as opposed to the first-order Hybrid (Upwind-Central) scheme.

The model has been validated by means of water model experiments with velocity measurements obtained using the LDA technique by AMR. Both experimental and numerical methods provide a physical explanation for the dynamic behaviour of the slag layer and identify the parameters which aid the flow stabilization. Qualitative evaluation of the results against water model visualizations explains the main flow patterns observed, and verifies the predicted deformation of the meniscus. Quantitative comparisons are provided against LDA velocity measurements at seven measurement positions. Simulations of various process parameters agree very well with the experiments and lead to several suggestions which are of value to the industrial continuous casting process.

For the first time, the nature of flow oscillations of the lower and upper recirculation loops during the continuous casting process is explained by comparing frequency spectral patterns with observed flow features, in particular the turnover time of the main recirculation loops and the flapping motion of the two SEN jets.

The mathematical model was also applied to the simulation of an actual industrial caster with the addition of heat transfer and solidification. The latter investigation predicts the influence of injected argon gas where velocity measurements and simulation show a fundamental switch in the steel flow pattern. The model has determined the solid shell thickness profile as it emerges from the mould and numerical predictions compare favourably with shell thickness predictions from previous studies in the literature.

The last case presented aimed to characterise the phase transformation of the powder to liquid and then to the re-solidified flux layer on the mould walls. Despite the assumptions used, the model gives a reasonable prediction of the flow pattern in the meniscus together with the mould and slag layer thickness in accord with available experiments results provided by AMR. However, in order to attain a more accurate knowledge of the heat transfer across the slag layer, the deformation of the slag layer due to the steel flow and the effect of argon bubbles through the flux layer must be taken into account.

Considering the results presented in this thesis the following conclusions and suggestions can be applied to the industrial Continuous Casting process:

### **Conclusions for water model configuration**

- The purpose of the multi-phase mathematical model was to simulate the transient turbulent flow pattern, coupled with free surface and particle tracking either in a water model or for a real industrial configuration. It was observed that the second-order accurate scheme SMART, without any modification of the turbulent k- $\epsilon$  model, provides good qualitative and quantitative agreement with experiments. Initial studies suggested the adoption of a filtered k- $\epsilon$  model would be necessary.

- The mathematical model is capable of accurately describing experimental observations: the turbulent steel flow, the free surface shape with and without gas, the mean value, standard deviation and fluctuating velocity spectra. Two contributors to velocity fluctuation should be considered for standard deviation calculations; one from the resolved low frequency oscillation and the other from turbulence [101].
- Both experimental and numerical results suggest that gas and the presence of oil stabilize the flow. The SEN jet develops into two recirculation loops with the upper loop slowed down by the bubbles. Furthermore a 2cm oil layer representing slag leads to a wavy oil water interface that becomes very disturbed at higher velocity; the oil is pushed towards the centre of the section, exposing the water (steel) surface to the air.
- Numerical results indicate that the presence of oil tends to decrease the mean value and the fluctuation amplitude of the horizontal velocity at the meniscus except in the case of the lowest inlet velocity (0.5m/s). Gas injection tends to reduce the standard deviation of the horizontal velocity component and affects the upper loop from the SEN to the narrow faces. Visualization of numerical results and experimental videos illustrate that the gas affects the upper loop from the SEN to the narrow face which perhaps can be profitable for the flow stability.
- Spectral analysis of the numerical and experimental data seems to indicate that the dominant frequencies relate to the turnaround time of the two recirculation loops. The upper and lower loops are characterized by frequency oscillations close to 0.012Hz and 0.05 Hz respectively. In general, the results predict a small increase in the frequency (smaller period) and a stronger signal when the inlet velocity increases.
- Spectral analysis prediction confirms the stabilization of flow due to the presence of the oil at the top of the mould and the buoyancy forces of bubbles. Experimental and numerical trends illustrate that the energy of the lower frequency oscillations related to the upper loop (0.05Hz) is reduced due to the viscosity of the oil, and the resulting

oscillations seem to be eliminated when the gas flows. The latter leads to the conclusion that gas has more stabilizing effect than the oil layer.

### **Conclusion for the industrial model configuration**

- The model predicts the transient turbulent flow behaviour and accurately reflects plant observations on the influence of gas buoyancy forces in the metal flow pattern. The numerical results illustrate a single roll pattern in the lower casting velocity (0.8m/min) and the expected double roll pattern in the higher casting velocity (1.6m/min) due to the increasing presence of buoyancy forces. The model identifies the buoyancy influence of the bubble plume as critical in determining this behaviour.
- Quantitative velocity comparisons between experiment and simulation show similar trends although actual velocity values differ. There is some uncertainty related to the depth of the measurement probe immersion and the actual bubbles size distribution which may explain the differences.
- Three-dimensional steady-state calculations coupled with fluid flow and heat transfer enable shell thickness predictions, which compare favourably with values available in the literature and validate the slag thickness profile from experimental data provided by AMR.
- As expected, the shell thickness decreases with the increase in casting speed. Moreover the bubbles' spread and the corresponding gas volume rate increase as the casting velocity increases. As mentioned above, the prediction of the shell thickness compares favourably with previous results and the influence of gas in the flow pattern is in good agreement with real caster experiments performed by AMR.
- The injected argon gas creates a weaker upper recirculation flow which leads to a thinner shell at the top of mould. However, the solidified steel in the mould exit is the same either with gas or without. The height of the immersion depth is also considered as a parameter which affects the flow pattern, hence the steel thickness profile. It can be stated that the

solidified steel thickness, in the top region of the mould, clearly increases with the increase in the immersion depth, but there is no change in the solidified steel thickness at the mould exit.

## **7.2 Further work**

There are many aspects of the CC process where improvements can be introduced, to the present model. For example, in recent years, the mathematical aspect of several studies [131,132] in CC has had to do with the effects of the magnetic field and gas and their influence in meniscus stability. However, further work is needed for the enhancement of our understanding in the related influence of the magnetic field in the flow pattern coupled with the bubble and meniscus steel/slag interface. Since the bubbles are electrically non-conducting, additional electromagnetic forces will act on them changing their distribution. In addition, the solid (or powder) fraction of the slag and its interaction with the gas bubbles may be linked to chemical reaction and heat transfer, since both affect the viscosity of the flux. Argon bubbles carry heat energy through the steel in their wake and dissipate it to the surroundings as they go through the flux/powder layer. Furthermore, and perhaps a more ambitious extension of the model would include the thermo-mechanical behaviour of the solidifying strand and its interaction with the meniscus. Recent investigations have considered the mould oscillation in order to enhance the physics involved in the lubrication mechanism and friction behaviour between the mould and the solidified shell [137]. This vertical-direction of friction between the mould wall and the solidified steel (shell) [138, 139] affects the quality of the slab, since it controls the formation of defects such as cracks and breakouts. Such a model requires to be coupled with the liquid-solid phase transformation, the stress generation inside the mould and the crack formation in the continuous casting of steel [140, 141]. Despite the considerable progress in the thermo-mechanical analysis of casting, an integral numerical model, which will combine all these complex phenomena, is still a challenging subject nowadays [142].

One of the main difficulties in carrying out these runs has been the very long computation times required by transient simulations. Code parallelisation for operation on multi-processor clusters is a future development that would make routine use of the model by industry possible. At

present, although the code PHYSICA can operate in parallel, the Lagrangian implementation of the gas field can only run in scalar mode.

## REFERENCES

1. PHYSICA code, *the University of Greenwich*, URL: <http://physica.co.uk/>.
2. B. van Leer, "Towards the Ultimate Conservation Difference Scheme IV, A New Approach to Numerical Convection," *Journal of Computational Physics*, 23:pp. 276-299, 1977.
3. J. D. Ramshaw and J. A. Trapp, "A Numerical Technique For Low Speed Homogeneous Two Phase Flow with a Sharp Interface", *Journal of Computational Physics*, 21:pp. 438-453, 1976.
4. C. W. Hirt and B. D. Nichols, "Volume of Fluid (VOF) Method For The Dynamics of Free Boundaries", *Journal of Computational Physics* 39, pp. 201-225 1981.
5. K. Pericleous, G. Djambazov, B. Lebon, T. N Croft, J. F. Domgin, P. Gardin, "Time-dependent modeling and experimental validation of the metal/flux interface in a continuous casting mould", *Revue De Metallurgie Cahiers D Informations Techniques* 2008, Vol.105, pp. 33-43.
6. J.H. Welch, *J. Sci. Instrm.*, 31 (1954), pp. 458.
7. J. Savage and W.H. Pritchard, "The problem of rupture of the billet in the continuous casting of steel", *J. Iron Steel Inst.*, Vol. 178, 1954, pp. 269-277.
8. E.A. Mizikar, "Mathematical Heat Transfer Model for Solidification of Continuously Cast Steel Slab", *Trans. TMS-AIME*, Vol. 239, 1967, pp.1747-1753.
9. Wikipedia web address, URL: [http://en.wikipedia.org/wiki/Continuous\\_Casting](http://en.wikipedia.org/wiki/Continuous_Casting).
10. S. T. Johansen, J. Wu, W. Shyy, "Filter Based unsteady RANS computation", *International Journal of Heat and Fluid Flow* 25 (2004) pp.10-21.
11. P. H. Gaskell and A. K. C. Lau, "Curvature-Compensated Convective Transport: SMART, A New Boundedness Preserving Transport Algorithm", *International Journal for Numerical Methods in Fluids*, 8, pp.617-641 (1988).
12. Web address: [Continuous casting section at steeluniversity.org, including fully interactive simulation](#).
13. K. C. Mills, A. B. Fox, R. P. Thackray, Z. Li, "The Performance and Properties of the Mould Fluxes", *Ironmaking & steelmaking* 2005, vol. 32, n°1 pp. 26-34.

14. B.G. Thomas, "Continuous Casting", *The Encyclopedia of Materials: Science and Technology*, Elsevier Science Ltd., Oxford, UK, Vol. 2, 2001, pp. 1595-1599.
15. HARPOON web address, URL: <http://www.sharc.co.uk/>
16. Fluent web address, URL [www.fluent.com/software/gambit](http://www.fluent.com/software/gambit).
17. H. Wang, G. LI, Y. LEI, Y. Zhao, Q. Dai and J. Wang, "Mathematical Heat Transfer Model Research for the Improvement of Continuous Casting Slab Temperature", *ISIJ International*, Vol.45 (2005) No.9 pp.1291-1296.
18. M. Long, L. Zhang and F. Lu, "A Simple Model to Calculate Dendrite Growth Rate during Steel Continuous Casting Process", *ISIJ International*, Vol. 50 (2010) No. 12 pp.1792-1796.
19. C. A. Santos, J. A. Spim and A. Garcia, "Mathematical modeling and optimization strategies (genetic algorithm and knowledge base) applied to the continuous casting of steel", *Engineering Applications of Artificial Intelligence*, Volume 16, Issues 5-6, August-September 2003, Pages 511-527.
20. Q. Yuan, S. Sivaramakrishnan, S.P. Vanka and B.G Thomas, "Computational and Experimental Study of Turbulent Flow in a 0.4-Scale Water Model of a Continuous Steel Caster", *Metallurgical and Materials Transactions B*, Vol. 35B, No. 5, Oct., 2004, pp. 967-982.
21. Y. Kwon, J. Zhang and H. Lee, "Water Model and CFD Studies of Bubble Dispersion and Inclusions Removal in Continuous Casting Mold of Steel", *ISIJ International*, Vol. 46 (2006) No. 2 pp.257-266.
22. B. LI and F. Tsukihashi, "Vortexing Flow Patterns in a Water Model of Slab Continuous Casting Mold", *ISIJ International*, Vol. 45 (2005) No.1 pp.30-36.
23. E. Brandaleze, L. Castella and E. Benavidez, "The influence of Mould Powder Properties on Heat Transfer In Continuous Casting", *ECCS 2005*, ATS-RM pp.645-647.
24. K. Watanabe, K. Tsutsumi, M. Suzuki, M. Nakada and T. Shiomi, "Effect of Properties of Mold Powder Entrapped into Molten Steel in a Continuous Casting Process", *ISIJ International*, Vol. 49 (2009) No. 8 pp.1161-1166.
25. L. Zhang, J. Aoki and B.G. Thomas, "Inclusion Removal by Bubble Flotation in Continuous Casting Mold", *Materials Science & Technology*, 2004 (MS&T2004), Sep. 26-29, 2004, New Orleans, LA, Vol. II, pp. 161-177.

26. M. Wu, A. Ludwig and C. Pfeiler, "Influence of argon gas bubbles and non-metallic inclusions on the flow behaviour in steel continuous casting", *Materials science & engineering. A, Structure materials*, 2005. Volumes 413-414, pp 115-120.
27. M. Cross, T. N. Croft, G. Djambazov, K. Pericleous, "Computation modeling of bubbles, Droplets and particles in metals reduction and refining", *Applied Mathematical Modelling*, 30 (2006), Page. 1445-1458.
28. O. Putz and S. Rodl "Investigation of Unsteady and Asymmetric Flow Phenomena in Continuous Casting Moulds by Advanced Simulation Techniques" *Steel Research International* 2003, vol. 74, n<sup>o</sup>2, pp. 104-113.
29. B.G. Thomas, Q. Yuan, B. Zhao and S.P. Vanka, "Transient Fluid-Flow Phenomena in the Continuous Steel-Slab Casting Mold and Defect Formation" *JOMe, (Journal of Metals – electronic edition)*, December, 2006.
30. Q. Yuan, B. Zhao, S.P. Vanka and B.G. Thomas "Study of Computational Issues in Simulation of Transient Flow in Continuous Casting", *Steel Research International, Special Issue: Simulation of Fluid Flow in Metallurgy*, Jan. 2005, Vol. 76, No. 1, pp. 33-43.
31. K. Fujisaki, "3-D MHD Calculation in Consideration of Free Surface, Heat Transfer and Solidification", *International Journal of Applied Electromagnetics and Mechanics* Vol. 14, 2002 pp. 9-14.
32. Mizukami, M. Kamatsu, T. Kitagawa and K. Kawakami, "Effect of Electromagnetic Stirring at the Final Stage of Solidification of Continuously Cast Strand", *Tetsu-to-Hagane*, 70 (1984) No 2 pp. 194
33. F. Chang, J. Hull and L. Beitelman "Simulation of flow control in the meniscus of a continuous casting mold with opposing alternating current magnetic fields", *Metallurgical and Materials Transactions B* Vol. 35, Number 6 December 2004. pp. 1129-1137.
34. K. Takatani, "Effects of electromagnetic brake and meniscus electromagnetic stirrer on transient molten steel flow at meniscus in a continuous casting mold", *ISIJ-International*. 43, (2003) 915-922.
35. T. Takehiko, E. Takeuchi and K. Yamamura "Multi-physics Analysis for Electromagnetic Processing In Continuous Casting of Steel by Finite Volume Method Approach", *Seventh International Conference on CFD in the Minerals and Process Industries* CSIRO, Melbourne, Australia 9-11 December 2009.

36. K. Cukierki and B. Thomas, "Flow Control with Local Electromagnetic Braking in Continuous Casting of Steel Slabs", *The Minerals, Metals & Materials Society and ASM International* 2007 Vol. 39B, Feb 2008 –pp. 94-107.
37. B.G. Thomas, "Continuous Casting: Complex Models", *The Encyclopedia of Materials: Science and Technology*, Elsevier Science Ltd., Oxford, UK, Vol. 2, 2001, pp. 1599-1609.
38. L. Zhang, "Fluid Flow and Inclusion Removal in Molten Steel Continuous Casting Strands", *Fifth International Conference on CFD in the Process Industries*, CSIRO, Melbourne, Australia, 13-15 December 2006.
39. Z. Xing-guo, Z. Wen-xiao, J. Jun-ze, J.W. Evans, "Flow of Steel in Mold Region During Continuous Casting" *Journal Of Iron and Steel Research, International* 2007,14(2)-Page 10-35.
40. H. Bai and B.G. Thomas, "Turbulent Flow of Liquid Steel and Argon Bubbles In Slide-Gate Tundish Nozzles: Part I. Model Development and Validation", *Metallurgical and Materials Transactions B* Vol 32B, April 2001-Page 253-267.
41. M. Meratian and A. Hadjari, "Physical Modeling of Steel Delivery during Thin Slab Continuous Casting" *International Journal of ISSI*, Vol.5 (2008), No. 1, pp. 41-46.
42. F.M. Najjar, B.G. Thomas and D. Hershey, "Numerical Study of Steady Turbulent Flow through Bifurcated Nozzles in Continuous Casting" *Metallurgical Transactions B.*, Vol. 26B, No. 4, 1995, pp. 749-765.
43. H. Bai and B.G. Thomas, "Turbulent Flow of Liquid Steel and Argon Bubbles in Slide-Gate Tundish Nozzles, Part II, Effect of Operation Conditions and Nozzle Design", *Metallurgical and Materials Transactions B*, 2001, Vol. 32B, No. 2, pp. 269-284.
44. J. Anagnostopoulos and G. Bergeles "Three-Dimensional Modeling of the Flow and the Interface Surface in a Continuous Casting Mold Model", *Metallurgical and Materials Transactions B* Vol. 30B, December 1999-Page 1095-1103.
45. P. Ramirez-Lopez, R. D. Morales, R. Sanches-Perez, L. G. Demedices "Structure of Turbulent in a Slab Mold" *Metallurgical and Materials Transactions B* Vol. 36B, December 2005-Page 787-799.
46. B. G. Thomas, Q. Yuan, S. Sivaramakrishnan, T. Shi, S. P. Vanka, and M. B. Assar "Comparison of Four Methods to Evaluate Fluid Velocities in a Continuous Slab Casting Mold" *ISIJ International* 2001, Vol.41, No 10, pp, 1262-1271.

47. P. Gardin, M. Brunet, J. F. Domgin, K. Pericleous “An experimental and Numerical CFD Study of Turbulence in a Tundish container” *Second International Conference on CFD in the Minerals and Process Industries* 1999.
48. B. Wiwatanapataphee, Y. H. Wu, J. Archapitak, P. F. Siew, B. Unyong “A Numerical Study of the Turbulence Flow of Molten Steel in a Domain With a Phase-change boundary” *Journal of Computation and Applied Mathematics* 166(2004) 307-319.
49. M. Brummayer, P. Gittler, J. Watzinger, “Stabilization of unsteady in the mold region of a wide slab caster by submerged entry nozzle design optimization with CFD”, *Second International Conference on CFD in The Minerals and Process Industries*, CSIRO, Melbourne, 6-8 December 1999, Australia.
50. Q. Yuan, S.P. Vanka and Brian G. Thomas, “Large Eddy Simulations of Transient Flow during Continuous Slab Casting of Steel”, *3rd International Symposium on Turbulence and Shear Flow Phenomena*, Sendai, Japan, 25-27 June, 2003, Conference Proceedings, Vol. 2, pp.681-686, 2003.
51. C. T. Shaw *Using Computational Fluid Dynamics*.
52. T. N. Croft, K. A. Pericleous, M. Bobadilal, P. Gardin, “Three-phase Computation of the Continuous Casting Process”, 4<sup>th</sup> European Continuous Casting Conference, 2002.
53. B. G. Thomas and F. P. Najjar “Finite element modelling of turbulent fluid flow and heat transfer in continuous casting” *Appl. Math. Modelling*, May 1991, Vol. 15.
54. B. G. Thomas, L .J. Mika, F. M. Najjar, “Simulation of Fluid Flow Inside a Continuous Slab-Casting Machine”, *Metallurgical and Materials Transactions B* Vol. 21B, April 1990 pp. 387-400.
55. B.G. Thomas, R. O'Malley, T. Shi, Y. Meng, D. Creech, and D. Stone, “Validation of Fluid Flow and Solidification Simulation of a Continuous Thin Slab Caster, Modeling of Casting, Welding, and Advanced Solidification Processes- IX”, Aachen, Germany, August 20-25, 2000, pp. 769-776.
56. S. Sivaramakrishnan, B.G. Thomas, and S.P. Vanka, “Large Eddy Simulation of Turbulent Flow in Continuous Casting of Steel”, *Materials Processing in the Computer Age III*, V. Voller and H. Henein, eds., TMS Annual Meeting, Nashville, TN, March 12-16, 2000, pp. 189-198.
57. Yuan, Q, S.P. Vanka, and B.G.Thomas, “Large Eddy Simulations of Turbulent Flow and Inclusion Transport in Continuous Casting of Steel”, *Proceedings of 2nd International*

- Symposium on Turbulent and Shear Flow Phenomena, Vol. 2, Royal Institute of Technology (KTH), Stockholm, Sweden, June 27 - 29, 2001, pp. 519-524.
58. B. G. Thomas, R. O'Malley, T. Shi, Y. Meng, D. Creech, and D. Stone, "Validation of Fluid Flow and Solidification Simulation of a Continuous Thin Slab Caster", Modeling of Casting, Welding, and Advanced Solidification Processes - IX, Aachen, Germany, August 20-25, 2000, P. Sahm, ed., Shaker Verlag GmbH, Aachen, Germany, 2000, pp. 769-776.
59. B. G. Thomas, "Modelling Of the Continuous Casting of Steel-Past, Present and Future", 59<sup>th</sup> Electric Furnace Conference., Phoenix, AZ, 2001, Iron & Steel Soc. pp.3-30.
60. B. G. Thomas "Continuous Casting of Steel" Chapter 15 in Modelling for Casting and Solidification Processing, O. Yu, editor, Marcel Dekker, New York, NY, 2001, pp. 499-540.
61. B. Zhao, S. P. Vanka, and B. Thomas, "Numerical Study of Flow and Heat Transfer in a Molten Flux Layer", *Int. J. Heat and Fluid Flow*, 2005, Vol. 26, No. 1, pp 105-118.
62. R. Saraswat, D. M. Maijer, P. Lee, K. C. Mills "The effect of Mould Flux Properties on Thermo-mechanical Behaviour during Billet Continuous Casting", *ISIJ International* Vol.47 2007 No1 pp. 95-104.
63. B. Zhao, B. G. Thomas S. P. Vanka, J. O' Malley "Transient Fluid Flow and Superheat Transport in Continuous Casting of Steel Slab", *Metallurgical and Materials Transactions B* Vol. 36B, Dec 2005-pp 801-823.
64. M. Alizadeh, A. Jahromi and O. Abouali, "A new Semi-analytical Model for Predictions of the strand Surface Temperature in Continuous Casting of Steel in Mold region", *ISIJ International*, Vol.48 (2008), No. 2, pp. 161-169.
65. Y. Meng and B. G. Thomas, "Heat Transfer and Solidification Model of Continuous Slab Casting: CON1D" *Metallurgical & Materials Transactions*, Vol. 34B, No. 5, Oct., 2003, pp. 685-705.
66. R. McDavid and B. G. Thomas, "Flow and Thermal Behavior of the Top Surface Flux Powder Layers in Continuous Casting Molds", *Metallurgical and Materials Transactions B*, Vol. 27B, No. 4 (August), 1996, pp. 672-685.
67. K. G. Rackers and B. G. Thomas, "Clogging in Continuous Casting Nozzles", 78th Steelmaking Conference Proceedings, April 2, 1995, Iron and Steel Society, Vol. 78, 1995, pp. 723-734.

68. B. G. Thomas, A. Denissov, H. Bai, "Behavior of Argon Bubbles during Continuous Casting of Steel", ISS 80<sup>th</sup> Steelmaking Conference, April 13-16,1997 pp.375-384.
69. B. G. Thomas, X. Huang, and R. C. Sussman, "Simulation of Argon Gas Flow Effects in a Continuous Slab Caster", Metallurgical Transactions B, Vol. 25B, No. 4, (August), 1994, pp. 527-547
70. M. B. Assar, P. H. Dauby and G. D. Lawson, "Opening the Black Box: PIV and MFC Measurements in a Continuous Caster Mold", Steelmaking Conference Proceedings, Vol. 83, ISS, Warrendale, PA, 2000, 397-411.
71. L. Zhang, S. Yang, X. Wang, K. Cai, J. Li, X. Wan and B.G Thomas, "Physical, Numerical and Industrial Investigation of Fluid Flow and Steel Cleanliness in the Continuous Casting Mold", Panzhihua SteelAISTech 2004, Nashville, TN, Sep.15-17, 2004, AIST, Warrendale, PA.
72. N. Kubo et al, "Two-phase Flow Numerical Simulation of Molten Steel and Argon Gas in a Continuous Casting Mold", *ISIJ International* Vol 42 (2002) No. 11, Page 1251-1258.
73. N. Kubo, T. Ishii, J. Kubota T. Ikagawa "Numerical Simulation of molten Steel Flow under a Magnetic Field with argon Gas Bubbling in a Continuous Casting Mold", *ISIJ International*, Vol. 44 (2004), No. 3,pp.556-564.
74. N. Kuno et al, "Molten Steel Flow Monitoring and Control by EMLS in a Continuous Casting Mold", The 5<sup>th</sup> International Symposium on Electromagnetic Processing of Materials, 2006, Japan, ISIJ.
75. D. Jiroveanu, P. Gardin and J-F Domgin, "Modelling and numerical simulation of 3D bubble flow by the Eulerian-Lagrangian approach", *Progress in Computational Fluid Dynamics*, Vol. 7, Nos. 2/3/4, Page 163–169.
76. Alexiadis, P. Gardin, J-F Domgin, "Probabilistic Approach for Break-up and Coalescence in bubbly flow and coupling with CFD codes" *Applied Mathematical modeling* 31 (2007) pp. 2051-2061.
77. Q. Yuan and B. G. Thomas, "Transport and Entrapment of Particles in Continuous Casting of Steel", TMS (The Mineral, Metals & and Materials Society),2006, Page1-8.
78. L. Zhang, J. Aoki and B. G. Thomas, "Inclusions Removal by Bubble Flotation in a Continuous Casting Mold", Metallurgical and Materials Transactions B Vol. 37B, June 2006 pp. 361-379.

79. B. G. Thomas and L. Zhang, “Mathematical Modeling of Fluid Flow In Continuous Casting”, *ISIJ International*, Vol 41 (2001), No 10 pp.1181-1193.
80. B. G. Thomas, “Application of Mathematical Models to the Continuous Slab Casting Mold”, *Iron and Steelmaker*, Vol. 16, No. 12 (December), 1989 pp.53-66.
81. K. A. Pericleous, K. S. Chan, M. Cross, “Free Surface Flow and Heat Transfer in Cavities: The SEA Algorithm”, *Advances in Computational Mathematics* Volume 6, Number 1 / December, 1996.
82. G. A. Panaras, A. Theodorakos, G. Bergeles, “Numerical Investigation of the Free Surface in a Continuous Steel Casting Mold Model”, *Metallurgical and Materials Transactions B* Vol. 29B, Oct 1998 pp. 1117-1126.
83. N. Bessho, R. Yoda, H. Yamasaki, T. Fujii, T. Nozaki, S. Takatori “Numerical Analysis of Fluid Flow in Continuous Casting Mold By Bubbles Dispersion”, *ISIL International* Vol. 31 (1991), No 1, pp.40-45.
84. Theodorakakos and G. Bergeles, “Numerical Investigation of the Free Surface in a Continuous Steel Casting Mold Water Model”, *Metallurgical and Materials Transactions B*, 1998, vol. 29B, pp 1321-1327.
85. R. Miranda, M. A. Barron, J. Barreto, L. H. Gonzalez, ‘Experimental and Numerical of the Free Surface in a Water Model of a Slab Continuous Casting Mold’, *ISIL International*, Vol. 45 (2005), No. 11 pp.1626-1635.
86. Ramos-Banderas et al., “Dynamics of two-phase downwards flows in submerged entry nozzles and its influence on the two-phase flow in the mold”, *International Journal of Multiphase Flow* 31 (2005) pp.643–665.
87. F. M. Najjar, B. G. Thomas and D. Hershey, “Numerical Study of Steady Turbulent Flow through Bifurcated Nozzles in Continuous Casting”, *Metallurgical Transactions B* Vol. 26B, No. 4, 1995, pp. 749-765.
88. D. Hershey, B. G. Thomas and F. M. Najjar, “Turbulent Flow through Bifurcated Nozzles”, *International Journal for Numerical Methods in Fluids*, Vol. 17, No. 1, 1993, pp. 23-47.
89. B. Lebon MSc Thesis, “Heat transfer across the flux layer and the mould region of a continuous casting”, University of Greenwich, 2007.

90. G-G Lee, B. G. Thomas, S-H. Kim, H-J. Shin, S-K. Baek, C-H. Choi, D-S. Kim, S-J. Yu “Microstructure near corners of Continuous-cast steel slabs showing three-dimensional frozen meniscus and hooks”, 2006 *Acta Materialia* 55 pp.6705-6712.
91. C. Ojeda, B.G. Thomas, J. Barco and J. L. Arena, “Model of Thermal-Fluid Flow in the Meniscus Region During An Oscillation Cycle”, AISTech 2007, Steelmaking Conference Proc., (May 7-10, Indianapolis, IN), AIST, Warrendale, PA, Vol. 1, 2007.
92. C. Ojeda, B. G. Thomas, J. Barco and J. Luis Arena, “Mathematical Model of Thermal-Fluid Flow in the Meniscus Region During An Oscillation Cycle”. AISTech 2006 Proceedings Volume 1 p.1017-1028.
93. P. Ramirez-Lopes, Peter D. Lee and K. D. Mills, “Explicit Modelling Of Slag Infiltration and Shell Formation During Mould Oscillation in Continuous Casting”, *ISIJ International*, Vol. 50 (2010), No. 3, pp.425-434.
94. J. Sengupta , B.G. Thomas, H.J. Shin, and S.H. Kim, “Mechanism of Hook Formation in Ultra-low Carbon Steels based on Microscopy Analysis and Thermal-stress Modeling”, AISTech 2006 Steelmaking Conference Proc., Vol. 1, 2006, pp. 903-914.
95. B. Li, T. Okane and T. Umeda, “Modeling of Molten Metal flow in continuous casting Process Considering the effects of Argon Gas Injection and Static Magnetic-Field Application”, *Metallurgical and Materials Transactions B* Vol. 31b Dec 2000 pp. 1491-1503.
96. B.G. Thomas, “Modeling of Continuous Casting” , *Chapter 5 in Making, Shaping and Treating of Steel*, 11th Edition, Vol. 5, Casting Volume, A. Cramb, editor, AISE Steel Foundation, Pittsburgh, PA, 2003, pp. 5.1-5.24.
97. S. Massey, “*Mechanics of Fluids*”, ( 5<sup>th</sup> edition, Van Nostrand Reinhold UK, 1987).
98. Croft TN, “PhD Thesis”, University of Greenwich, 1997 .
99. K. A. Pericleous, G. J. Moran, S. M. Bounds, P. Chow, M. Cross, “Three-dimensional free surface modeling in an unstructured mesh environment for metal processing applications”, *Proc. CFD in Mineral & Metal Processing and Power Generation*, pp. 321-328. Publ. CSIRO Division of Minerals. Melbourne, Australia, July 1997.
100. R. Courant, K. Friedrichs and H. Lewy, “On the partial difference equations of mathematical physics” *IBM Journal*, March 1967, pp. 215-234, English translation of the 1928 German original.
101. Wang Hong, “Research PhD Thesis”, University of Greenwich 2009.

102. C. T. Crowe, M. P. Sharma and D. E. Stock, "The Particle-Source-In Cell (PSI-CELL) Model for Gas-Droplet Flows", ASME, Transactions, Series I - Journal of Fluids Engineering, 99 (1977), 325-332.
103. R. Clift, J. R. Grace and M.E. Weber, "Bubbles, Drops and Particles", Academic Press, 1978.
104. J. T. Kuo, G. B. Wallis "Flow of Bubbles through Nozzles Medium", *Int. J. Multiphase Flow* 14 (1988) 547-564.
105. G. B. Wallis "The Terminal Speed of Single Drops or Bubbles in an Infinite Medium", *Int. J. Multiphase Flow* 1 (1974) 491-511.
106. Data dynamic web address: <http://www.dantecdynamics.com/>
107. Y. Xie et al, "Mathematical Modelling of Mould Temperature field during Continuous Casting of Steel", *Journal of Material Processing Technology* (2008) pp. 49-55.
108. Professor Pericleous, "CFD Lecture".
109. B. Reitow and B. G. Thomas, "Using nailboard experiments to qualify surface velocity in continuous casting", AIST Techn. 2008 Steelmaking Proc.
110. B. Spalding, A Novel, "Finite Difference Formulation for Differential Expressions Involving both First and Second Derivatives", *International Journal for Numerical Methods in Engineering*, 4, 551-559 (1972).
111. R. Courant, E. Isaacson and M. Rees, "On the Solution of Nonlinear Hyperbolic Differential Equations by Finite Difference", *Communications in Pure and Applied Mathematics* 5, 243-255 (1952).
112. S. V. Patankar "Numerical Heat Transfer and Fluid Flow", McGraw-Hill, New York (1980).
113. H. K. Versteeg, W. Malalasekera, "An introduction to Computational Fluid Dynamics".
114. X. Miao et al "Numerical Simulation of Two-phase Flow in a Slab Mold by MUSIG Model", 6<sup>th</sup> International Conference on Electromagnetic Processing of Materials 2009.
115. Y. Kwon, J. Zhang and H-G Lee, "Water Model and CFD Studies of Bubble Dispersion and Inclusions Removal in Continuous Casting Mold of Steel", *ISIJ International*, Vol. 46 (2006)No. 2 pp.257-266.

116. H. Yu and M. Zhu, “Numerical Simulation of the Effects of Electromagnetic Brake and Argon Gas Injection on the Three-dimensional Multiphase Flow and Heat Transfer in Slab Continuous Casting Mold”, *ISIJ International*, Vol.48 (2008) No.5pp.584-591.
117. Djambazov G. (2007), MB3 Mesh Builder for PHYSICA, *The University of Greenwich*.  
<http://staffweb.cms.gre.ac.uk/~dg06/phy3g/guide/mb3.htm>.
118. N. Kasai and M. Iguchi, “Water-model Experiment on Melting Powder Trapping by Vortex in the Continuous Casting Mold”, *ISIJ International*, Vol. 47 (2007),No7, pp.982-987.
119. N. J. Lawson, M. R. Davidson, “Oscillatory Flow in a Physical Model of a Thin Slab Casting Mould With a Bifurcated Submerged Entry Nozzle” *Journal of Fluid Engineering* June 2002, Vol. 124, pp 535-543
120. Y. Jin Jeon et al, “Flow Oscillations and Meniscus Fluctuations in a Funnel-Type Water Mold Model”, *Metallurgical and Materials Transactions B* Vol. 41B, Feb. 2010 pp. 121-130.
121. S. P. Vanka and B. G. Thomas, “Study of Transient Flow Structures in the Continuous Casting of Steel”, *Proceedings of the 2001 NSF Design & Manufacturing Grantees Conference*, Tampa, Florida, Jan. 7-10 2001, NSF, Washington, D.C. 14p.
122. DADisp web address: <http://www.dadisp.com>
123. P. Gardin and J-F Domgin, “Mathematical Description of Flows in Continuous Casting”, *Machine of Steel TMS* 2006.
124. G. Thomas, Q. Yuan, S. Sivaramakrishnan, and S. P. Vanka, “Transient fluid flow in the continuous steel-slab casting mold”, *JOM-e*, (Journal of Metals electronic edition).
125. P. Ramirez-Lopez et al, “A Coupled Model to Simulate the Solidification Inside the Continuous Casting Slab Mould”, *Liquid Metal Processing and Casting Symposium* 2007, p. 133-138, 2007.
126. C.A. Santos, A. Garcia, C.R. Frickand and J. A. Spim (2003), “Evaluation of heat transfer coefficients along the secondary cooling zones in the continuous casting of steel billets”, *Inverse Problems in Science and Engineering*, Vol. 14, No. 6, September 2006, pp. 687-700.
127. L. Zhang, S. Yang, X. Wang, K. Cai, J. Li, X. Wan, and B.G. Thomas, “Investigation of Fluid Flow and Steel Cleanliness in the Continuous Casting Strand”, *Metallurgical and Materials Transactions B*, Vol. 38B, No. 1, Feb., 2007, pp. 63-83.

128. B.G.Thomas and X. Huang, “Effect of Argon Gas on Fluid Flow in a Continuous Slab Casting Mold”, 76th Steelmaking Conference, Dallas, TX, March 28-31, 1993, Iron and Steel Society, Warrendale, PA, Vol. 76, 1993, pp. 273-289.
129. P. E. Ramirez-Lopez, P. D. Lee, K. C. Mills and B. Santillana, “A New Approach for Modelling Slag Infiltration and Solidification in a Continuous Casting Mould”, *ISIJ International*, Vol. 50 (2010) No. 12 pp.1797-1804.
130. B.G. Thomas, G. Li, A. Moitra and D. Habing, “Analysis of Thermal and Mechanical Behavior of Copper Molds during Continuous Casting of Steel Slabs”, Iron and Steelmaker (ISS Transactions), Iron and Steel Society, Warrendale, PA, Vol. 25, No. 10, 1998, pp. 125-143.
131. H. Yu and M. Zhu, “Numerical Simulation of the Effects of Electromagnetic Brake and Argon Gas Injection on the Three-dimensional Multiphase Flow and Heat Transfer in Slab Continuous Casting Mold”, *ISIJ International*, Vol. 48 (2008) No. 5 pp.584-591.
132. Z. Lei, Z. Ren, K. Deng, W. Li and Y. Zhong, “Amplitude-modulated Magnetic Field Coupled with Mold Oscillation in Electromagnetic Continuous Casting”, *ISIJ International*, Vol. 46 (2006) No. 5 pp.680-686
133. H-J Shin, S. H. Kim, B. G. Thomas, G. G. Lee, J. M. Park, and J. Sengupta, “Measurement and Prediction of Lubrication, Powder Consumption, and Oscillation Mark Profiles in Ultra-low Carbon Steel Slabs”, *ISIJ International*, Vol. 46, No. 11, 2006, pp. 1635-1644.
134. T. Araki and M. Ikeda, “Optimization of Mold Oscillation For High Speed-New Criteria For Mold Oscillation”, *Canadian Metallurgical Quarterly*, Vol. 38, No.5,pp. 295-300,1999.
135. K.C. Mills and A.B. Fox, “The role of Mould Fluxes in Continuous Casting-So Simple Yet So Complex”, *ISIJ International* 2003, 43(10)pp1479-1486.
136. B. E. Launder and D. B. Spalding, “The Numerical Computation of Turbulent Flows”, *Computer Methods in Applied Mechanics and Engineering*, **3**, 1974, pp. 269-289.
137. S. Mazumdar and S. K. Ray, “Solidification control in continuous casting of steel”, *Sadhana* Volume 26, Numbers 1-2, 179-198, DOI: 10.1007/BF02728485’
138. B. G. Thomas, “Recent Advances in Computational Modeling of Continuous Casting of Steel”, Scanmet II Conference, (Luleå, Sweden, June 6-9, 2004), MEFOS, Vol. 1, pp. 243-252.

139. Z. Xinyang, W. Xudong, M. Yong, Y. Man, Z. Li and Y. Shihong, "The Shell Surface Force Caused by Mould Friction during Slab Continuous Casting", *ISIJ International*, Vol. 48 (2008) No. 2 pp.170-174.
140. S. Koric et. al., "Explicit Coupled Thermo-Mechanical Finite Element Model of Steel Solidification" *Int. J. Num. Meths. Engineering*, 2009, Vol. 78, pp. 1-31.
141. Y. Meng and B.G. Thomas, "Interfacial Friction-Related Phenomena in Continuous Casting with Mold Slags, ISSTech 2003 Steelmaking Conference Proceedings, (Indianapolis, IN, Apr. 27-30, 2003), ISS-AIME, Warrendale, PA, 2003, pp. 589-606.
142. M. Bellet and B.G. Thomas, "Chapter 27, SOLIDIFICATION MACROPROCESSES (Thermal-mechanical Modeling of Stress, Distortion and Hot Tearing)," in *Materials Processing Handbook- Cat # 3216*, Joanna R. Groza; James F. Shackelford; Enrique J. Lavernia; Michael T. Powers, eds. CRC Press, 2007.
143. Rhino software Web address: URL: <http://www.rhino3d.com/>
144. A.D. Gosman and E. Ioannides, "Aspects of computer-simulation of liquid-fuelled combustors", *Journal of Energy*, 7 (6) (1983), 482-490.

## Appendices

### Appendix A. INFORM file for water model configuration

```
#####
#   INFORM file using Transient run, particle tracking, standard k-e model, SMART scheme,
#   CDM method - 2cm Oil with surface tension – Gas 2NL/min
#   Restart Case of 200s END TIME=400s TIME STEP=0.01
#   18-SEP-2008
#####
GEOMETRY_MODULE
  GRAVITY_Z -9.81
  FILENAME out
END

DATABASE_MODULE
  INPUT_DATABASE outza2
  OUTPUT_DATABASE outza3
END

GENERIC_MODULE
  TRANSIENT_RUN
  DELTA_T
  FOR_ALL_TIME_STEPS 0.01
  END
  END_TIME 400
  END
  MAX_SWEEPS 40
  USER_INTERVAL_SAVE OFF
END
# convert NL/min to kg/s
REAL mdotin

# Enter gas flow rate in NL / min
mdotin = 2
# Convert to Nm^3/s
mdotin = mdotin * 1.0E-3 / 60
# Convert to kg/s (Standard Pressure * Molecular weight of Argon)
#   -----
#   (Gas Constant * Standard Temperature)
mdotin = mdotin * 101325 * 0.040 / 8.3147 / 273

USER_MODULE
  OUTPUT_INITIAL ON
  OUTPUT_FREQUENCY 1.0

PARTICLE_TRACKING
  MASS_FLOW_RATE      mdotin
  CRITICAL_TIME       10.
  MAXIMUM_TIME_STEP   0.1
```

```

MINIMUM_TIME_STEP      0.001
NUMBER_OF_PARTICLES    1000
TURBULENCE_MODEL       ON
U_SOLVER               ON
V_SOLVER               ON
W_SOLVER               ON
PARTICLE_DIAMETER      0.001
PARTICLE_DENSITY       1.2
PRINT_PATH             ON
RESTITUTION_COEFFICIENT 0.5
SAVE_DIAMETERS         TRANSIENT
SAVE_VOLUME_FRACTIONS  TRANSIENT
STAGNATION_VELOCITY    1.e-5
TIME_STEPS_PER_ELEMENT 10
TRACK_WITHIN_ITERATION_LOOP OFF
TRACKING_FREQUENCY     25
END
END

MATERIAL_PROPERTY_MODULE
DENSITY
  MATERIAL 1 USER_ROUTINE mix3 3 1000 860. 1.2
END
# kin_wat = dyn_vis/density = 0.001/1000 = 1.0E-6
#kin_oil = dyn_vis/density = 0.0194/850 = 2.255E-5
  kin_water = 1.0E-6
  kin_oil = 2.255E-5
VISCOSITY
  MATERIAL 1 USER_ROUTINE FS_PROP 2 kin_water kin_oil
END
SURFACE_TENSION
  MATERIAL 1 CONSTANT 0.035
END
END

FREE_SURFACE_MODULE
GALA ON
STORE_FREESURF
  INITIAL_VALUES USER_ROUTINE perpatch 3 0. 1. 0.
END
END

SCALAR_MODULE
SOLVE_CDM_PHI
DIFFUSION_TERM OFF
TRANSIENT_COEFFICIENT
  ALL CONSTANT 1.
END
CONVECTION_COEFFICIENT
  ALL CONSTANT 1.
END
INITIAL_VALUES USER_ROUTINE perpatch 3 0. 1. 0.
BOUNDARY_CONDITIONS
  PATCH 1 FIXED_VALUE VALUE 1.
  PATCH 11 IN_OUT VALUE 1.

```

```

    PATCH 6 IN_OUT VALUE 0.
END
USER_SOURCE_TERMS
    CDM 2 1.5 0.05
END
END
END

REAL watrate ,Vel, area_in
# water flow rate 3.1m^3/h
# Enter water flow rate m^3/h
# wrate = 3.1
# Convert to m^3/s
#wrate = wrate / 3600
#MASS FLOW RATE = density * velocity * arrea
# The following value is the actual area of the inlet.
# It should probably be equal to PI*(18mm)^2 = 0.00102m
area_in = 0.00102
# Co= area_in* wrate
#Co = area_in*wrate
#Enter the Inlet velocity- Val = Inlet Velocity

#watrate = 1000 * Vel * area_in
# watrate = 0.816
#Co mass flow rate per unit area  watrate = 0.816/area_in = 0.00102
#11.1.3.2 ONLY_MASS
#In the only mass boundary condition the mass flow rate into
#the domain per unit area and the value of the solved variable
#at the boundary are set. The boundary condition ignores the
#contribution from the diffusion term and uses the set mass
#flow rate, dm/dt to convect the set value, v, into the domain.
#The source for this boundary type is equal
#Co = A*dm/dt
#Val = u

FLUID_FLOW_MODULE
    BUOYANCY
    BOUSSINESQ_APPROXIMATION OFF
    REFERENCE_DENSITY 860
END

SOLVE_U-MOMENTUM
    DIFFERENCE_SCHEME SMART
    FALSE_TIMESTEP 0.01
    INITIAL_VALUES ALL 0.0
BOUNDARY_CONDITIONS
    PATCH 1 ONLY_MASS FLOWRATE 1018 VALUE 0.
    PATCH 2 WALL COEFF 1. VALUE 0.0
    PATCH 3 WALL COEFF 1. VALUE 0.0
    PATCH 7 WALL COEFF 1. VALUE 0.0
    PATCH 8 WALL COEFF 1. VALUE 0.0
    PATCH 9 WALL COEFF 1. VALUE 0.0
    PATCH 10 WALL COEFF 1. VALUE 0.0
END
USER_SOURCE_TERMS
    surfTens 0

```

```

END
END

SOLVE_V-MOMENTUM
  INITIAL_VALUES ALL 0.0
  BOUNDARY_CONDITIONS
    PATCH 1 ONLY_MASS FLOWRATE 1018 VALUE 0.
    PATCH 2 WALL COEFF 1. VALUE 0.0
    PATCH 3 WALL COEFF 1. VALUE 0.0
    PATCH 7 WALL COEFF 1. VALUE 0.0
    PATCH 8 WALL COEFF 1. VALUE 0.0
    PATCH 9 WALL COEFF 1. VALUE 0.0
    PATCH 10 WALL COEFF 1. VALUE 0.0
  END
  USER_SOURCE_TERMS
    surfTens 0
  END
END

SOLVE_W-MOMENTUM
  DIFFERENCE_SCHEME SMART
  FALSE_TIMESTEP 0.01
  INITIAL_VALUES ALL 0.0
  BOUNDARY_CONDITIONS
    PATCH 1 ONLY_MASS FLOWRATE 1018 VALUE -1.018
    PATCH 2 WALL COEFF 1. VALUE 0.0
    PATCH 3 WALL COEFF 1. VALUE 0.0
    PATCH 7 WALL COEFF 1. VALUE 0.0
    PATCH 8 WALL COEFF 1. VALUE 0.0
    PATCH 9 WALL COEFF 1. VALUE 0.0
    PATCH 10 WALL COEFF 1. VALUE 0.0
  END
  USER_SOURCE_TERMS
    surfTens 0
  END
END

SOLVE_PRESSURE
  INITIAL_VALUES ALL 0.0
  BOUNDARY_CONDITIONS
    PATCH 11 FIXED_VALUE VALUE 0.
  END
  RESIDUAL_REFERENCE 100.
  END
END

REAL kin, epin, f_dt
f_dt = -1
REAL enut, ke, ep
kin = (0.1^2)*(1.018)^2
epin = 0.09*ke^2/enut

TURBULENCE_MODULE

KE_MODEL
  SOLVE_KINETIC_ENERGY
  DIFFERENCE_SCHEME SMART

```

```
FALSE_TIMESTEP 0.01
INITIAL_VALUES ALL 0.001
SAVE_VARIABLE NEVER
BOUNDARY_CONDITIONS
  PATCH 1 FIXED_VALUE VALUE kin
  PATCH 2 WALL COEFF 1. VALUE 0.0
  PATCH 3 WALL COEFF 1. VALUE 0.0
  PATCH 7 WALL COEFF 1. VALUE 0.0
  PATCH 8 WALL COEFF 1. VALUE 0.0
  PATCH 9 WALL COEFF 1. VALUE 0.0
  PATCH 10 WALL COEFF 1. VALUE 0.0
  PATCH 11 IN_OUT VALUE kin
END
END

SOLVE DISSIPATION_RATE
DIFFERENCE_SCHEME SMART
FALSE_TIMESTEP 0.01
INITIAL_VALUES ALL epin
BOUNDARY_CONDITIONS
  PATCH 1 FIXED_VALUE VALUE epin
  PATCH 2 WALL COEFF 1. VALUE 0.0
  PATCH 3 WALL COEFF 1. VALUE 0.0
  PATCH 7 WALL COEFF 1. VALUE 0.0
  PATCH 8 WALL COEFF 1. VALUE 0.0
  PATCH 9 WALL COEFF 1. VALUE 0.0
  PATCH 10 WALL COEFF 1. VALUE 0.00
  PATCH 11 IN_OUT VALUE epin
END
END
SAVE_GENERATION_RATE NEVER
END
END

MONITOR_MODULE
OUTPUT_INTERVAL 5
MONITOR_LOCATION 0.11 0.0 -0.116
WRITE_TO_FILE zk.txt
END

POST-PROCESSING_MODULE
FEMGV_FORMAT
END
TECPLOT_FORMAT
TIME_STEP_FREQUENCY 50
END
END

STOP
```

**Appendix B. INFORM file for industrial model configuration**

```
#####
# INFORM file for the steady-run using turbulence, Heat transfer and Solidification #
# Particle Tracking, Fixed Surface #
# 7cm of Flux, Immersion depth: 160mm, Casting Speed 0.8m/min #
# 18-May-2010 #
#####

# Constants to be used in the inform
REAL TempIn, TAmp, SolidTemp, LiquidTemp
LiquidTemp = 1529
SolidTemp = 1495.1
TempIn = 1600
TAmp = 22
Kpwsld = 0.23

REAL gasMas, gasDen, gasVol, totVol
gasMas =10.4e-5
gasDen = 0.28
gasVol = gasMas/gasDen

REAL CASTVEL , Abot, Ainlet, metVol,wIn
Abot= 1.9 * 0.229 /2
Ainlet = 0.194 * 0.067/2
CASTVEL = 0.8/60
metVol = CASTVEL * Abot
wIn = metVol / Ainlet

GEOMETRY_MODULE
GRAVITY_Z -9.81
FILENAME GHalfrect160
END

DATABASE_MODULE
INPUT_DATABASE stead
OUTPUT_DATABASE stead
END

GENERIC_MODULE
STEADY_STATE_RUN
MAX_SWEEPS 50000
USER_INTERVAL_SAVE ON
END

MATERIAL_PROPERTY_MODULE
DENSITY
MATERIAL 1 PARTS 2
PART 1 CELL_T_DEPENDENT 10 -1E+9 7605
                                0 7605
                                500 7442.9
                                900 7370
                                1000 7320
                                1100 7266
                                1300 7168
```

```

1500 7067
1600 7016.4
1.0E+9 7290
PART 2 CONSTANT 0.28
PROPERTY USER_ROUTINE bubble 0
END
MATERIAL 2 CONSTANT 2500
END
DYNAMIC_VISCOSITY ON
VISCOSITY
MATERIAL 1 CONSTANT 5.4E-3
MATERIAL 2 CELL_T_DEPENDENT 7 -1000000 5
770 1.7
1000 1.3
1100 0.11
1300 0.09
1500 0.07
1.0E+9 0.065
END
THERMAL_CONDUCTIVITY
MATERIAL 1 CELL_T_DEPENDENT 4 -1000000 32
SolidTemp 32
LiquidTemp 40.3
1.0E+9 40.3
MATERIAL 2 CELL_T_DEPENDENT 9 -100000 0.23
20 Kpwsld
400 0.4
600 0.55
800 0.7
900 0.85
1100 1.5
1700 3.0
1.0E+9 3.0
END
SPECIFIC_HEAT
MATERIAL 1 CELL_T_DEPENDENT 11 -1000000 428
477 550
602 750
802 950
902 653
1210 653
1330 672
1509 700
1529 800
1600 822
1.0E+9 822
MATERIAL 2 CONSTANT 2040.
END
LATENT_HEAT
MATERIAL 1 CONSTANT 263250.
MATERIAL 2 CONSTANT 500000
LINEAR_RELAXATION 0.8
END
LIQUIDUS_TEMPERATURE
MATERIAL 1 CONSTANT 1527.7
MATERIAL 2 CONSTANT 1100

```

```

    LINEAR_RELAXATION 0.8
  END
  SOLIDUS_TEMPERATURE
    MATERIAL 1 CONSTANT 1495.1
    MATERIAL 2 CONSTANT 1000
    LINEAR_RELAXATION 0.8
  END
  SURFACE_TENSION
    MATERIAL 1 CONSTANT 1.4
  END
END

# Enter gas flow rate in NL / min
REAL mdotin ,
mdotin = 7/2
# Convert to Nm^3/s
mdotin = mdotin * 1.0E-3 / 60
# Convert to kg/s (Standard Pressure * Molecular weight of Argon)
# -----
# (Gas Constant * Standard Temperature)
mdotin = mdotin * 101325 * 0.040 / 8.3147 / 273
# MDOTIN = 1.48794E-4

```

```

USER_MODULE
  OUTPUT_INITIAL ON
  OUTPUT_FREQUENCY 0.5
  PARTICLE_TRACKING
    MASS_FLOW_RATE      mdotin
    CRITICAL_TIME       10.
    MAXIMUM_TIME_STEP   0.1
    MINIMUM_TIME_STEP   0.001
    NUMBER_OF_PARTICLES 1000
    TURBULENCE_MODEL    ON
    U_SOLVER            ON
    V_SOLVER            ON
    W_SOLVER            ON
    PARTICLE_DIAMETER   0.001
    PARTICLE_DENSITY    0.28
    PRINT_PATH          OFF
    RESTITUTION_COEFFICIENT 0.5
    SAVE_DIAMETERS      TRANSIENT
    SAVE_VOLUME_FRACTIONS TRANSIENT
    STAGNATION_VELOCITY 1.e-5
    TIME_STEPS_PER_ELEMENT 10
    TRACK_WITHIN_ITERATION_LOOP ON
    TRACKING_FREQUENCY  500
  END
END

```

```

#####Heat and Solidification#####
SOLIDIFICATION_MODULE
  INITIAL_FRACTION_LIQUID PER_MATERIAL
    MATERIAL 1 1.
    MATERIAL 2 0.
  END

```

```

FRACTION_LIQUID_FUNCTION
  MATERIAL 1 LINEAR_FUNCTION
  MATERIAL 2 LINEAR_FUNCTION
END
  UPDATE_TEMP ON
  SOLID_VELOCITY 0 0 -CASTVEL
  PERMEABILITY_COEFFICIENT 1E-7
  DARCY_SOURCE_METHOD 3
  UNDER_RELAXATION_VALUE 0.8
END

HEAT_TRANSFER_MODULE
  SOLVE_TEMPERATURE
  FALSE_TIMESTEP 0.06
  INITIAL_VALUES PER_MATERIAL
    MATERIAL 1 1600
    MATERIAL 2 100
  END
  BOUNDARY_CONDITIONS
    PATCH 1 FIXED_VALUE VALUE TempIn
# !Top free boundary
    PATCH 6 COEFF_VALUE COEFF 100. VALUE Tmp
# Slag wall X-plane
    PATCH 13 COEFF_VALUE COEFF 100. VALUE Tmp
# Slag wall Y-plane
    PATCH 23 USER_ROUTINE walls_side 1 Tmp
#!Mould wall X-plane
    PATCH 14 USER_ROUTINE walls_side 1 Tmp
#!Mould wall y-plane
    PATCH 24 USER_ROUTINE walls_side 1 Tmp
#Tank wall X-plane
    PATCH 15 USER_ROUTINE walls_side 1 Tmp
#Tank wall Y-plane
    PATCH 25 USER_ROUTINE walls_side 1 Tmp
  END
  RESIDUAL_REFERENCE 1000.
END
END

#####Store Free Surface#####

FREE_SURFACE_MODULE
  GALA ON
  STORE_FREESURF
  INITIAL_VALUES USER_ROUTINE perpatch 6 0. 1. 0. 1. 0. 1.
  END
END

#####Momentum Equations#####

FLUID_FLOW_MODULE
  MOMENTUM_FALSE_TIMESTEP 0.6

  BUOYANCY
  BOUSSINESQ_APPROXIMATION OFF
  REFERENCE_DENSITY 7000.

```

```

END
SOLVE_U-MOMENTUM
  INITIAL_VALUES ALL 0.0
  BOUNDARY_CONDITIONS
    PATCH 1 FIXED_VALUE VALUE 0.
    PATCH 3 WALL COEFF 1. VALUE 0.0
    PATCH 4 WALL COEFF 1. VALUE 0.
    PATCH 5 WALL COEFF 1. VALUE 0.
    PATCH 9 WALL COEFF 1. VALUE 0.
    PATCH 13 WALL COEFF 1. VALUE 0.
    PATCH 23 WALL COEFF 1. VALUE 0.
    PATCH 14 WALL COEFF 1. VALUE 0.
    PATCH 24 WALL COEFF 1. VALUE 0.
    PATCH 15 WALL COEFF 1. VALUE 0.
    PATCH 25 WALL COEFF 1. VALUE 0.
  END
  USER_SOURCE_TERMS
    surfTens 0
  END
END

```

```

SOLVE_V-MOMENTUM
  INITIAL_VALUES ALL 0.0
  BOUNDARY_CONDITIONS
    PATCH 1 FIXED_VALUE VALUE 0.
    PATCH 3 WALL COEFF 1. VALUE 0.0
    PATCH 4 WALL COEFF 1. VALUE 0.
    PATCH 5 WALL COEFF 1. VALUE 0.
    PATCH 9 WALL COEFF 1. VALUE 0.
    PATCH 13 WALL COEFF 1. VALUE 0.
    PATCH 23 WALL COEFF 1. VALUE 0.
    PATCH 14 WALL COEFF 1. VALUE 0.
    PATCH 24 WALL COEFF 1. VALUE 0.
    PATCH 15 WALL COEFF 1. VALUE 0.
    PATCH 25 WALL COEFF 1. VALUE 0.
  END
  USER_SOURCE_TERMS
    surfTens 0
  END
END

```

```

SOLVE_W-MOMENTUM
  INITIAL_VALUES ALL 0.0
  BOUNDARY_CONDITIONS
    PATCH 1 FIXED_VALUE VALUE -wIn
    PATCH 3 WALL COEFF 1. VALUE 0.0
    PATCH 4 WALL COEFF 1. VALUE 0.
    PATCH 5 WALL COEFF 1. VALUE 0.
    PATCH 9 WALL COEFF 1. VALUE 0.
    PATCH 13 WALL COEFF 1. VALUE 0.
    PATCH 23 WALL COEFF 1. VALUE 0.
    PATCH 14 WALL COEFF 1. VALUE 0.
    PATCH 24 WALL COEFF 1. VALUE 0.
    PATCH 15 WALL COEFF 1. VALUE 0.
    PATCH 25 WALL COEFF 1. VALUE 0.
  END

```

```

USER_SOURCE_TERMS
  surfTens 0
END
END

SOLVE_PRESSURE
  INITIAL_VALUES ALL 0.0
  BOUNDARY_CONDITIONS
    PATCH 2 FIXED_VALUE VALUE 0.
  END
  RESIDUAL_REFERENCE 1000.
END
END

#####k-e turbulence model#####
REAL enut, ke, ep
  kin = (0.1^2)*(wIn)^2
  epin = 0.09*ke^2/0.097
TURBULENCE_MODULE
  KE_MODEL
  SOLVE_KINETIC_ENERGY
    FALSE_TIMESTEP 0.01
    INITIAL_VALUES ALL 0.01
    BOUNDARY_CONDITIONS
      PATCH 1 FIXED_VALUE VALUE kin
      PATCH 3 WALL COEFF 1. VALUE 0.
      PATCH 4 WALL COEFF 1. VALUE 0.
      PATCH 5 WALL COEFF 1. VALUE 0.
      PATCH 9 WALL COEFF 1. VALUE 0.
      PATCH 13 WALL COEFF 1. VALUE 0.
      PATCH 23 WALL COEFF 1. VALUE 0.
      PATCH 14 WALL COEFF 1. VALUE 0.
      PATCH 24 WALL COEFF 1. VALUE 0.
      PATCH 15 WALL COEFF 1. VALUE 0.
      PATCH 25 WALL COEFF 1. VALUE 0.
      PATCH 2 IN_OUT VALUE kin
    END
    SAVE_VARIABLE NEVER
  END
END

SOLVE DISSIPATION_RATE
  FALSE_TIMESTEP 0.01
  INITIAL_VALUES ALL epin
  BOUNDARY_CONDITIONS
    PATCH 1 FIXED_VALUE VALUE epin
    PATCH 3 WALL COEFF 1. VALUE 0.
    PATCH 4 WALL COEFF 1. VALUE 0.
    PATCH 5 WALL COEFF 1. VALUE 0.
    PATCH 9 WALL COEFF 1. VALUE 0.
    PATCH 13 WALL COEFF 1. VALUE 0.
    PATCH 23 WALL COEFF 1. VALUE 0.
    PATCH 14 WALL COEFF 1. VALUE 0.
    PATCH 24 WALL COEFF 1. VALUE 0.
    PATCH 15 WALL COEFF 1. VALUE 0.
    PATCH 25 WALL COEFF 1. VALUE 0.

```

```

    PATCH 2 IN_OUT VALUE epin
    END
    SAVE_VARIABLE NEVER
    END

    SAVE_GENERATION_RATE NEVER
    END
    END
    MONITOR_MODULE
    OUTPUT_INTERVAL 20
    MONITOR_LOCATION 0.07 0.0 0.17
    WRITE_TO_FILE SteadySim.txt
    END

    POST-PROCESSING_MODULE
    FEMGV_FORMAT
    END
    TECPLOT_FORMAT
    END
    END

    STOP

```

## Appendix C. PHYSICA User routine

### C. 1. Moving Solid

```

ELSEIF (Command (1: cmdlen) .EQ. 'SOLID_VELOCITY') THEN
    cfound = .TRUE.
    CALL count_arguments ( String(1:strlen), n_args )
    DO arg_no = 2, MIN(n_args, 4)
        CALL read_arg_as_real
    @   (String(1:strlen), arg_no, SOLID_VEL(arg_no-1))
    END DO
ELSE IF ( SRC_EQN_NAM(1:namsiz) .EQ. 'SOLIDF_FLOW' ) THEN
    Handld = .TRUE.
    IF ( DISCRETISE .EQ. DISC_FV_CC ) THEN
        IF (VAR_ID .EQ. UN_P) THEN
            j = 1
        ELSE IF (VAR_ID .EQ. VN_P) THEN
            j = 2
        ELSE
            j = 3
        END IF
    IF ( GROUP_ID .LE. 0 ) THEN
        DO iele = 0, TOTELE-1
            zpos = Ra(CENTRE_P+3*iele+2)
            IF ( zpos .LT. 0.0 ) THEN
                Ra(SPV_P+iele) = Ra(SPV_P+iele) - Ra(DARCY_P+iele)
                zpos = Ra(CENTRE_P+3*iele+2)
            IF (IA(ELEMAT_P+iele).EQ.1)
    @   Ra (SCV_P +iele) = Ra (SCV_P+iele) + Ra(DARCY_P + iele) *
    @   SOLID_VEL (j)

```

```

        END IF
    END DO
ELSE
    DO iele = 0, TOTELE-1
        zpos = Ra(CENTRE_P+3*iele+2)
        IF ( zpos .LT. 0.0 ) THEN
            IF( La(GROUP_ID+iele) )
@           Ra(SPV_P+iele) = Ra(SPV_P+iele) - Ra(DARCY_P+iele)
        END IF
    END DO
END IF

```

## C. 2. Heat Flux in the Mould

```

ELSE IF (SRC_EQN_NAM(1:10).EQ.'walls_side') THEN
    handld = .TRUE.
    fminus = SRC_FACE_ID - 1
    eminus = SRC_ELE_ID - 1
    tamb = 30.0
    IF (SRC_NUM_VAL.GT.0 ) tamb = Ra (SRC_VALPTR)
        z= 0.0
        DO i = 0 , Ia(NOPINF_P + fminus) - 1
            pt = Ia( FACPTS_P + TOTPIF * fminus+i)-1
            z = z +Ra (XYZCRD_P+3*pt+2)
        END DO
        z = -z/REAL(Ia(NOPINF_P+fminus))
    IF (z.LT.0) THEN
        SRC_COEFF = 0.0
        SRC_VALUE = 0.0
    ELSE IF (z. LT. 0.9)THEN
        SRC_COEFF = 1.0E-10
        SRC_VALUE = -175.0-z*(90.0-175.0)/0.9
        SRC_VALUE = SRC_VALUE * 1.0E-2*1E+6/SRC_COEFF
    ELSE IF (z.LT.1.16) THEN
        SRC_VALUE = tamb
        SRC_COEFF = 0.098E-2*1.0E+06
    ELSE IF (z.LT.1.6)THEN
        SRC_VALUE = tamb
        SRC_COEFF = 0.0841E-2*1.0E+06
    ELSE
        SRC_COEFF = 0.0
        SRC_VALUE = 0.0
    END IF
END IF

```

## **Appendix D CD containing Thesis .pdf file and CC animations**

D1.1 CFD-SMART 0.5m\_s Oil 2cm Gas 0.**avi**

D1.2 LDA 0.5m\_s Oil 2cm Gas 0.**wmv**

D2.1 CFD-SMART 0.8m\_s Oil 2cm Gas 0.**avi**

D2.2 LDA 0.8m\_s Oil 2cm Gas 0.**wmv**

D2.3 CFD-SMART 0.8m\_s Oil 2cm Gas 2.**avi**

D2.4 LDA 0.8m\_s Oil 2cm Gas 2.**wmv**

D3.1 CFD-SMART 1.018m\_s Oil 0cm Gas 0.**avi**

D3.2 LDA 1.018m\_s Oil 0cm Gas 0.**wmv**

D3.3 CFD-SMART 1.018m\_s Oil 2cm Gas 0.**avi**

D3.4 LDA 1.018m\_s Oil 2cm Gas 0.**wmv**

D3.5 CFD-Hybrid 1.018m\_s Oil 2cm Gas 0.**avi** (turbulence model eliminated in the oil layer)

D3.6 CFD-SMART 1.018m\_s Oil 2cm Gas 2.**avi**

D3.7 LDA 1.018m\_s Oil 2cm Gas 2.**wmv**